# Quantum oscillations and charge-neutral fermions in Kondo insulator $YbB_{12}$

Ph. D. Thesis

Department of Physics, Kyoto University, Japan

January, 2021

Yuki Sato

# Abstract

Strong electronic correlation in many-body systems often results in a wide variety of ground states, leading to phenomena such as heavy Fermi liquids, unconventional superconductivity, and strongly correlated insulators. Understanding those exotic electronic phases and excitations (i.e., emergent quasiparticles) from these ground states is the most fundamental and important research problem in condensed matter physics. A Kondo insulator (KI) is a typical example of such strongly correlated insulators, where hybridization between conduction $c$-electrons and localized $f$-electrons opens up a charge gap across the Fermi level. KIs have recently attracted much interest because of the following important theoretical predictions and experimental findings:

(a) Strong electronic correlation can drive certain KIs into topological insulators.

(b) The KIs exhibit quantum oscillations in high magnetic fields.

(c) The KIs show gapless fermionic excitations.

In this thesis, we study exotic electronic properties found in $YbB_{12}$, which is a topological Kondo insulator candidate. In correspondence with the aforementioned findings, our results reveal that $YbB_{12}$ shows (b) quantum oscillations and (c) gapless fermionic excitations. We stress that the observations of both (b) and (c), in general, indicate the presence of a Fermi surface, which has been considered a defining characteristic of metals. Our findings, therefore, demonstrate novel electronic properties in $YbB_{12}$: it exhibits "metallic" behavior, although it is electrically insulating.

This thesis is structured as follows. In chapter 1, we introduce the physics of KIs. Subsequently, we review the electronic properties of the candidate materials $SmB_6$ and $YbB_{12}$, including recent progress in the search for topological surface states. In chapter 2, we examine previous reports and theoretical proposals on the observations of quantum oscillations in $SmB_6$. We discuss the observation of quantum oscillations in $YbB_{12}$

in chapter 3. After briefly introducing the purpose of this study in chapter 4, we present the results of thermal transport measurements in $YbB_{12}$, which is the main finding of this thesis, in chapter 5. The abstract of chapter 5 is as follows.

- **Charge-neutral fermions in $YbB_{12}$ (Chapter 5)**

The presence of a Fermi surface is manifested in the linear temperature ($T$)-dependent terms in specific heat and thermal conductivity. We present low-temperature heat-transport measurements to discuss low-energy excitations in the ground state of $YbB_{12}$. At zero field, sizable linear $T$-dependent terms are clearly observed in the specific heat and thermal conductivity, indicating the presence of gapless fermionic excitations with an itinerant character. Remarkably, the observed linear $T$-dependent thermal conductivity leads to a spectacular violation of the Wiedemann–Franz law: the Lorenz ratio is $10^4$–$10^5$ times larger than that expected in conventional metals, indicating that $YbB_{12}$ is electrically insulating but thermally metallic. Interestingly, the neutral fermions become more mobile when the sample becomes more insulating, ruling out the possibility that minor metallic impurities contribute to the heat transport. Moreover, these fermions couple to magnetic fields, despite their charge neutrality. Our findings expose novel quasiparticles in this unconventional quantum state, which are potentially identical to what contributes to the quantum oscillations in the insulating phase.

Finally, we summarize and conclude the thesis in chapter 6.

# Contents

# 1 Introduction

Contrary to free electron gases, strong electronic correlation in many-body systems often results in a wide variety of electronic ground states, leading to phenomena such as heavy Fermi liquids, unconventional superconductivity, magnetism, hidden order, strongly correlated insulators. Understanding those exotic electronic phases and excitations (i.e., emergent quasiparticles) from those ground states is the most fundamental and important research problem in condensed matter physics. Among those strongly correlated electronic systems, the physical properties of rare-earth compounds have been intensively studied. The key ingredient is the inner $4f$ electrons of rare-earth elements; these electrons are mostly localized in their atomic environment, and their moments play a role in magnetism. However, once the localized moments are immersed in a sea of mobile conduction electrons, they interact strongly on decreasing the temperature. Consequently, the localized moments can occasionally become itinerant through the interaction with the conduction electrons. In this chapter, we introduce the physics of these rare-earth compounds, including the Kondo effect, and examine how these many-body systems can be modeled and can produce a rich variety of electronic properties. A Kondo insulator (KI), which is the main focus of this thesis, can also be introduced within this framework. We also introduce the topological nature of KIs, which is a new perspective that emerged with recent progress in the field of condensed matter physics. Finally, we examine the electronic structure of prototypical candidates of KIs, $SmB_6$ and $YbB_{12}$.

## 1.1 Kondo effect

The problem of the interaction between localized moments and conduction electrons can be traced to the well-known Kondo problem, which concerns the resistivity minimum found in metals with dilute magnetic impurities. Hereafter, we refer to the problem as the dilute Kondo effect to distinguish it from the problem in a lattice system, which will be introduced in the next subsection 1.2. The theoretical explanation for this phenomenon was first reported by Kondo in 1964 [1]. Kondo showed that the coupling $J$ between conduction electrons and a magnetic moment yields singularity in the second perturbation scattering term, leading to a logarithmic increase in the resistivity through the factor -$\log T$ with decreasing temperature $T$. Corresponding to this singularity, the Kondo interaction involves the logarithmic growth of the effective interaction $J$:

$$J \to J(T) = J + 2J^2 N(0) \left( \ln \frac{D}{T} \right), \tag{1.1}$$

where $N(0)$ is the density of states (DOS) at the Fermi level and $D$ is the width of the conduction band. It is worth noting that this term originates from both the noncommutative relation of the local moment spin operators, $[S_+, S_-] \neq 0$, and the Fermi-Dirac distribution function; therefore, it has roots in the quantum many-body effect. This formulation is quite novel in that the interaction becomes larger as the energy scale becomes smaller. The logic later sparked a novel concept called asymptotic freedom in particle physics. The logarithmic growth, however, implies that some physical properties cannot avoid divergence as $T \to 0$. This failure of the theory at low temperature is clear because the correction term becomes comparable to the non-perturbation term below the characteristic Kondo temperature $T_{\mathrm{K}}$ defined by

$$T_{\mathrm{K}} \sim D \exp\left[ -\frac{1}{2JN(0)} \right]. \tag{1.2}$$

Therefore, the low-temperature physics below $T_{\mathrm{K}}$ remained a puzzle until the 1970s, stimulating further theoretical investigations. Wilson later developed the renormalization group theory and solved this problem [2]. Now, the Kondo physics is strictly solved throughout the temperature range [3]. The same expression of $T_{\mathrm{K}}$ can be also obtained from the scaling theory developed by Anderson [4]. In the strong coupling regime at low temperature, the spin of localized moments and the sea of conduction electrons form a Kondo singlet, where the moment is screened by the sea of conduction electrons, and the magnetic degree of freedom of the moment disappears.

## 1.2 Kondo lattice

As rare-earth compounds contain the "magnetic impurity" of $4f$ electrons at each lattice site, one can expand the above dilute Kondo problem by including lattice periodicity in the moments. The underlying physics of the system can be described by the Kondo lattice Hamiltonian:

$$H = -t \sum_{(i,j)\sigma} (c^{\dagger}_{i\sigma} c_{j\sigma} + \text{h.c.}) + J \sum_{j,\alpha\beta} \vec{S_j} \cdot c^{\dagger}_{j\alpha} \vec{\sigma_{\alpha\beta}} c_{j\beta}, \tag{1.3}$$

where $t$ is a hopping integral, $c^{\dagger}_{i\sigma}$ is an electron creation operator at site $i$ with spin $\sigma$, and $\vec{S_j}$ is a spin operator of localized moments at site $j$. In the lattice system, the Kondo effect coherently occurs over the whole lattice, leading to the ground state of the non-magnetic Kondo singlet. This is because elastic scatterings at the local moment conserves momentum owing to translational symmetry [5]. Consequently, the system develops Fermi liquid (FL) behavior with the renormalized effective mass $m^*$, reflecting the strong electronic correlation. In Kondo lattice systems, $m^*$ typically becomes 100-1000 times larger than that of a bare electron; hence, the quasiparticle is called a heavy fermion. Although all the physical properties show universal behavior with respect to $T/T_{\mathrm{K}}$ in the dilute Kondo system, this is not the case for a lattice system, which has another energy scale related to the Kondo coherence: $k_{\mathrm{B}}T^*$. Here, $T^*$ is called the coherent temperature below which the sea of conduction electrons requires coherence, leading to the formation of FL. $T^*$ is always lower than $T_{\mathrm{K}}$, below which the Kondo singlet locally begins to occur. The relation between $T^*$ and $T_{\mathrm{K}}$ is a subtle problem, and it has been pointed out that $T^*$ strongly depends on the density of conduction electrons [6].

There also exists another type of interaction between conduction and local electrons, known as the Rudermann Kittel Kasuya Yoshida (RKKY) interaction. Immediately after a conduction electron interacts with a local moment, the spin of the conduction electron has polarization for a moment. As other local moments can experience this polarization through the conduction electron, one can regard this effect as an effective exchange interaction between two local moments. The RKKY interaction is given by

$$H_{\mathrm{RKKY}} = -9\pi \frac{J^2}{\epsilon_{\mathrm{F}}} \left( \frac{N_e}{N} \right)^2 f(2k_{\mathrm{F}}R)\boldsymbol{S_1} \cdot \boldsymbol{S_2}, \tag{1.4}$$

where $R$ is the distance between given two local moments and $f(x) = (-x\cos x + \sin x)/x^4$ is the function that describes the spatial modulation of the interaction. Because $f(x)$ oscillates by changing its sign as a function of $R$, the effective interaction becomes either ferromagnetic or antiferromagnetic. Now, the RKKY interaction is established as a major mechanism causing the emergence of magnetism in heavy fermion systems.

The competition between the Kondo effect and RKKY interaction was pointed out by Doniach [7]. In the Doniach phase diagram shown in Fig. 1.1, the Kondo temperature $T_{\mathrm{K}}$ (the red curve) and Néel temperature $T_{\mathrm{N}}$ (the blue curve), which corresponds to the strength of the RKKY interaction, are plotted as a function of the coupling constant $J$. In the weak coupling regime of $T_{\mathrm{N}} > T_{\mathrm{K}}$, the ground state with magnetism becomes stable. In the strong coupling regime of $T_{\mathrm{K}} > T_{\mathrm{N}}$, on the other hand, the Kondo interaction overcomes the RKKY interaction, and Kondo screening leads to the coherent heavy fermion quasiparticles below $T^*$. In other words, the coupling strength $J$ determines whether the $f$-electrons become localized or itinerant.

Around the point where $T_{\mathrm{N}} \sim T_{\mathrm{K}}$, the system undergoes a phase transition between these states; remarkably, the phase transition can occur even at $T = 0$. Most of the phase transitions occurring at finite temperature are driven by thermal fluctuation. On the other hand, the phase transition at absolute zero temperature is called a quantum phase transition, which is driven by the uncertainty principle of quantum mechanics. In the vicinity of the critical constant $J_c$, which is called the quantum critical point (QCP), novel quantum phenomena, such as unconventional superconductivity and non-FL behavior are occasionally realized. Several types of QCPs including heavy fermion systems have been reported thus far, and they have provided interesting platforms to study a series of exotic electronic states in strongly correlated systems [8].

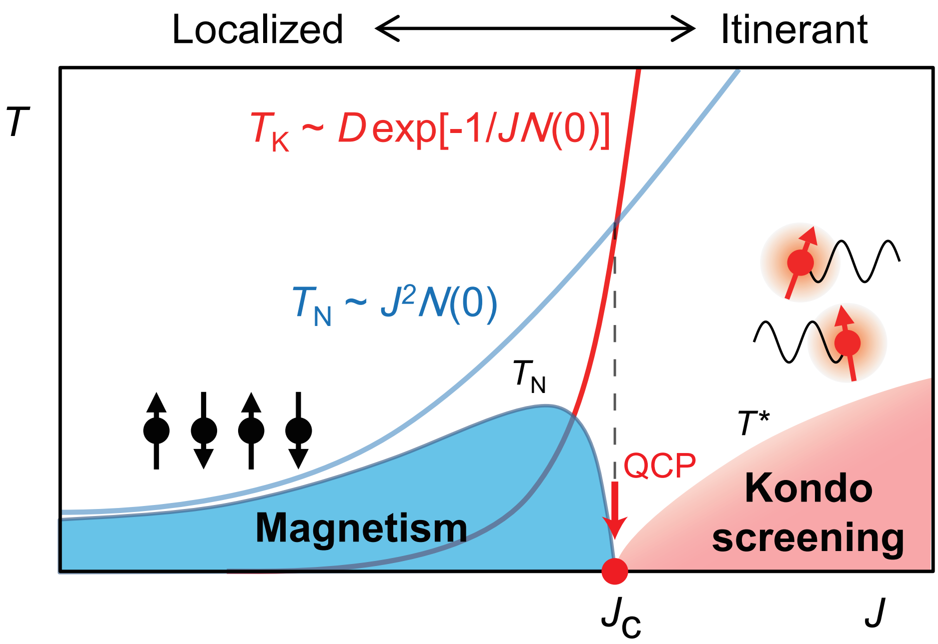


Figure 1.1: Schematic of the Doniach phase diagram. Magnetic order and a Kondo screened state are realized according to the coupling strength $J$. $f$-electrons become itinerant on approaching the right side of the graph.

## 1.3 Kondo insulator

In the Kondo screening regime with a high coupling strength $J$, the renormalized coherent band dispersion of a heavy FL is well defined. However, the question of whether the system becomes metallic or insulating below the coherent temperature $T \ll T^*$ is not trivial. Several types of models have been proposed to study Kondo physics. To examine the insulating ground state, let us first express Eq. 1.3 in the limit of $t/J \to 0$ as

$$H = J \sum_{j,\alpha\beta} \vec{S}_j \cdot \vec{\sigma_j} + O(t), \tag{1.5}$$

where $\vec{\sigma_j} \equiv c^{\dagger}_{j\alpha} \vec{\sigma_{\alpha\beta}} c_{j\beta}$. The Hamiltonian simply describes the onsite antiferromagnetic ($J > 0$) interaction, leading to a non-magnetic ground state, where the Kondo singlet is formed at each site as

$$|\mathrm{KI}\rangle = \prod_j \frac{1}{\sqrt{2}} \left( \Uparrow_j \downarrow_j - \Downarrow_j \uparrow_j \right). \tag{1.6}$$

Here, the double and single arrows denote the spin of local and conduction electrons, respectively. It is apparent that this ground state has a spin gap of $2J$ as a triplet excitation and a charge gap of $3J$, which separates the hole and electron quasiparticle dispersion bands [5]. Therefore, the Kondo singlet state in the limit of $t/J \to 0$ is insulating. The Kondo screened system, in which the Fermi energy lies in the charge gap, is called a Kondo insulator (KI). In addition to Mott insulators, KIs are known to be a typical example of correlated insulators, which acquire the insulating ground state owing to strong electron correlation.

To examine how the Kondo lattice becomes either a KI or a heavy FL, it is instructive to introduce the band structure of the system. The nature of the insulating ground state can be understood by introducing the band hybridization, and this view is preferable especially when we discuss the topological order of a certain insulator in subsection 1.5. The model we employ here is the periodic Anderson model:

$$H = \sum_{\boldsymbol{k}\alpha} \epsilon^c_{\boldsymbol{k}\alpha} n^c_{\boldsymbol{k}\alpha} + \epsilon^f \sum_{i\alpha} n^f_{i\alpha} + \sum_{\boldsymbol{k}\alpha} \left( V_{\boldsymbol{k}} f^\dagger_\alpha c_{\boldsymbol{k}\alpha} + \text{h.c.} \right) + U \sum_{\alpha \neq \alpha'} n^f_{i\alpha} n^f_{i\alpha'} \tag{1.7}$$

Here, $\epsilon^p_{\boldsymbol{k}\alpha}$ and $n^p_{\boldsymbol{k}\alpha}$ are the energy band and number operator, where the corresponding superscript $p = c$ or $f$ denotes conduction or $f$-electrons, respectively. $V_{\boldsymbol{k}}$ and $U$ denote the strength of the hybridization and onsite Coulomb repulsion interaction, respectively. The band structure for $V = |V_{\boldsymbol{k}}| = 0$ is depicted in Fig. 1.2(a). Based on its localized character of the $f$-moments, $\epsilon^f$ can be regarded as nearly flat. Furthermore, the system is metallic at a sufficiently high temperature relative to $T_{\mathrm{K}}$ because the Fermi energy lies within the conduction band. With decreasing temperature, the Kondo interaction becomes increasingly pronounced, as expressed in Eq. 1.1, and the hybridization term $V$ becomes dominant. When $V$ becomes dominant, these two bands begin to hybridize, leading to the reconstructed band structure shown in Fig. 1.2(b). Here, the dispersion has the direct gap $V$ and indirect gap $\Delta \sim 2V^2/D$, where $D$ is the half band width [9]. It has been shown that $\Delta$ is robustly finite against $U$ [10]. On approaching to the limit of $U \to \infty$ adiabatically, the model is reduced to Eq. 1.5, leading to an insulating ground state with the finite charge gap $\Delta \sim k_{\mathrm{B}}T_{\mathrm{K}}$. When the system is not at half filling or the Fermi level is shifted upwards (downwards) by introducing a moderate amount of electrons (holes), a finite DOS can be induced at the Fermi level. In this case, the quasiparticle band has a much lower curvature than the original conduction band because the conduction electrons acquire an $f$-like character owing to the hybridization. A lower curvature of a band dispersion leads to the heavier effective mass of quasiparticles. On the other hand, when the system is at half filling, the $c$-$f$ hybridized band dispersion with a finite $\Delta$ leads to an insulating ground state; hence, the Kondo lattice becomes a KI.

Owing to the band inversion, the flat $f$-band adiabatically splits into several patches, some of which are partially occupied in the hybridized valence band. This partial occupation of the $f$-orbit results in the intermediate valence (or mixed valence) state widely found in Kondo screened materials including KIs. Taking an example of Yb compounds, in the intermediate valence state, the atomic configuration of magnetic ($Yb^{3+}$) and non-magnetic ($Yb^{2+}$) states are coherently superpositioned spatially and temporally. Therefore, the mean valence for the Yb ion becomes a non-integer ranging from 2 to 3. The intermediate valence state is also one of the topics of research interest in Kondo lattice systems.

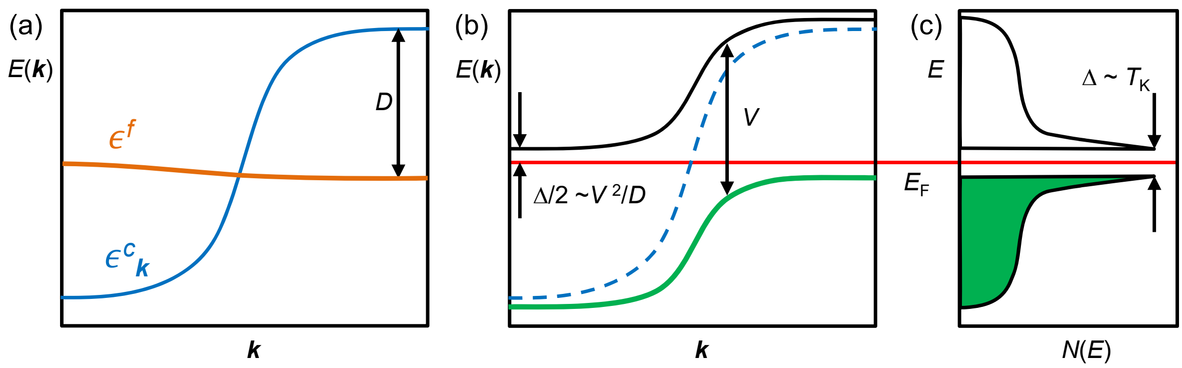


Figure 1.2: (a) Schematic of a conductive and flat band without hybridization, realized in typical Kondo lattice compounds at a temperature above $T_{\mathrm{K}}$. As the Fermi energy crosses the conduction band, the system becomes metallic. (b) The hybridized band structure at a temperature below $T_{\mathrm{K}}$. (c) Energy dependence of the DOS for the hybridized band structure with half filling.

## 1.4 Electronic properties of Kondo lattice systems

### 1.4.1 Thermodynamic and transport properties

Figs. 1.3(a)-(c) show the temperature evolution of the magnetic susceptibility $\chi$, resistivity $\rho$, and electronic specific heat $C_{\mathrm{e}}$ of a KI and heavy FL by red and blue curves, respectively. In the high-temperature regime $T \gg T_{\mathrm{K}}$, these quantities show similar temperature dependences because both systems can be treated as conduction electrons strongly scattering with lattice local moments. $\chi$ shows Curie-Weiss behavior owing to unscreened local moments. The resistivity shows metallic behavior at a sufficiently high temperature, and it exhibits a logarithmic upturn below $T_{\mathrm{K}}$. On decreasing the temperature further, the Kondo lattice acquires coherence below $T^*$, and the system becomes either a heavy FL or a KI according to the band structure and chemical potential.

First, we examine the electronic properties of a heavy FL. As the entropy $S$ of the local moments $R \ln 2$ (here, $R$ is the universal gas constant) vanishes below $T^*$ owing to the Kondo screening, the $C_{\mathrm{e}}/T$ of the conduction electron is also influenced according to

$$S(T) = \int_0^T \frac{C_{\mathrm{e}}(T')}{T'} dT'. \tag{1.8}$$

Therefore, on decreasing the temperature, $C_{\mathrm{e}}/T$ increases, as if the conduction electrons absorb the magnetic entropy of the local moments. To understand the physical picture behind this enhanced $C_{\mathrm{e}}$, it is instructive to express the Sommerfeld coefficient $\gamma = C/T(T \to 0)$ of the 3D electron gas model as

$$\begin{aligned} \gamma &= \frac{\pi^2 k_{\mathrm{B}}^2}{3} N(0) \\ &= \frac{k_{\mathrm{B}}^2 k_{\mathrm{F}}}{3\hbar^2} m^*, \end{aligned} \tag{1.9}$$

where $k_{\mathrm{B}}$ is the Boltzmann constant and $k_{\mathrm{F}}$ is the Fermi wave vector. As $\gamma \propto N(0) \propto m^*$, the enhancement in $\gamma$ implies that the effective mass of the quasiparticle is larger than that of a bare electron. This is why the quasiparticles in Kondo lattices are called heavy fermions. According to Eq. 1.8, $\gamma$ should be of the order of $\sim (R\ln 2)/T_{\mathrm{K}}$ at sufficiently low temperatures. When the Fermi energy crosses the heavy fermion band, the system becomes metallic, and its physical quantities can be well described in the framework of FL theory. As we will see in subsections 1.4.2 and 1.4.3, $\chi$ shows a temperature-independent Pauli paramagnetic response, while $\rho$ decreases in proportion to $A_2T^2$ (the blue curves in Figs. 1.3(a)-(c)). These are the basic properties of a FL.

On the other hand, when the Fermi level is within the Kondo gap, Kondo lattice becomes a KI. It shows a weak magnetic response and activation behavior ($\propto \exp[\Delta/k_{\mathrm{B}}T]$) in resistivity, as indicated by the red curves in Figs. 1.3(a)-(b). One of the main problems addressed in this thesis is the behavior of $C_{\mathrm{e}}/T$ in KIs at low temperature. From a conventional view of insulators, $N(0)$ becomes zero for $T \to 0$. In this case, fermionic excitations must derive from the thermally activated quasiparticles across the gap $\Delta$, leading to $C_{\mathrm{e}}/T \sim \exp(-\Delta/k_{\mathrm{B}}T)$. However, if $C_{\mathrm{e}}/T$ behaves as same as in a heavy FL at high temperature, as indicated by the black curve in Fig. 1.3(c), this conventional gapped behavior violates Eq. 1.8. Therefore, there may be an additional steep peak in $C_e/T$ below $T^*$. Experimentally, however, reliably estimating $C_e/T$ from the total specific heat is difficult, because other contributions, such as the contribution from phonons, become dominant at $T > T_{\mathrm{K}}$ (here, $T_{\mathrm{K}} \approx 100$ K in typical KIs). In fact, the thermodynamics of KIs is poorly understood, and as we will discuss in chapter 5, every model KI discovered so far, to our knowledge, exhibits finite $\gamma$. This is quite surprising given that they show thermally activated behavior in $\rho$, i.e., they are charge insulators with zero DOS at the Fermi level.

### 1.4.2 Kadowaki-Woods ratio

The applicability of the FL theory to heavy fermions implies that the quasiparticles in Kondo lattice systems behave as non-interacting free particles but with a heavier effective mass owing to the renormalization of the Kondo interaction. This picture leads to the universal properties of FLs for various families of materials. The temperature

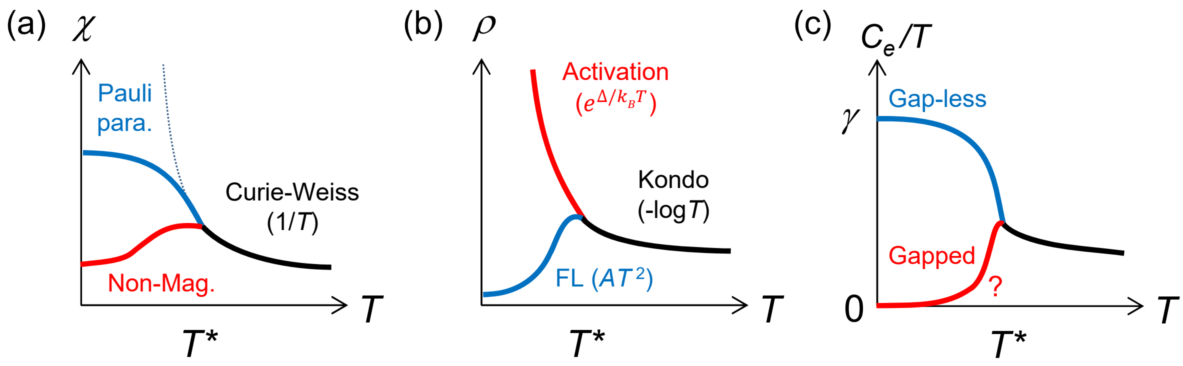


Figure 1.3: Schematics of electronic properties expected in Kondo-screened materials, namely, the Kondo insulator (the red curves) and heavy FL (the blue curves). (a) Magnetic susceptibility, (b) resistivity, and (c) electronic specific heat are shown as a function of temperature.

dependence of resistivity, for example, is given by

$$\rho = \rho_0 + A_2 T^2, \tag{1.10}$$

where $\rho_0$ is the impurity scattering term and the $T^2$ dependence derives from electron-electron interaction with the parameter $A_2$, which determines the probability of the scattering. Kadowaki and Woods [11] first pointed out the universal relationship between $\gamma$ and $A_2$:

$$\frac{A_2}{\gamma^2} = R_{\mathrm{KW}} \equiv 1 \times 10^{-5} \mu\Omega\mathrm{cm}(\mathrm{Kmol/mJ})^2. \tag{1.11}$$

Here, $R_{\mathrm{KW}}$ is known as the Kadowaki-Wood (KW) ratio. Although each physical quantity varies by several orders of magnitude among various classes of materials, this relation holds in a rich variety of systems, such as normal metals, $f$- and $d$-electron-based intermetallic compounds, and oxides. The relation can be understood if one considers the simplest expressions for $A_2$: $A_2 \propto m^{*2}$. Because $\gamma \propto m^*$ from Eq. 1.9, the ratio $R_{\mathrm{KW}}$ does not depend on the renormalization parameter $m^*$, leading to the universal ratio. Although it is also known that the ratio $A_2/\gamma^2$ in a certain category of materials becomes 0.04 times smaller than $R_{\mathrm{KW}}$, the deviation can be generalized by considering the degeneracy of quasiparticles [12].

### 1.4.3 Wilson ratio

One can also find a universal relationship between $\gamma$ and the magnetic susceptibility $\chi$ for FLs. In the FL theory, the main contribution to magnetism is from the Zeeman splitting of the spin-up and spin-down bands, which leads to unbalanced spin population phenomena known as Pauli paramagnetism. This susceptibility is given by

$$\chi_{\text{Pauli}} = \frac{(g\mu_{\text{B}})^2}{4} N(0), \tag{1.12}$$

which is temperature independent, in contrast to the Curie-Weiss behavior. Here, $g$ is the $g$-factor, and $\mu_{\text{B}}$ is the Bohr magneton. Pauli paramagnetism is known as a basic property that metals exhibit at sufficiently low temperatures below the Fermi temperature. According to Eq. 1.9, $\gamma \propto N(0)$ leads to the universal ratio between $\chi_{\text{Pauli}}$ and $\gamma$:

$$R_{\text{W}} = \frac{3}{4}\left(\frac{\mu_{\text{B}} g}{2\pi k_{\text{B}}}\right)^2 \frac{\chi_{\text{Pauli}}}{\gamma}, \tag{1.13}$$

which is known as the Wilson ratio [2]. It has been shown that $R_{\text{W}}$ is close to unity for many FL materials. It is quite surprising that, despite the rich diversity of ground states in correlated metals, the low-temperature physical properties are solely determined by the degree of the renormalization parameter $N(0) \propto m^*$. Therefore, the universal relationships we have discovered thus so far, the KW ratio and Wilson ratio, have been considered direct and fundamental evidence for the validity of the FL theory for various correlated metals.

### 1.4.4 Wiedemann-Franz law

In a FL, quasiparticles carry not only charge but also heat. Therefore, one can expect a quantitative relation between charge transport and thermal transport. To find such a relation, we first express the electric conductivity $\sigma_{xx}$ in a 3D electron gas model is based on the Drude model as

$$\sigma_{xx} = \frac{ne^2\ell}{m^* v_\mathrm{F}} \tag{1.14}$$

$$= \frac{e^2}{3\pi^2\hbar}\ell k_\mathrm{F}^2, \tag{1.15}$$

where $n = k_\mathrm{F}^3/3\pi^2$ is the carrier density, $e$ is the elementary charge, $\ell$ is the mean free path, and $v_\mathrm{F} = \hbar k_\mathrm{F}/m^*$ is the Fermi velocity. The thermal conductivity $\kappa$ of the quasiparticle is also expressed as

$$\kappa_{xx} = \frac{1}{3}\gamma v_\mathrm{F} \ell T. \tag{1.16}$$

By substituting Eq. 1.9, one can obtain

$$\frac{\kappa_{xx}}{T} = \frac{k_\mathrm{B}^2}{9\hbar}\ell k_\mathrm{F}^2. \tag{1.17}$$

Combining Eqs. 1.15 and 1.17 yields

$$\frac{\kappa_{xx}/T}{\sigma_{xx}} = \frac{\pi^2}{3}\left(\frac{k_\mathrm{B}}{e}\right)^2 \equiv L_0 \simeq 2.44\times 10^{-8}\,\mathrm{W\Omega/K^2}. \tag{1.18}$$

The universal constant $L_0$ is known as Lorentz number, and the relation given by Eq. 1.18 is the well-known Wiedemann-Franz (WF) law [13]. This is valid for not only the longitudinal transport component but also the transverse response, i.e., $\kappa_{xy}/\sigma_{xy}T = L_0$. As this law holds for most conventional metals, it is regarded as supporting evidence for the validity of the FL theory. However, it is worth noting that the charge-neutral excitations can contribute to the thermal transport, while they cannot contribute to the electrical conductivity. Indeed, the phonon, which is an emergent excitation mode of lattice vibration, is a typical neutral quasiparticle that can carry heat. Therefore, if the observed ratio $\kappa/\sigma$ is larger than the Lorentz number, it can be interpreted that other neutral quasiparticles contribute to the heat transport. In fact, there are several examples that violate the WF law in strongly correlated electron systems such as quantum spin liquid candidates [14,15] and high-$T_c$ cuprates [16]. In addition, the violation of the WF law has also been reported in the heavy fermion $YbRh_2Si_2$, solely near the magnetic QCP [17, 18], where the $\kappa/\sigma$ becomes smaller than $L_0$. As neutral excitation descriptions are not valid in this case, the anomalous electric transport property is considered to be linked to the non-FL behavior, the mechanism behind which is a central issue in the field of correlated materials [19, 20]

## 1.5 Topological Kondo insulator

The application of the concept of topology to the field of condensed matter physics led to a paradigm shift in research to a new class of materials [21, 22]. A key idea arises from the question of whether it is always possible to adiabatically deform the given wave function of an insulator to another. The answer is no: in the presence of both time-reversal symmetry (TRS) and inversion symmetry (IS), all band insulators can be classified into two with the $Z_2$ invariant $\nu = 0, 1$, and these electronic structures are topologically distinct. The criteria for this classification are given by the Fu-Kane formula [23]:

$$(-1)^{\nu} = \prod_i \zeta(\Lambda_i) = \begin{cases} +1 \text{ trivial (conventional insulator)}, \\ -1 \text{ non-trivial (topological insulator)}, \end{cases} \tag{1.19}$$

where $\zeta(\Lambda_i)$ is the parity eigenvalue of the occupied Bloch states at the time-reversal invariant momentum (TRIM) $\Lambda_i$. As the wave functions of TIs show twisting, these two classes of insulators cannot be connected without breaking some symmetries or closing the band gap. As one can regard vacuum as a conventional insulator, this classification forces the band gap to close at the boundary between TIs and vacuum (i.e., sample edge or surface). This is called bulk-edge correspondence. Hence, the existence of topological order is manifested by the metallic surface state (SS) surrounding the insulating bulk. Because this SS is protected by the symmetry of the underlying crystal, it is robust to perturbations that do not violate the crystalline symmetries. The remarkable feature of this SS is that its dispersion is described as a linear Dirac cone of mass-less fermions. In addition, TRS and IS guarantee band crossing with opposite spin directions at TRIM. This constraint leads to spin-momentum locking, where the spin direction is determined by the momentum of the electron. Furthermore, the backscattering in this surface channel is prohibited owing to the topological protection. Because of the robustness, spin-momentum locking, and topological nature of SS, TIs recently attracted much interest for possible future applications such as efficient spintronics devices, quantum computation, and memory storage with low energy consumption [24].

The integer quantum Hall insulator is a prototypical example of this topological phase of matter, and $Z_2$ TIs were later discovered mostly in materials with strong spin-orbit interaction. In the early stage, the study of TIs focused on materials with weak correlation, most likely because their theoretical treatment to calculate band structures is relatively easy. In 2010, Dzero *et al.* [25] pointed out that a certain type of KI can be topologically non-trivial because they inherently experience band inversions owing to the hybridization of bands with opposite parity. Owing to this new scheme, KIs have been intensively re-investigated as a new family of TIs, where the strong electron correlation drives topological order. These systems are called topological KIs (TKIs) [10].

Because the topological order in KIs is driven by Kondo effect, its topological order also evolves with temperature. Fig. 1.4(a) schematically shows a simplified band structure of KIs at high temperature ($T > T^*$). As the conduction $d$-band crosses the Fermi level $E_\mathrm{F}$, the system becomes metallic with a flat $f$-band. As the temperature decreases to $T < T^*$, the $d$-orbital begins to create a coherent heavy quasiparticle band through the hybridization with the flat $f$-band, as shown in Fig. 1.4(b). Because the conduction $d$-band and localized $f$-band are even and odd in the parity operation, respectively, this hybridization leads to band inversions with different parities, possibly at several TRIMs. According to Eq. 1.19, therefore, if the band inversions occur an odd number of times over the whole Brillouin zone, KIs can be topologically non-trivial. Consequently, the KI can host a metallic SS on its surface, which is protected by TRS and IS, as shown in Fig. 1.4(b). In sections 1.6 and 1.7, we review the electronic properties of candidate TKI materials, $SmB_6$ and $YbB_{12}$, and discuss experimental evidence for the existence of the topological SS.

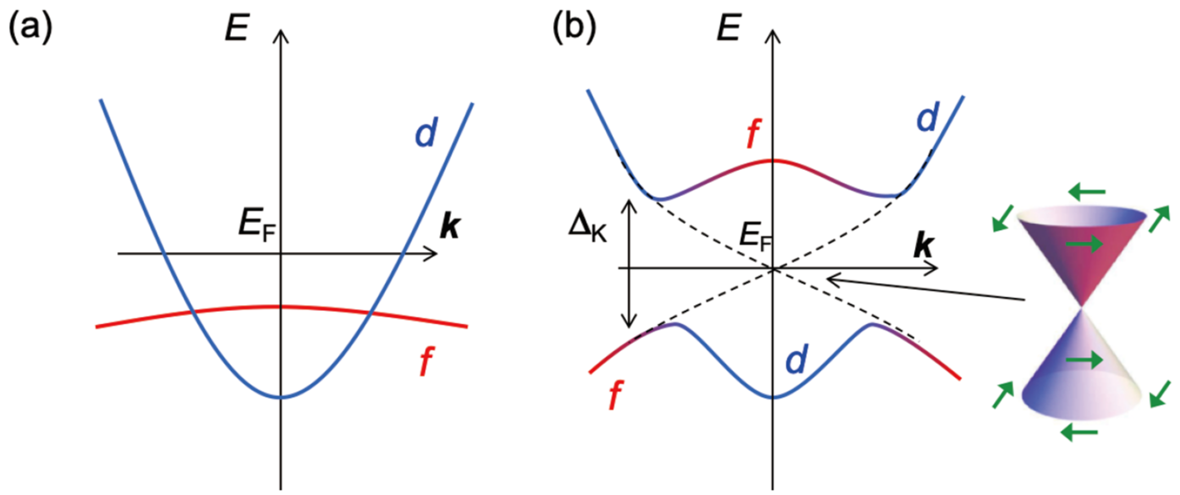


Figure 1.4: Schematics of the band structure of KIs at a (a) high $T$ and (b) low $T$. The dotted lines indicate surface states with Dirac dispersion, where the spins of electrons are locked to their momentum.

## 1.6 $SmB_6$

### 1.6.1 Electronic structure

The first KI, $SmB_6$, was discovered in 1969 [26], and its electrical properties have been intensively studied as a model KI materials and, later, as a correlation-driven TI [27]. It forms a body-centered cubic structure consisting of Sm and $B_6$ octahedra with a lattice constant $a \approx 4.133$ Å, belonging to the $Pm3m$ space group, as shown in Fig. 1.5(a). The corresponding Brillouin zone (BZ) is also shown in Fig. 1.5(b). First-principles calculations using local density approximation (LDA) with the Gutzwiller method revealed that band inversions between the $d$-band and $f$-band are expected to occur at three $\bar{X}$ points [28, 29]. Therefore, according to the Eq. 1.19, these band inversions force $SmB_6$ to be a $Z_2$ non-trivial insulator. The resulting band dispersion of the SS is shown by the red curves in Fig. 1.5(c), and the inset depicts corresponding Fermi surfaces on the (001) surface. Given that most TIs with strong spin-orbit coupling have a single Dirac cone near the Fermi level [21], it is notable that multiple Fermi surfaces appear in $SmB_6$ at the $\bar{\Gamma}$ point and two $\bar{X}$ points. Furthermore, the SS is within the gap and is well separated with the bulk bands, which is favorable to study the intrinsic transport properties of a topological SS.

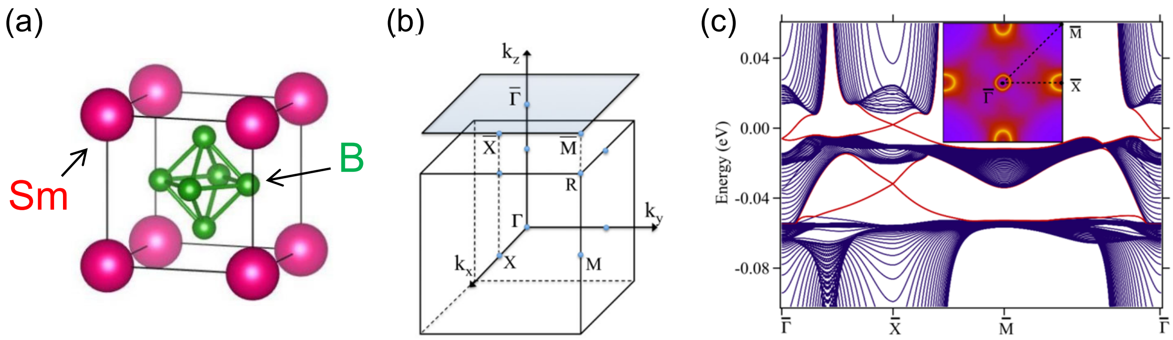


Figure 1.5: (a) Crystal structure of KI $SmB_6$. (b) The bulk and (001) surface Brillouin zone of $SmB_6$. (c) Calculation of the surface and bulk band structures indicated by the red and dark purple curves, respectively. The inset shows Fermi surfaces of the topological SS on the (001) surface. (b), (c) are taken from [28].

The formation of the hybridization gap in $SmB_6$ has been confirmed using various methods. For example, the insulating thermal activation behavior in resistivity has been confirmed [26, 30, 31], and it yields a gap amplitude $\approx 4$ meV [31]. Fig. 1.6(a) shows the Arrhenius plot of $\ln \rho$ vs. $1/T$ [30]. At high temperatures in the range of 100-300 K, $SmB_6$ shows bad metallic behavior because the conduction electrons strongly scatter with the local moments owing to the absence of the coherent hybridization. As the temperature decreases, the resistivity gradually shows insulating behavior down to $\approx 4$ K. It is well known that the resistivity shows saturation at low temperature, which is now discussed in terms of topological SSs. The details of the SS detected by transport measurements will be discussed in subsection 1.6.2. The formation of the hybridization gap can be also observed from the suppression in DOS across the Fermi level by spectroscopy measurements such as scanning tunneling spectroscopy (STM) [32,33], point-contact spectroscopy [34], and angle-resolved photoemission spectroscopy (ARPES) [35–37]. The tunneling conductance $\mathrm{d}I/\mathrm{d}V$, which reflects the local DOS, measured at various temperatures is shown in the upper panel of Fig. 1.6(b). The broad dip structure around $V = 0$ develops with decreasing temperature. This gap formation occurs at $T \approx 100$ K as shown by the lower panel, which displays the gap depth determined by tunneling conductance measurements. Momentum-integrated ARPES data are also displayed in Fig. 1.6(c). The peak structure resulting from the hybridization, which evolves with decreasing temperature, is clearly resolved. Recent ARPES measurements also revealed an in-gap state within the gap, the origin of which is still controversial [38].

$SmB_6$ also shows behavior characteristic of KI in its magnetic properties. Fig.1.7(a) shows the reciprocal magnetic susceptibility $1/\chi$ as a function of temperature [33]. At high temperature, the susceptibility shows paramagnetic Curie-Weiss behavior with a paramagnetic Curie temperature $\approx 50$ K, which is derived from the local moments of $f$-electrons. $1/\chi$ gradually deviates from the $T$-linear behavior below $\approx 120$ K, where the hybridization gap is formed. This Kondo screening prevents magnetic ordering, and $\chi$ shows less $T$-dependent non-magnetic behavior. $\chi$ also exhibits a low-temperature anomaly, which is likely to be associated with the in-gap state. Nuclear

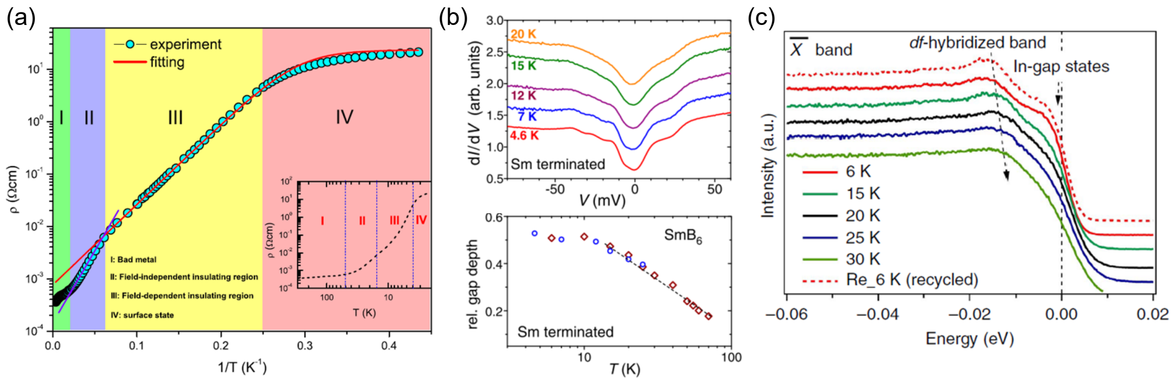


Figure 1.6: Formation of the hybridization gap in $SmB_6$. (a) Arrhenius plot of $\ln \rho$ vs. $1/T$ [30]. (b) Tunneling conductance at various temperatures (upper panel) and the temperature dependence of the gap depth (lower panel) [32]. (c) Momentum-integrated ARPES spectral intensity at the $\bar{X}$ band [35].

magnetic resonance (NMR) measurement also reveals the macroscopic magnetic properties of materials. The Knight shift $K$ is related to the local static susceptibility $\chi_0$ by $K \approx A/\gamma_e\gamma_n\hbar \cdot \chi_0$, where $\gamma_e$ and $\gamma_n$ are the electron and nuclear gyromagnetic ratio, respectively. The reported $^{11}$B NMR Knight shift $K$ also shows a similar temperature dependence as the bulk susceptibility $\chi$ [39]. NMR measurements are also used to obtain information on DOS $N(0)$ from spin-lattice relaxation rates $1/T_1$ by

$$\frac{1}{T_1} \propto N(0)^2 k_{\mathrm{B}} T. \tag{1.20}$$

$1/T_1$ in Fig. 1.7(b) shows suppression below $\approx 100$ K, which is consistent with the gap opening. $1/T_1$ becomes $T$-independent at low temperatures, whereas it remains sensitive to the magnetic field. This anomaly at low temperature also implies a field-dependent in-gap state. Neutron scattering measurements were also conducted to detect magnetic excitations in $SmB_6$. Only residual Bragg scattering and weak phonon scattering were observed, and no magnetic ordering or excitations were resolved down to 200 mK, as shown in Fig. 1.7(c) [40]. These experiments reveal temperature-driven Kondo screening below $T \approx 100$ K and the non-magnetic ground state in $SmB_6$.

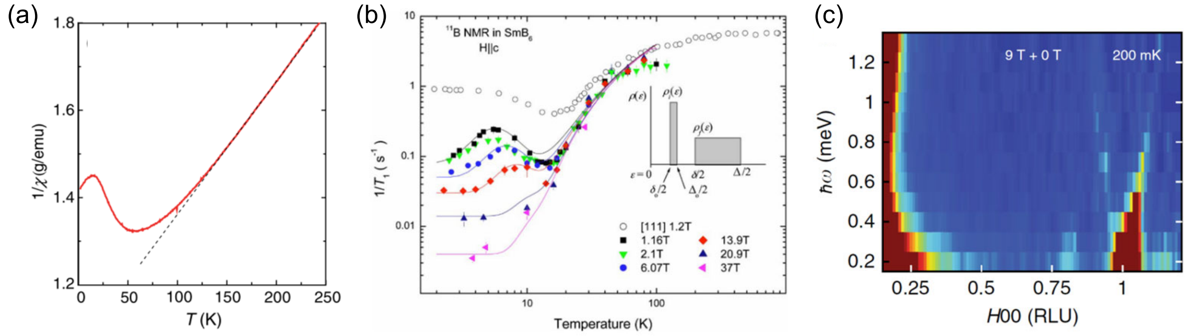


Figure 1.7: (a) Temperature dependence of the reciprocal magnetic susceptibility $1/\chi$ [33]. (b) Temperature dependence of spin-relaxation rates $1/T_1$ in various fields [39]. (c) Neutron scattering intensity mapped with $\hbar\omega$ vs. the reciprocal vector $H$ [40].

### 1.6.2 Topological surface state

The electronic structure of $SmB_6$ is well described in a Kondo screening model and has been regarded as a model KI material, with the exception of the low-temperature anomaly of the in-gap state. We will discuss the topological SS as a possible source of this contribution.

Numerous transport studies on $SmB_6$ were reported in an effort to detect the topological SS from different perspectives, such as the doping effect [41], geometrical effect [31, 42, 43], weak anti-localization (WAL) effect on magnetoresistance (MR) [44], spin-polarization [45], and micro cracks [46]. First, it was proved that the resistance plateau is sensitive to magnetic impurities [41]. As the SS is protected by TRS, it is expected to be destroyed by a magnetic impurity that violates TRS. As shown in Fig. 1.8(a), the resistance plateau shows different behaviors depending on whether the impurity is magnetic. The introduction of 3 % Gd is sufficient to destroy the SS, and the resistivity shows diverging behavior towards $T \to 0$. In contrast, Y-doping does not affect the transport properties.

It has also been shown that the low-temperature transport properties are sensitive to the geometry of samples and contacts. The upper panel of Fig. 1.8(b) displays the resistivity data with various values of the sample thickness $t$ [42]. The residual resistivity $\rho(T \to 0)$ shows a decreasing tendency with decreasing sample thickness. The lower panel shows the relationship between the residual resistance and sample thickness. To explain this behavior, one can regard the TI as a parallel circuit of a 3D bulk and 2D surface (inset of 1.8(b)) as follows:

$$\frac{1}{\rho} = \frac{\ell}{wt}\left(\frac{1}{R_{3\mathrm{D}}} + \frac{1}{R_{2\mathrm{D}}}\right) = \frac{1}{\rho_{3\mathrm{D}}} + \frac{1}{\rho_{2\mathrm{D}}} \cdot \frac{1}{t}. \tag{1.21}$$

As $1/\rho_{3\mathrm{D}} \to 0$ for $T \to 0$, the saturation amplitude corresponds to the second term. Therefore, the linear relationship between the residual resistivity and $t$ provides evidence for a 2D conduction channel in this compound. The separation of the surface and bulk conductance can also be achieved by employing specific configurations of the contacts [43], such as a double-sided Corbino disk [31]. Fig. 1.8(c) shows some such configurations, where the contacts are made from both sides of the crystal. Transport measurements agree with simulation for this configuration, revealing the surface conduction in $SmB_6$. These techniques can also be employed as a powerful tool for detecting bulk conductance even in the surface-dominant regime.

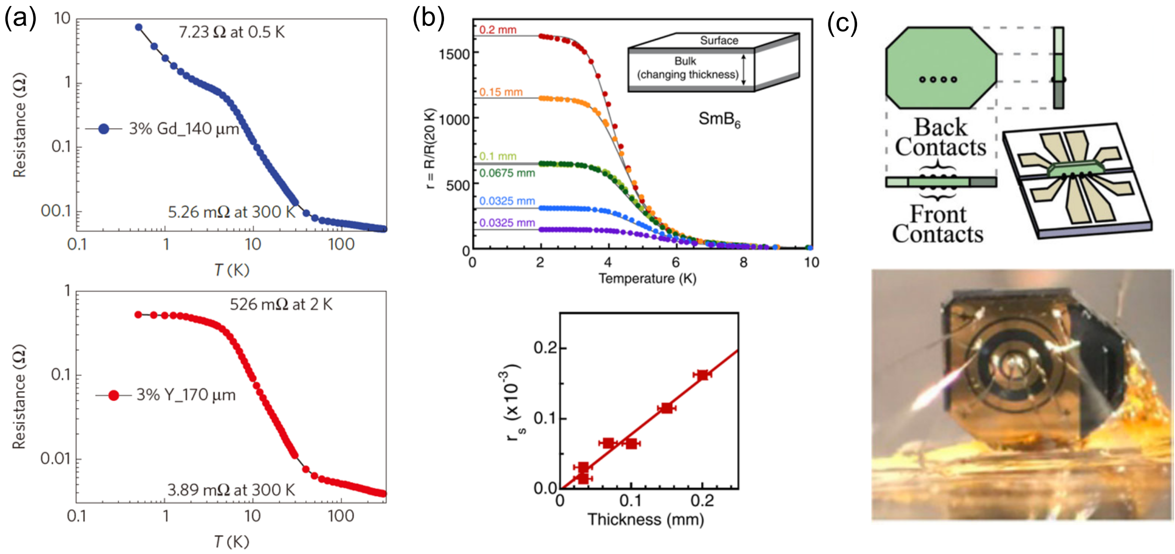


Figure 1.8: Topological SS detected using several types of transport techniques. (a) Temperature dependence of resistivity of Gd-doped (upper panel) and Y-doped (lower panel) $SmB_6$ crystals [41]. (b) Temperature dependence of normalized resistivity with various thickness (upper panel). The lower panel displays the residual resistivity against thicknesses [42]. (c) Examples of special configurations of contacts on the crystal [31,43].

Now, the question is whether the 2D conduction originates from the topological nature. One defining character of the topological SS is that the surface electrons have spin texture, where the spin is locked to its momentum. The detection of this spin polarity using a transport method is important as a possible future device application. The coupling between the spin and its momentum can be manifested in the WAL effect, which is a negative quantum correction to the conductivity. Applying magnetic fields destroys this coherence and leads to a cusp-like feature on MR. Fig. 1.9(a) shows the low-field MR of $SmB_6$ with a magnetic field parallel and perpendicular to the conduction surface [44]. The cusp-like feature is more pronounced when the field is applied perpendicular to the surface plane, which is consistent with the framework of the WAL effect. This result, therefore, implies that the spin of SS is locked to its momentum.

One can probe the spin polarization of the conduction electron more intuitively through spin potentiometric measurements [45]. In such measurements, the contact to the sample is made in a conventional Hall bar geometry, but one of the contacts is replaced by a ferromagnetic metal. As illustrated in Fig. 1.9(b), a current is induced between the gold electrodes on both sides of the crystal, and the transverse voltage is measured between the gold and permalloy magnetic contact (the green region Py). By changing the direction of magnetization of the Py contact, one can also change the potential in different spin directions. The spin-voltage graph shows a finite hysteresis loop in the transverse voltage $V_{xy}$ and the field $H_y$ along the $y$-direction. This result

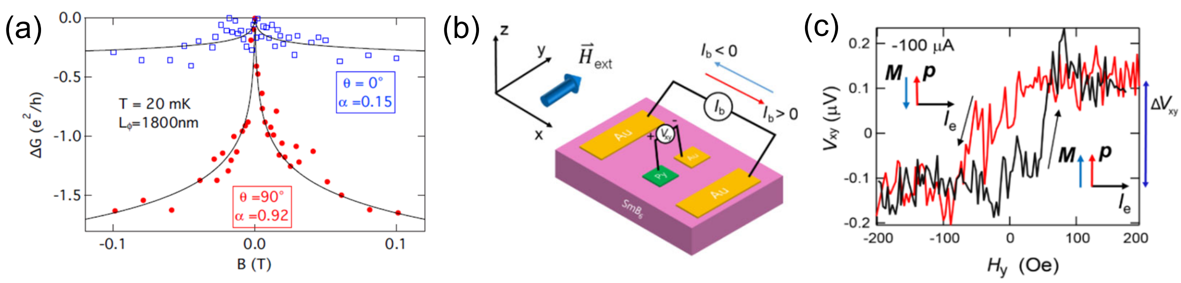


Figure 1.9: Evidence for the spin-momentum locking in the SS of $SmB_6$. (a) Magnetoresistance under a magnetic field applied perpendicular (the red points) and parallel (the blue points) to the major surface plane [47]. (b) Schematic of the setup for the spin potentiometric measurement and (c) the resulting spin voltage [45].

provides evidence that the spin polarization is perpendicular to the current (momentum), which is again consistent with the spin texture we can expect in the topological SS.

More direct evidence for the spin texture in the topological SS band in $SmB_6$ was provided by spin ARPES measurement [47]. A schematic of the Fermi surfaces on the (001) surface and their spin texture is illustrated in Fig. 1.10(a). The spin of the $\beta$ bands located on $\bar{X}$ rotates counterclockwise. The $\beta$ bands are clearly resolved by the ARPES measurement, as shown in Fig. 1.10(b), and the measurement shows good agreement with theoretical calculations. The $\alpha$ band is also resolved at the center of the $\bar{\Gamma}$ point, but the intensity is smaller than that of the $\beta$ bands. Fig. 1.10(c) displays the ARPES intensities along the C1 cut indicated by the red line in Fig. 1.10(b) for each spin direction. The up and down spins along the $x$ direction show a significant difference, and the spin polarization is consistent with the theoretically predicted spin texture. This result provides direct evidence that the SS originates from the non-trivial topology in the bulk electronic state.

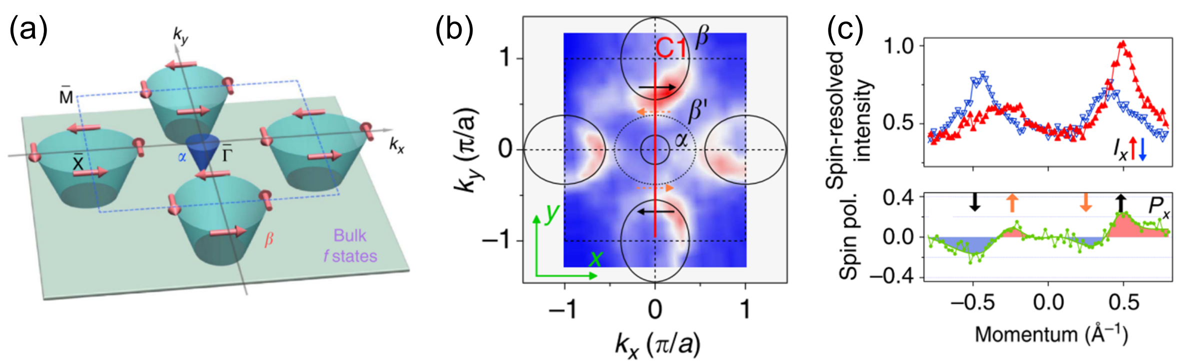


Figure 1.10: Spin texture of the topological SS in $SmB_6$ [47]. (a) Schematics of the SS on the (001) surface. (b) Observed Fermi surfaces of the SS. The red line C1 in the middle is the cut along which the spin polarity is measured. (c) Spin-resolved intensity and spin polarization along the C1 cut.

## 1.7 $YbB_{12}$

### 1.7.1 Electronic structure

$YbB_{12}$ is another prototypical KI. The study on poly-crystalline powders started in the 1970s [48, 49], and the first composition of large single crystals was achieved using the floating zone method in 1998 [50]. The crystalline structure of $YbB_{12}$ is shown in Fig. 1.11(a). It has a face-centered cubic structure consisting of Yb and $B_{12}$ cubo-octahedra with the lattice constant $a \approx 5.28$ Å, belonging to the $Fm\bar{3}m$ space group. The Brillouin zones of the bulk and the (001) surface are shown in Fig. 1.11(b). The topological invariant for this material has also been calculated, but it was shown that the $Z_2$ invariant in $YbB_{12}$ is trivial ($\nu = 0$) because the band inversion occurs twice at three $X$ points [51]. However, one can still expect a topological SS protected by a crystalline symmetry such as mirror symmetry. A topological non-trivial phase protected by a mirror symmetry is called a topological crystalline insulator (TCI) [52], which was first proposed in the strong spin-orbit coupling system $Bi_{1-x}Sb_x$. As the mirror operation classifies the wave function into two subgroups according to its eigenvalue $\eta = \pm i$, one can calculate the Chern number $N_{\pm i}$ for each subgroup. This is analogous to the fact that the TRS yields two subgroups according to the spin, $\pm 1/2$. TCI is a topological phase having a non-zero mirror Chern number, which is defined as $N_{\mathrm{M}} = N_{+i} - N_{-i}$, but zero total Chern number $N = N_{+i} + N_{-i}$. In $YbB_{12}$, it was shown that $N_{\mathrm{M}} = 2$ (non-trivial) owing to the presence of the (010) mirror plane [51]. Therefore, it is expected that $YbB_{12}$ also hosts a topological SS. The result of first-principles calculations for the (001) surface band is displayed in Fig. 1.11(c). As the mirror plane passes through $\bar{M}$-$\bar{\Gamma}$ direction, the degeneracy of the two substates are guaranteed on this plane. Therefore, the Dirac point indicated by the black circle in Fig. 1.11(c) is topologically protected by the mirror symmetry. The surface Dirac cone protected by the finite mirror Chern number also hosts a spin texture as well as an ordinal TI [53]

As a KI, the physical properties of $YbB_{12}$ are quite similar to those of $SmB_6$. The Arrhenius plot of its resistivity is displayed in Fig. 1.12(a). $YbB_{12}$ develops multiple

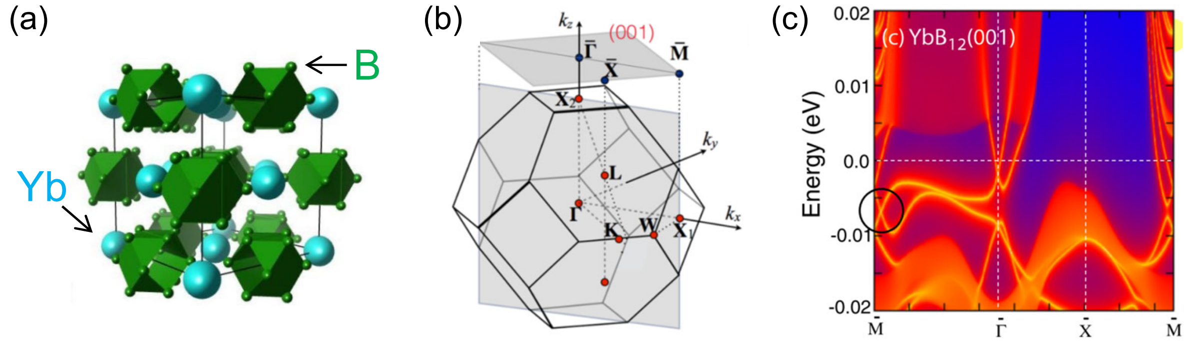


Figure 1.11: (a) Crystal structure of KI $YbB_{12}$. (b) Bulk and (001) surface Brillouin zones of $YbB_{12}$ and the calculation of the (001) surface band [51]. The black circle in (c) marks the Dirac point protected by mirror symmetry.

energy gaps: $\Delta E_1 \sim 15$ meV below $T \approx 40$ K and $\Delta E_2 \sim 4$ meV below $T \approx 15$ K [50]. The low temperature plateau is also observed in $YbB_{12}$, and it can be interpreted as a conduction channel of the topological SS. The formation of the second gap is unique in $YbB_{12}$, and its origin is still under the debate. The magnetic susceptibility $\chi$ also shows the typical Kondo screening behavior [54]. The Curie-Weiss behavior is observed at high temperatures, and $\chi$ shows a peak, which is suppressed below $T^* \approx 80$ K owing to the Kondo screening and finally becomes less $T$-dependent on decreasing the temperature further. The substitution of Yb by Lu moves the system towards a normal metal because Lu does not contain $4f$ electrons. The substitution strongly suppresses the Curie-Weiss behavior, and the system gradually shows Pauli paramagnetic behavior towards the Lu end. This result clearly demonstrates that the $4f$ electrons in Yb ions play an important role in its electronic properties and the observed behavior is entirely consistent with the Kondo physics. This behavior is also supported by the NMR Knight shift [55, 56], as shown in Fig. 1.12(c).

The formation of the hybridization gap was also observed through optical conductivity [57] and photo-emission spectroscopy (PES) measurements [58, 59]. Fig. 1.13(a) displays the optical reflectivity $R(\omega)$ and conductivity $\sigma(\omega)$ [57]. At high temperatures, $R(\omega)$ shows the rather metallic behavior of plasma reflection as $R(\omega = 0) \to 1$. However, at low temperatures, $R(\omega)$ shows a peak feature at $\omega \sim 15$ meV. $\sigma(\omega)$ is also gradually suppressed with decreasing temperature, and at 8 K, $\sigma(\omega)$ becomes almost

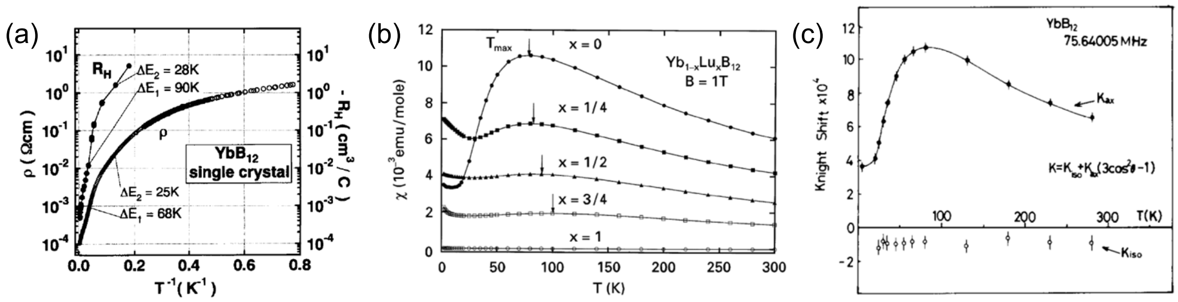


Figure 1.12: (a) Arrhenius plot of the resistivity $\rho$ and Hall coefficient $R_{\mathrm{H}}$ in a single crystal of $YbB_{12}$ [50]. (b) Temperature dependence of the susceptibility of $Yb_{1-x}Lu_xB_{12}$ [54]. (c) Temperature dependence of the $^{11}$B NMR Knight shift [55].

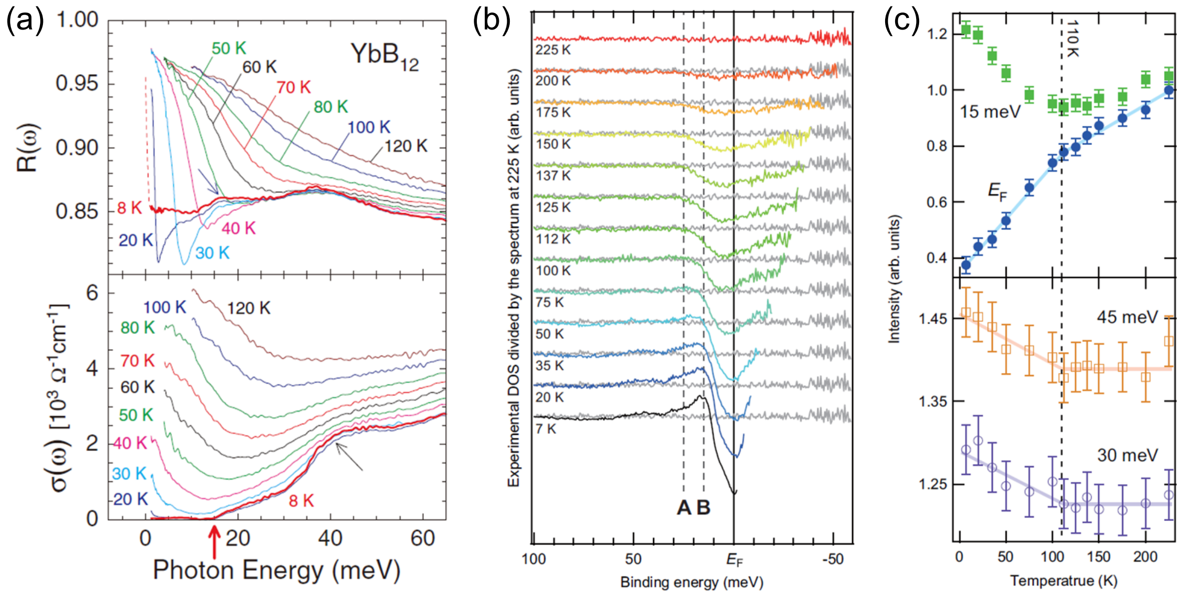


Figure 1.13: Formation of hybridization gap in $YbB_{12}$. (a) Optical reflectivity $R(\omega)$ and conductivity $\sigma(\omega)$ [57]. The red arrow indicates the direct gap amplitude. (b) DOS vs. binding energy determined by laser PES measurements [59] at various temperatures. (c) Temperature dependence of the spectrum intensity obtained from cuts at various binding energies in the data in (b).

zero below $\omega \sim 15$ meV, as indicated by the red arrow in Fig. 1.13(a). These results clearly indicate an optical gap developing below $\approx 80$ K, and the gap amplitude is consistent with other experiments. Another shoulder-like structure around 40 meV corresponds to the indirect gap excitation. Laser PES measurements also provide information on the DOS around $E_{\mathrm{F}}$ [59]. Fig. 1.13(b) clearly shows the development of the multi-gap feature with temperature. Fig. 1.13(c) also shows the temperature dependence of the spectral intensity with different binding energies obtained from the DOS data. The intensity at the inner-gap edge of 15 meV begins to develop below the coherent temperature of 110 K, and the DOS at $\mathrm{E_F}$ decreases owing to the gap formation. Although the coherent temperature is slightly higher than that determined from other experiments, the result strongly supports the opening of the hybridization gap at low temperature.

### 1.7.2 Field-induced insulator-metal transition

The hybridization gap can be suppressed by applying magnetic fields such that the Zeeman energy is sufficient to break the Kondo singlet: $g\mu_{\mathrm{B}}B \sim \Delta$. The high magnetic field can completely destroy the gap so that the system turns metallic. Pulsed high-field measurements reveal this insulator-metal (I-M) transition with the critical field $H_{\text{I-M}}$ ranging from $\mu_0 H_{\mathrm{I-M}} \simeq$ 45-47 T ($\boldsymbol{H}||[100]$) to 55-59 T ($\boldsymbol{H}||[110]$) [60–63]. Fig. 1.14(a)-(c) shows the field dependence of resistivity [63], specific heat [62], and magnetization [61]. Reflecting the gap suppression, a negative MR is observed up to $H_{\text{I-M}}$. In the higher-field regime above $H_{\text{I-M}}$, $\Delta$ completely vanishes, and the system shows a negligibly small MR, indicating a field-induced metallic phase. Although not mentioned in this early paper [63], the oscillating behavior observed in an $x = 0$ sample around 40-55 T may be the signature of quantum oscillations, which will be discussed in more detail in chapter 3. Corresponding to the phase transition, the specific heat $C$ is also dramatically and discontinuously enhanced at the critical field. The finite large Sommerfeld coefficient $\gamma$ at the high-field regime clearly indicates that the DOS at $E_{\mathrm{F}}$ is induced in the metallic phase. The field induced metallic phase with the large $\gamma$ is termed the Kondo metal phase because the Kondo correlation does not break down at $H_{\text{I-M}}$ and robustly remains even in the metallic phase. The magnetization $M$ also shows a kink anomaly at the critical field, and $M$ shows a strong upturn in the Kondo metal regime. In the powder sample, a second transition at approximately 100 T is also observed. Little is known about this phase because the excessively strong field limits the types of measurements we can conduct.

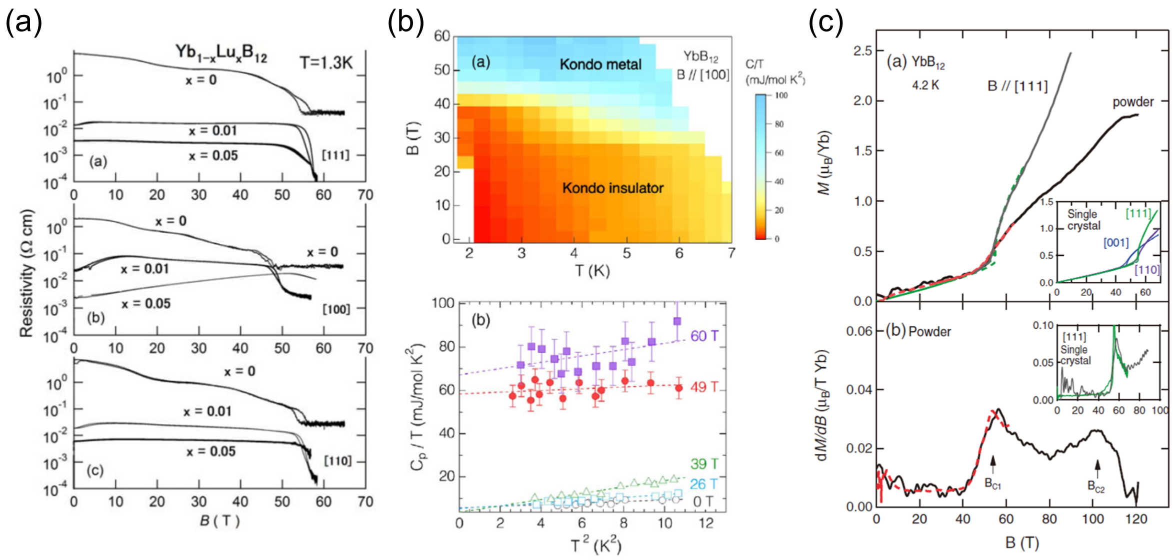


Figure 1.14: High-field properties of $YbB_{12}$. (a) Field dependence of the series of single crystals $Yb_{1-x}Lu_xB_{12}$ with different field directions [63]. (b) $B$-$T$ mapping of specific heat (upper panel). The lower panel displays $C/T$ vs. $T^2$. The intercept at $T^2 \to 0$ corresponds to the quasiparticle contribution in $C$ [62]. (c) Field dependence of magnetization and its derivative with respect to the field [61].

### 1.7.3 Topological surface state

While $SmB_6$ has been intensively studied as the first candidate TKI, research on $YbB_{12}$ is rather scarce. A recent ARPES measurement on a clean (001) surface revealed surface band dispersion, which is consistent with a topological SS [64]. As shown in Fig. 1.15(a), the ARPES intensity at a biding energy of 200 meV shows distinct square constant-energy contours at 20 K. As indicated by the red dotted line, the photon energy does not affect the in-plane momentum of this band dispersion. This result indicates that the band does not host dispersion along $k_z$, demonstrating a 2D surface metallic state. Furthermore, this surface band shows hybridization with the flat $f$-band below $T^*$, as shown in Fig. 1.15(b). The reconstructed band dispersion along the [100] direction taken with a photon energy of 16.5 eV is shown in Fig. 1.15(c). The surface band clearly crosses the Fermi level at $k_{||[100]} \sim 0.18$ (Å$^{-1}$). This dispersion appears to connect to the $f$-band at the $\bar{\Gamma}$ point at the binding energy $\sim 35$ meV, leading to the degeneracy at TRIM, which is consistent with a topological SS. Although the surface band dispersion shows good agreement with that of a topological SS, the spin texture in the SS of $YbB_{12}$ has been scarcely studied thus far, especially from the perspective of transport properties.

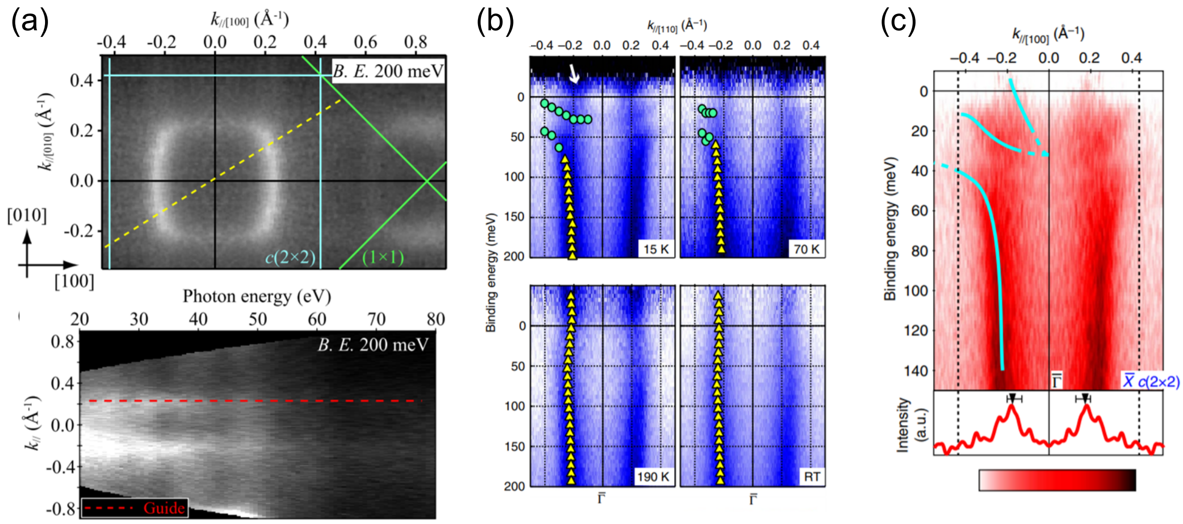


Figure 1.15: ARPES data acquired from a clean (001) surface of $YbB_{12}$ [64]. (a) ARPES intensity map a the binding energy of 200 meV. (b) Band dispersion at different temperatures ranging from room temperature to 15 K. (c) ARPES data taken with a photon energy of 16.5 eV. The bottom panel shows the momentum distribution curve near $E_F = \pm 10$ meV.

# 2 Unconventional quantum oscillations in $SmB_6$

## 2.1 Introduction

A Fermi surface sets the boundary of occupied and unoccupied electron states in momentum space at zero temperature. It is well established that the presence of a Fermi surface is the definitive character of metals; hence, insulators (as well as semiconductors) do not have a Fermi surface. Most of the physical properties of a certain material are determined by its electrical ground state and how its electrons excite from that state. As electrons (fermions) follow the Pauli exclusion principle, only the electrons near the Fermi surface can participate in the excitations. This is why most of the physical properties of metals are determined by the geometry of the Fermi surface. Therefore, studying the geometry of the Fermi surface, which is also called Fermiology, is the one of the most promising ways to understand a metal from a physical perspective.

Quantum oscillation (QO) is a phenomenon in which certain physical quantities, such as magnetization and resistivity, show periodic oscillations with respect to the reciprocal of external fields. QO is driven by the Landau quantization of conduction electrons in strong fields, and reflects much information about the Fermi surface. Intuitively, this is because one can scan and map the electron states in momentum space by modulating the Landau level. Therefore, QOs have been employed as pivotal experimental tools in Fermiology. Recently, it has been reported that some TKIs such as $SmB_6$ and $YbB_{12}$ show QOs, although they are insulators. These observations have attracted great interest in the condensed matter physics community because these KIs are the first experimental counterexamples for insulators that may host Fermi surfaces. In this chapter, we review the recent observations of unconventional QOs in TKIs and the theories proposed to explain how they arise in insulators.

## 2.2 Quantum oscillations

In classical mechanics, the motion of electrons under magnetic fields can be described as a cyclotron motion owing to the Lorentz force. This closed orbit is manifested in the Landau quantization of energy levels (Landau levels) in the framework of quantum mechanics. The Schrödinger equation for a stationary charged particle in a 3D system is given by

$$\frac{1}{2m}(-i\hbar\nabla + e\mathbf{A})^2\psi = E\psi. \tag{2.1}$$

When a magnetic field is applied parallel to the $z$-axis, the vector potential can be expressed as $\mathbf{A} = (0, Bx, 0)$. The Schrödinger equation can then be transformed into

$$\frac{\partial^2\tilde{\psi}}{\partial x^2} + \left[\frac{2mE}{\hbar^2} - k_z^2 - \left(\frac{eBx}{\hbar} - k_y\right)^2\right]\tilde{\psi} = 0, \tag{2.2}$$

where $\tilde{\psi} = \psi \exp[i(k_y y + k_z z)]$. By substituting $\xi_n = E - \hbar^2 k_z^2/2m$, $x' = x - \hbar k_y/eB$, and $\omega_\mathrm{c} = eB/m$, we obtain the equation of motion for the harmonic oscillator:

$$\frac{\partial^2\tilde{\psi}}{\partial x^2} + \frac{2m}{\hbar^2}\left[\xi_n - \frac{1}{2}m\omega_\mathrm{c}^2 x'^2\right]\tilde{\psi} = 0. \tag{2.3}$$

The energy eigenvalue is then simply given by

$$E = \xi_n + E(k_z) = \left(n + \frac{1}{2}\right)\hbar\omega_\mathrm{c} + \frac{\hbar^2 k_z^2}{2m}. \tag{2.4}$$

Therefore, the energy levels for the motion within the $xy$-plane split into subbands with the energy difference $\Delta E = \hbar\omega_\mathrm{c}$. Fig.2.1 shows schematics of the electron states of a 3D electron gas (a) without and (b) with an applied external field. Because the motion along the $z$-axis is not quantized, the energy levels form coaxial cylinders of Landau tubes along the $z$-axis.

The correspondence principle gives the orbit-area quantization condition [65], leading

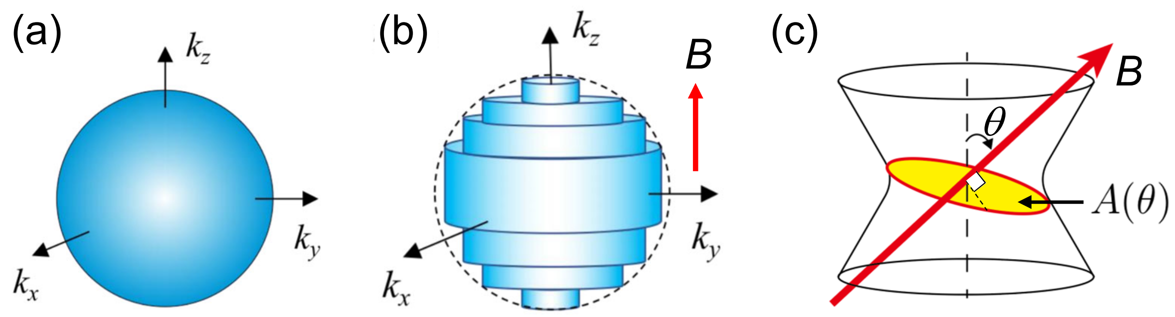


Figure 2.1: Schematic of the spherical Fermi surface of a 3D free electron gas (a) without external fields and (b) under a magnetic field along the $z$-direction. (c) Extreme cross-section $S(\theta)$ of the Fermi surface perpendicular to the magnetic field tilted by $\theta$ from the $z$-axis.

to the following relation between the cross-section of the $n$-th cylinder $A_n$ and $n$:

$$A_n = (n + \gamma)\frac{2\pi eB}{\hbar}. \tag{2.5}$$

As the field increases and energy splitting broadens, the outermost cylinders below the Fermi level are pushed out into the unoccupied states. This depopulation of the electrons near the Fermi level occurs periodically with respect to the change in the magnetic field, and its frequency $F$ is given by

$$F = \frac{A(\theta)}{2\pi e\hbar}, \tag{2.6}$$

where $A(\theta)$ is the extreme cross-section of the Fermi surface perpendicular to the field direction, as shown in Fig. 2.1(c). Eq. 2.6 is also known as Onsager's rule, according to which the frequency of the quantization is proportional to the cross-section of the Fermi surface. Consequently, the thermodynamic potential shows sets of oscillations as a function of the reciprocal of the field; consequently, some physical properties such as the thermodynamic and transport quantities of metals also show oscillations. The QOs in magnetization are called the de Haas-van Alphen (dHvA) effect, while the QOs in resistivity are referred to as the Shubnikov-de Haas (SdH) effect.

It is worth noting that Eq. 2.6 holds even if $A_n$ is $B$-dependent. For the $B$-dependent cross-section $A(B_n)$, Eq. 2.5 can be expressed as

$$A(B_n) = (n + \gamma)\frac{2\pi e B_n}{\hbar}. \tag{2.7}$$

A set of equations for n and n+1 can be combined to produce

$$\frac{A(B_{n+1})}{B_{n+1}} - \frac{A(B_n)}{B_n} = \frac{2\pi e}{\hbar}. \tag{2.8}$$

Moreover, $F$ is field-dependent, the quantization condition should be satisfied when the field is equal to $F(B_n)$, i.e., $F(B_n)/B_n = n + \gamma$, which yields

$$\frac{F(B_{n+1})}{B_{n+1}} - \frac{F(B_n)}{B_n} = 1. \tag{2.9}$$

Therefore, Eqs. 2.8 and 2.9 demonstrate that Onsager's rule still holds:

$$F(B) = \frac{\hbar}{2\pi e} A(B). \tag{2.10}$$

The QOs are formulated as the well-known Lifshitz-Kosevich (LK) formula [66, 67], and the oscillatory part of magnetization is given by

$$M_{\text{osc}} = -\sum_{r=1}^{\infty} \frac{1}{r^{3/2}} M_r \sin\left[2\pi r\left(\frac{F}{B} - \frac{1}{2} \pm \frac{\pi}{4}\right)\right], \tag{2.11}$$

where the + and − signs in the phase shift of $\pm\pi/4$ correspond to the minimum and maximum cross-section area, respectively. The amplitudes of the oscillations $M_r$ are given by

$$M_r = \left(\frac{e}{2\pi\hbar}\right)^{3/2} \frac{A(\theta)B^{1/2}}{\pi^2 m^* |A''|_{\text{extr}}^{1/2}} R_T(r) R_{\text{D}}(r) R_S(r), \tag{2.12}$$

where $m^*$ is the cyclotron effective mass and $|A''|_{\text{extr}} = (\partial^2 S/\partial p_B^2)_{\text{extr}}$ is the curvature of the Fermi surface around the cross-section along the $B$ direction. Eq. 2.12 also contains three types of damping factors, namely, temperature, Dingle, and spin damping, which are denoted as $R_T(r)$, $R_{\text{D}}(r)$, and $R_S(r)$, respectively. These three factors arise from the broadening of the Landau levels driven by the finite thermal energy in the Fermi-

Dirac distribution function, impurity scattering, and Zeeman splitting of opposite spin bands, respectively. $R_T(r)$ can be expressed as,

$$R_T(r) = \frac{2\pi^2 r k_{\mathrm{B}} T/(\hbar\omega_{\mathrm{c}})}{\sinh[2\pi^2 r k_{\mathrm{B}} T/(\hbar\omega_{\mathrm{c}})]} = \frac{K r \mu T/B}{\sinh(K r \mu T/B)}, \tag{2.13}$$

where $\mu = m^*/m_0$ and $K \equiv 2\pi^2 k_{\mathrm{B}} m_0/(\hbar e) \sim 14.7$ T/K. Therefore, by utilizing $\mu$ as a fitting parameter, one can estimate the effective mass of electrons from the temperature dependence of the oscillatory amplitudes. The Dingle-damping factor is given by

$$R_{\mathrm{D}}(r) = \exp\left(-\frac{\pi r}{\omega_{\mathrm{c}}\tau}\right) = \exp(-B_{\mathrm{c}}/B) = \exp(-K r \mu T_{\mathrm{D}}/B), \tag{2.14}$$

where $T_{\mathrm{D}} = \hbar/(2\pi k_{\mathrm{B}}\tau)$ is the Dingle factor related to the impurity scattering energy. The characteristic field found in the numerator of the exponent $B_{\mathrm{c}} = K r \mu T_{\mathrm{D}}$ is the field above which QOs are visible. The field $B_c$ can also be expressed as the reciprocal of the mobility $e\tau/m^*$. By utilizing $T_{\mathrm{D}}$ as a fitting parameter again, one can estimate the scattering time $\tau$ from the field dependence of the oscillatory amplitudes. Finally, the spin-damping factor is written as

$$R_S(r) = \cos\left(\frac{\pi}{2} r g \mu\right), \tag{2.15}$$

which contains the $g$-factor. As shown above, the measurements of QOs provide rich information on the geometry of the Fermi surface, effective mass, scattering time, and $g$-factor of metals. According to Eqs. 2.13 and 2.14, the oscillation amplitude becomes visible when $\hbar\omega_{\mathrm{c}} > k_{\mathrm{B}}T$ and $\hbar\omega_{\mathrm{c}} > \hbar/\tau$. The first condition is rewritten as $B/T > k_{\mathrm{B}} m^*/\hbar e$, suggesting that sufficiently large magnetic fields and low temperatures are required to experimentally resolve QOs. Moreover, when the cyclotron mass $m^*$ is low, QOs are relatively easy to detect. The second condition from the Dingle factor leads $\tau > 1/\omega_{\mathrm{c}}$, implying that an electron must form a closed cyclotron orbit before it is scattered. This condition necessitates a clean crystal with a long scattering time.

## 2.3 Quantum oscillations in $SmB_6$

### 2.3.1 Results reported by the Michigan group

The first observations of QOs in the KI $SmB_6$ was reported by Li *et al.* [68] from the University of Michigan. They synthesized single crystals of $SmB_6$ by using the aluminum flux method and measured the magnetic torque $\boldsymbol{\tau}$ by using the capacitance cantilever method. The field dependence of $\boldsymbol{\tau}$ and a schematic of the experimental setup are shown in the main panel and inset of Fig.2.2(a), respectively. As $\boldsymbol{\tau} = \boldsymbol{M} \times \boldsymbol{H}$, the oscillations in $\boldsymbol{\tau}$ are a direct consequence of the dHvA effect. As shown clearly in Fig. 2.2(a), the magnetization shows clear oscillations at high fields. By performing a fast Fourier transformation (FFT), one can separate multiple components of oscillations with different frequencies $F$. In Fig. 2.2(b), one of the characteristic frequencies, $F^{\beta}$, is plotted as a function of the field angle $\phi$. First, $F^{\beta}(T)$ shows four-fold rotational symmetry, which is expected from the cubic crystalline structure of $SmB_6$. Most importantly, as shown by the black curves in Fig. 2.2(b), all the data can be perfectly fitted by

$$F = \frac{F_0}{\cos(\phi - \pi/4 - n\pi/2)}, \tag{2.16}$$

which is the angular dependence of the cross-section expected from the cylindrical Fermi surface of 2D electrons. This field dependence strongly suggests that the dHvA effect originates from the 2D electronic state, which is most likely to have originated from the topological SS. The amplitude of the oscillations are shown as a function of temperature in Fig. 2.2(c). As the oscillations contain three different frequencies and, thereby, different Fermi pockets $\alpha$, $\beta$, and $\gamma$, one must separate each oscillatory component by performing FFT. As shown by the solid curves in Fig. 2.2(c), the normalized amplitudes follow the LK formula given by Eq. 2.13, which extracts the effective mass $m^* = 0.12$-$0.19m_0$. The observed LK behavior indicates that the quasiparticles participating in the dHvA effect follow the Fermi-Dirac statistics, and hence, they are fermions. The low effective mass of roughly 0.1 times that of a free electron is rather surprising, as the strong correlations in KI tend to yield heavy fermions with a large $m^*$.

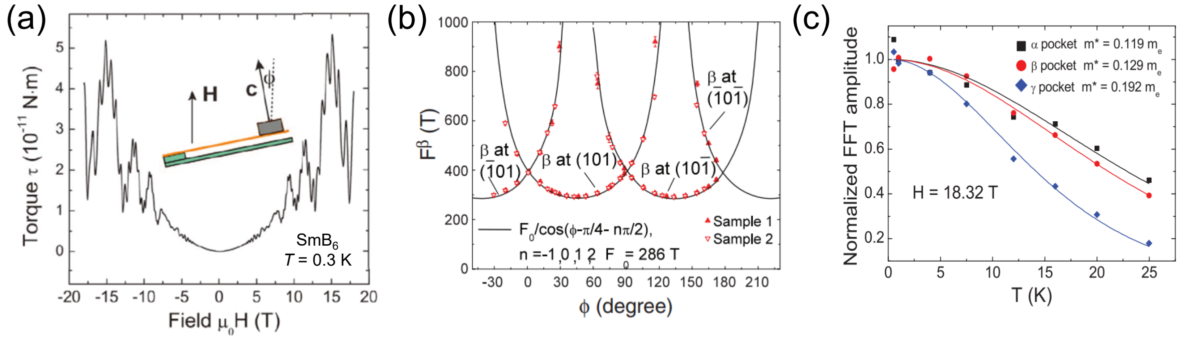


Figure 2.2: The dHvA effect observed in a flux-grown $SmB_6$ crystal [68]. (a) Field dependence of the magnetic torque. (b) Angular dependence of the FFT frequency. (c) Temperature dependence of the normalized FFT amplitudes for three different Fermi pockets. The solid curves represent the LK fitting given by Eq. 2.13.

### 2.3.2 Results reported by the Cambridge group

Soon after the first report by the Michigan group, Tan *et al.* [69] from Cambridge University also reported the dHvA effect in $SmB_6$. Although they found the same phenomenon in the same compounds, they presented some surprising results, which were not observed in the first report. While they employed the same types of experimental techniques, the single crystals of $SmB_6$ used in their study were prepared using the floating zone method. The left panel of Fig. 2.3(a) shows the angular mapping of the FFT frequency extracted by the dHvA effects of $SmB_6$. In addition to the low-frequency oscillations around $F \sim 10^2$-$10^3$ T, which were also observed by the Michigan group, they found other oscillations with higher frequencies $F \sim 10^3$-$10^4$ T. The dHvA frequencies of the isostructual metallic compound $LaB_6$ are shown in the right panel of Fig. 2.3(a). It was pointed out that the observed higher frequency in $SmB_6$ and its angular dependence is akin to that of $LaB_6$, which implies that these two materials have similar Fermi surfaces. As one can regard $LaB_6$ as $SmB_6$ without hybridization owing to the absence of $f$-electrons, its Fermi surfaces are nearly spherical, large pockets of conduction bands located on the $X$ points, as illustrated in Fig. 2.3(b). This similarity of the Fermi surfaces is quite surprising because such a large 3D Fermi surface rules out the possibility that the dHvA effect with the higher frequency originates from the SS. Therefore, the Cambridge group's results suggest that $SmB_6$ somehow possesses an unconventional 3D bulk Fermi surface, although it is a charge insulator. As this was the first experimentally observed insulator that shows QOs, the oscillations are occasionally referred to as unconventional QOs.

Another surprising feature of this unconventional dHvA effect is its non-LK behavior in the temperature damping factor. The temperature dependence of the amplitude of the oscillations is shown in Fig. 2.3(c), and the red curve in the inset shows the LK fit. A good agreement with the LK curve can be found around 1-15 K, yielding the light effective mass of $m^* \approx 0.18m_0$. This $m^*$ is rather close to that observed by the Michigan group. However, the amplitude strongly deviates from the LK fit below $\sim$ 1 K, showing a non-monotonic, sharp upturn towards low temperatures. This unusual temperature dependence of amplitude may indicate that the quasiparticles do not follow the Fermi-Dirac distribution, or that multiple types of quasiparticles with different $m^*$ are involved in the dHvA signals. The theoretical approach for this non-LK behavior will be discussed in subsection 2.4.

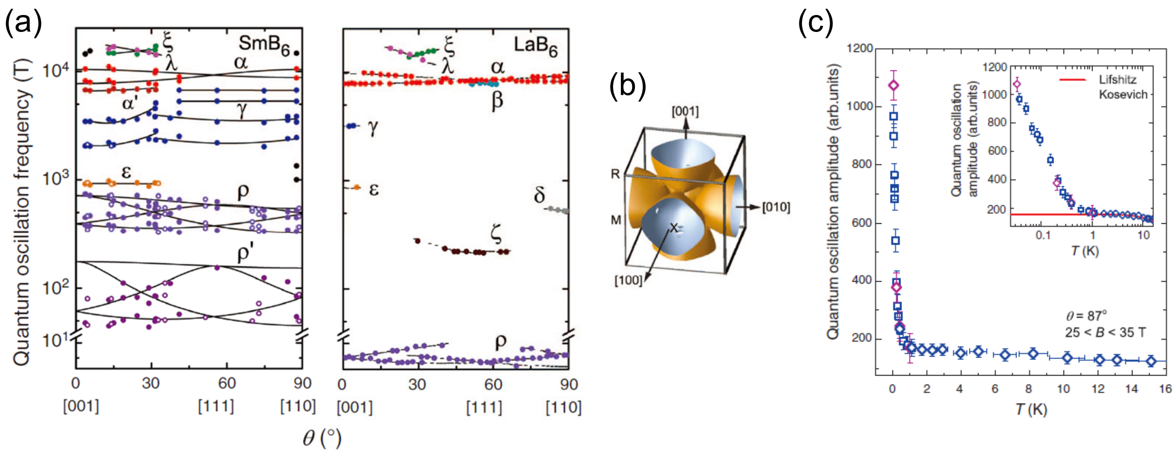


Figure 2.3: Unconventional dHvA effect observed in $SmB_6$ crystals grown using the floating-zone method [69]. (a) Angular dependence of the dHvA frequency for $SmB_6$ (left panel) and $LaB_6$ (right panel). (b) An illustration of the Fermi surface of $LaB_6$. (c) Temperature dependence of the oscillation amplitude. The red curve in the inset represents the LK fitting of Eq. 2.13.

### 2.3.3 Problems related to the QOs in $SmB_6$

Although the observations of the dHvA effect provide convincing evidence for the Fermi surfaces of $SmB_6$, which may originate from the topological SS or exotic 3D insulating phase, several problems remain. The first problem is why the QOs in resistivity (SdH effects) have never observed so far. The MR of the flux-grown sample was also reported by the Michigan group [68] (Fig. 2.4(a)). Although the dHvA effects are clearly resolved below $T \sim 25$ K and above $B \sim 5$ T, no evidence of SdH oscillations was detected, even at the lowest temperature of $T \sim 350$ mK and fields of up to $\sim 45$ T. Given the low $m^*$ and high mobility of the quasiparticles estimated from the dHvA signals, the absence of the SdH signal in such conditions is puzzling. A possible explanation for this issue is that the scattering probability is not significantly affected by the Landau quantization, leading to less pronounced SdH signals, while the dHvA effect is a direct consequence of the oscillations in the thermodynamic potential. However, this idea has not been quantitatively justified, and the lack of the SdH signal has been under debate.

The second issue is whether the dHvA effects are intrinsic properties of $SmB_6$. As the difference between the results of the Michigan group and Cambridge group lies in the method of crystal growth, it has been suggested that the qualitative difference might have originated from the sample quality or an extrinsic effect induced by the impurity of the aluminum flux. From this perspective, torque measurements on $SmB_6$ were reexamined by Thomas *et al.* [70] from Los Alamos National Laboratory. To verify the effect of the aluminum flux more clearly, they prepared crystals with an intentionally large amount of aluminum flux, as shown in Fig. 2.4(b). The torque signal with respect to the field is shown by the blue curve in Fig. 2.4(c). The crystal shows a clear dHvA effect, and the angular dependence of this frequency and the temperature dependence of the amplitude are quite similar to those reported by the Michigan group. Furthermore, on polishing the as-grown crystal to remove the flux, the oscillations in torque decrease and finally vanish within the experimental resolution. The results suggest that the 2D features of the dHvA effect originate from the extrinsic metallic aluminum phase and are not intrinsic to $SmB_6$.

On the other hand, the Cambridge group recently reported another experiment [71], where they argue that the dHvA effect is an intrinsic property of the insulating bulk of $SmB_6$, as reported earlier. They prepared an extremely clean single crystal of $SmB_6$ by using the floating-zone method. The crystals show a lower concentration of impurities, better thermal conductivity, and an inverse residual resistivity ratio higher than those of previously investigated samples by over an order of magnitude, demonstrating that the new sample is of much higher quality. In the newly prepared crystals, they reproduced dHvA signals similar to those in the previous report [69]. The oscillation amplitudes are comparable to that of the paramagnetic response, indicating that the dHvA effects originate from a major portion of the sample, i.e., the bulk. Moreover, they also show the dHvA signals of a single crystal of elemental aluminum, pointing out that their frequencies are essentially different from that observed in $SmB_6$.

As seen thus far, there is still no consensus on whether the QOs have a surface or bulk origin; it is also unclear whether the dHvA effect is intrinsic to $SmB_6$. It is, thus, essential to address these issues for understanding the nature of unconventional QOs in KIs, and further investigation on other materials is necessary.

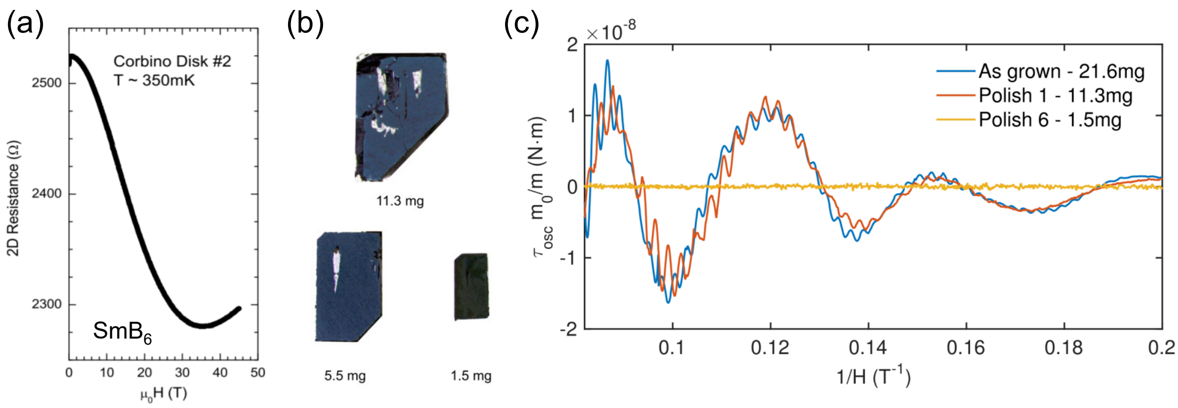


Figure 2.4: (a) Magnetoresistance of $SmB_6$ [68]. (b) $SmB_6$ crystal with intentionally embedded aluminum impurities. The sample was polished into small pieces with a low concentration of aluminum. (c) dHvA data observed in the samples shown in (b) [70].

## 2.4 Theories for the unconventional quantum oscillations

After the discovery of the dHvA effects in $SmB_6$, a substantial number of theories have been proposed to explain this phenomenon. In this section, we review some of the theories to examine how QOs can arise from the insulating bulk and how these theories can be verified experimentally. Some are based on the intrinsic properties of narrow-gap insulators, while some assume certain types of charge-neutral quasiparticles.

### 2.4.1 QOs without a bulk Fermi surface

It was pointed out that the gap amplitude of KIs shows oscillatory narrowing under external fields owing to the inverted band structure resulting from the $c$-$f$ hybridization [72]. In a simple metal with a parabolic conduction band, the Landau tubes periodically swell out and pass through the chemical potential $\mu$ as the field increases, leading to the periodic modulation of the low-energy density of states (LEDOS), as shown in Fig. 2.5(a). In KIs, on the other hand, the Landau tubes first approach $\mu$ but are reflected at the band edge; consequently, they move away from $\mu$ (Fig. 2.5(b)). In accordance with this gap narrowing, the LEDOS also oscillates. In a narrow-gap insulator, thermally activated quasiparticles show periodic oscillations in the thermodynamic potential, leading to the magnetic QOs. A key ingredient for this theory is that only the inverted band structure is preferred in KIs; therefore, any narrow-gap insulators with band inversion would show QOs irrespective of their topological nature. It is worth noting that this thermal activation leads to a exponential decrease in the oscillatory amplitude at the absolute zero temperature.

There are also several theories based on the topological SS as a source of the QOs [73]. In this scheme, the non-LK behavior observed in $SmB_6$ can be explained by the Kondo breakdown of the SS. The band structures of $SmB_6$ are calculated by changing the parameter $\langle b_s \rangle^2 / \langle b \rangle^2$, which indicates the amount of hybridization between the local moments on the surface and the topological SS. Fig. 2.5(c) and (d) show the resulting

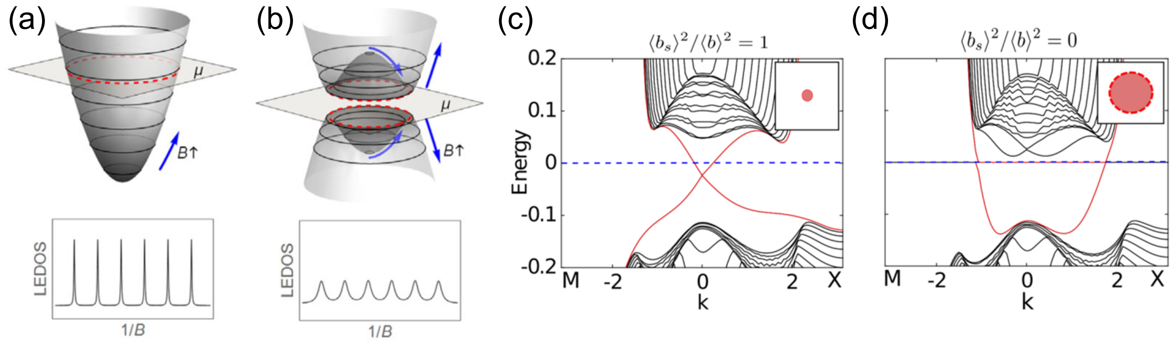


Figure 2.5: Schematic of the band structure and the corresponding LEDOS in (a) metals and (b) KIs [72]. The blue arrow indicates the direction to which the Landau level moves as the field increases. (c), (d) Calculated surface (red lines) and bulk (black lines) band structures of KI with different hybridization strengths on the SS [73].

band structure of the bulk and the SS with black and red curves, respectively, and their insets depict the Fermi surface of the SS. For $\langle b_s\rangle^2/\langle b\rangle^2 = 1$, the SS is completely hybridized to the local moments on the surface, leading to surface electrons with a large $m^*$ forming a small Fermi pocket. With decreasing temperature, $\langle b_s\rangle^2/\langle b\rangle^2$ decreases and the surface electrons decouple to the local moment, resulting in the small $m^*$ and large Fermi surface. This Kondo breakdown on the surface possibly explains the non-LK behavior through the dramatic change in $m^*$.

An alternative approach is based on non-Hermitian Landau level problem of impurity-induced in-gap states of narrow insulators [74, 75]. The electron scattering between different Landau levels can be described by the non-Hermitian quasiparticle Hamiltonian. This scattering process is important to realize the in-gap state, which is responsible for the QOs. Contrary to the gap-narrowing scenario, the amplitude of QOs remains finite even at the absolute zero temperature in this theory.

The importance of the strong correlation effect to the SS has also been studied [76]. The interplay between correlations and topology successfully explains both the dHvA and SdH effect, the amplitudes of which are enhanced on increasing the correlation strength.

### 2.4.2 Neutral quasiparticles as a source of QOs

The theories we have discussed so far do not require any actual bulk Fermi surfaces but demonstrate that some insulators still can exhibit QOs. A more straightforward idea, in some ways, is that a certain type of quasiparticles form bulk Fermi surfaces and can experience the Landau quantization in magnetic fields, resulting in the unconventional QOs. However, such quasiparticles cannot be conventional electrons because they are not directly responsible for the charge transport, given the activation behavior in the resistivity of KIs. In other words, they must be charge-neutral quasiparticles. Some theories are, in fact, based in this idea, and several types of charge-neutral quasiparticles have been proposed.

Knolle and Cooper [77] proposed that excitons, which are bound states of an electron and an hole, can be realized in $SmB_6$ and may be the source of the QOs. In this scenario, they showed that KIs are susceptible to the formation of excitons owing to the ring-shaped dispersion of the hybridized bands. In a certain range of parameters, the dispersion of the excitons can be considered gapless, which results in the QOs. Despite the charge neutrality of excitons, they are responsible for the thermal excitations, leading to the finite specific heat and thermal conductivity. Because of their bosonic nature, the calculated temperature dependence of specific heat and thermal conductivity show non-monotonic behavior, as shown in Fig. 2.6(a)-(b). While this theory can explain the dHvA effect and its non-LK temperature damping, it is not unclear how SdH effects can be described within this theoretical framework.

Chowdhury *et al.* [78] also developed a theory based on excitons. First, following the slave-boson representation $f = b\chi_{\rm s}$, the $f$-holes $f$ are fractionalized into spinless bosons $b$ (holons) with charge $-e$ and neutral fermions $\chi_{\rm s}$ (spinons) with spin $s$ (Fig. 2.7(a)-(b)). The conduction $d$-electrons $d$ then form binding states with holons $b$ in the form $\Psi = bd$ owing to the strong attractive interaction. Here, $\Psi$ represents the composite fermionic excitons that follow Fermi-Dirac statistics. As these composite excitons and spinons form neutral Fermi surfaces of hybridized bands, as shown in Fig. 2.7(c), the low-energy excitations become similar to that of ordinal metals, yielding $T$-linear terms in the specific heat $C \sim \gamma T$, thermal conductivity $\kappa \sim \kappa_0 T$, and NMR spin-lattice relaxation rate, $1/T_1 \sim T$. This theoretical view is similar to the spinon Fermi surface proposed in quantum spin liquids [79], although QOs have not been experimentally realized in this class of materials. QOs can also occur when these neutral fermions couple to external fields through the internal gauge degree of freedom in holons. This coupling is also expected to be manifested as a sizable finite thermal Hall conductivity $\kappa_{xy}$, as the neutral fermions experience the Lorentz force in fields.

Majorana fermions have also been proposed [80–82] as a source of the unconventional QOs. Historically, they were first introduced in the context of particle physics, and recently, they have been intensely debated as possible emergent quasiparticles in certain quantum materials such as the Kitaev model [83, 84]. It is interesting to note that the introduction of the Majorana operator in KI was first prompted by Coleman *et al.* [85] in 1993 before the discovery of TIs and the unconventional QOs in KIs. Majorana fermions are particles whose anti-particles are themselves ($\gamma = \gamma^\dagger$), and therefore, they are charge neutral. They can be described as fractionalized electrons and may form a neutral Fermi surface, as shown in Fig. 2.7(d). The QOs can be realized through the Landau quantization of original electrons. However, no experiments have provided direct evidence of Majorana fermions in KIs.

We have seen that several types of neutral quasiparticles have been proposed as possible candidates for the origin of the QOs. One way to test the presence of such neutral particles is to detect the neutral Fermi surface by measuring other physical quantities such as thermal conductivity. The response with respect to an applied magnetic field may also provide pivotal information that allows us to identify the microscopic origin of the excitations.

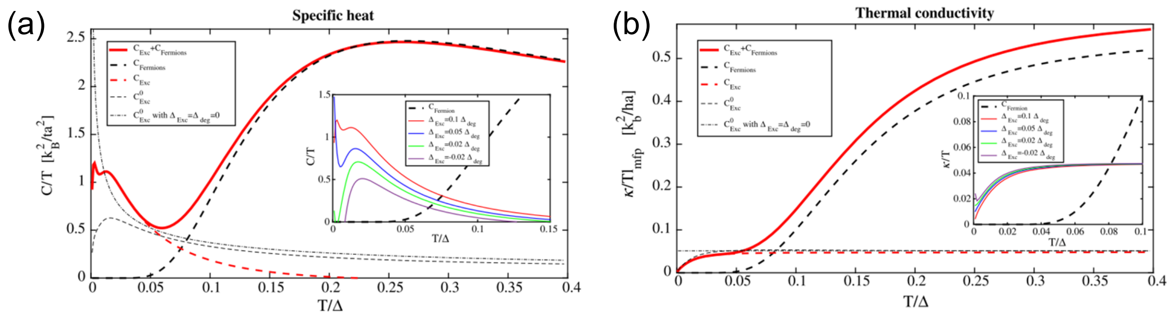


Figure 2.6: Calculated temperature dependence of the (a) specific heat and (b) thermal conductivity based on the exciton model [77].

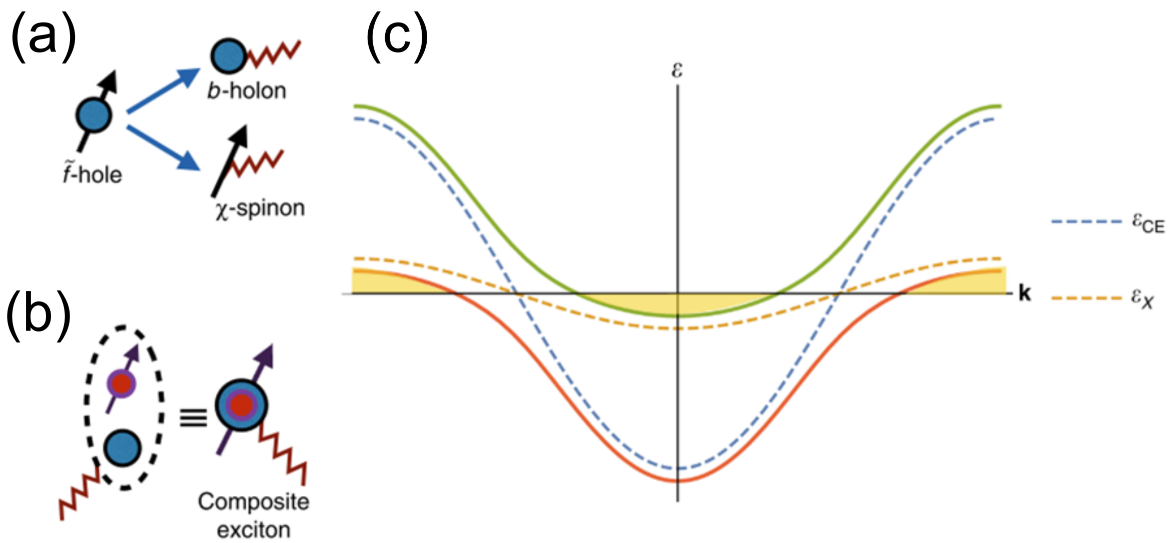


Figure 2.7: Proposed Fermi surfaces of neutral fermions of composite excitons [78]. (a) Schematic of the fractionalization of the $f$-hole. (b) Formation of the composite exciton between a conduction electron and holon. (c) Hybridized band of the neutral fermion of an exciton and a spinon.

# 3 Quantum oscillations in $YbB_{12}$

## 3.1 Introduction

The observation of unconventional QOs in $SmB_6$ stimulated substantial efforts to understand its nature, both theoretically and experimentally. The fundamental question is whether they are intrinsic properties commonly observable among (topological) KIs or a specific feature inherent in $SmB_6$. A comparison to other similar materials, thus, may provide important information to solve this problem. For the other TKI $YbB_{12}$, we investigated high-field electric properties such as the transport, magnetic torque, and penetration depth to discover possible QOs in both insulating and field-induced metallic phases by employing a series of experimental techniques [86, 87].

## 3.2 Sample characterization

High-quality single crystals of $YbB_{12}$ were grown and provided by Prof. Fumitoshi Iga at Ibaraki Univeristy, Japan. The crystals were synthesized using the traveling-solvent floating-zone method [50]. We conducted a series of measurements for three different samples, which are labeled #1, #2, and #3. #1 and #2 were cut off from the same growth batch, while #3 was taken from another batch. To estimate the sample quality, we performed synchrotron X-ray powder diffraction measurements at the BL02B2 beamline at the SPring-8 facility, Japan. Figs. 3.1(a)-(b) display the diffraction pattern. Fine peaks attributed to the crystalline structure of $YbB_{12}$ were clearly observed. As impurities, tiny amounts of $Al_2O_3$ and $YbB_6$ were found. $Al_2O_3$ contamination possibly occurred during the grinding process for making the powder from the bulk crystal, while $YbB_6$, which is a correlated insulator, is the only impurity phase we found in our sample. Peaks corresponding to other metallic $YbB_x$ compounds such as $YbB_2$ and $YbB_4$ could not be resolved with our experimental resolution, and the maximum volume can be estimated to be less than 10 ppm. These diffraction results indicate that the samples contain an extremely low concentration of metallic impurities. The magnetic susceptibilities of crystal #2 and #3 were measured using MPMS Quantum Design, and the resulting temperature dependence is shown in Fig. 3.1(c). We found excellent agreement with previously reported data [54]: $\chi$ shows a Curie-Weiss-like response at high temperature as well as a broad peak around 70 K, and it finally shows saturation at low temperature. However, there is a minor difference in that the absolute value below 10 K is slightly smaller than that in the previous report. This suggests the Kondo screening is a little stronger in the present sample, which may indicate a better sample quality.

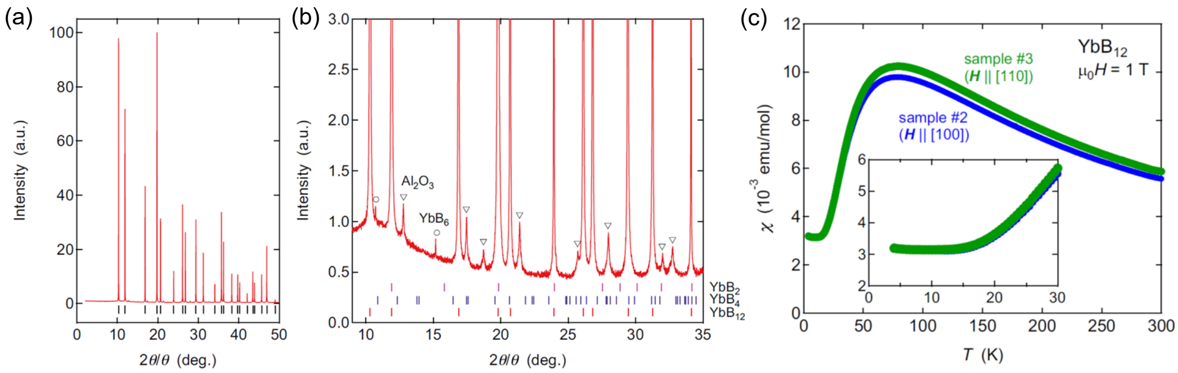


Figure 3.1: Sample characterizations. (a), (b) Synchrotron X-ray powder diffraction pattern of the $YbB_{12}$ samples. The bottom tick marks in (a) represent the peak positions of $YbB_{12}$, while the circles and triangles in (b) indicate the peaks of $YbB_6$ and $Al_2O_3$, respectively. (c) Temperature dependence of the susceptibility $\chi$ in #2 and #3. The inset shows an expanded view of the region below 30 K.

The higher sample quality also results in a slight variation in the gap amplitude $\Delta$ among the different growth batches. Fig. 3.2(a) displays the temperature evolution of the resistivity $\rho$ of all the three samples. At 0.1 K, $\rho$ is 4-5 orders of magnitude larger than that at room temperature. Although $\rho$ is not sample dependent around room temperature, it shows significant variation with decreasing. The resistivity plateau, which we also discussed in chapter 1, appears to be due to surface conduction as the residual resistivity is roughly proportional to the sample thickness. To evaluate $\Delta$, we make an Arrhenius plot, $\ln \rho$ vs. $1/T$, for all crystals. We found a two-gap behavior, which is consistent with a previous transport measurement [50]. The small gap developing below $\approx 20$ K shows a slight sample dependence, and the linear fittings over the temperature range of 6 K $< T <$ 12.5 K yields a gap of 4.7 meV for #1 and #2 and of 4.0 meV for #3. The present results suggest that the sample quality of the first batch (#1 and #2) is slightly higher than that of the second one (#3), as the large activation energy, in general, implies a low impurity concentration and high homogeneity. The larger gap developing in the temperature range of 20 K $< T <$ 300 K is approximately 11 meV, and this gap does not show significant sample dependence. We note that the larger gap is almost twice larger than that reported in another paper [88].

It is also worth noting that our transport data do not reveal any metallic behavior below the I-M transition critical field $\mu_0 H_{\text{I-M}} \sim 46$ T. Fig. 3.2(c) shows the temperature dependence of the resistivity with different magnetic fields of up to 45 T. Even at 45 T, $\rho$ shows an increasing trend with decreasing temperature, indicating that the activation behavior survives and the samples are purely insulating.

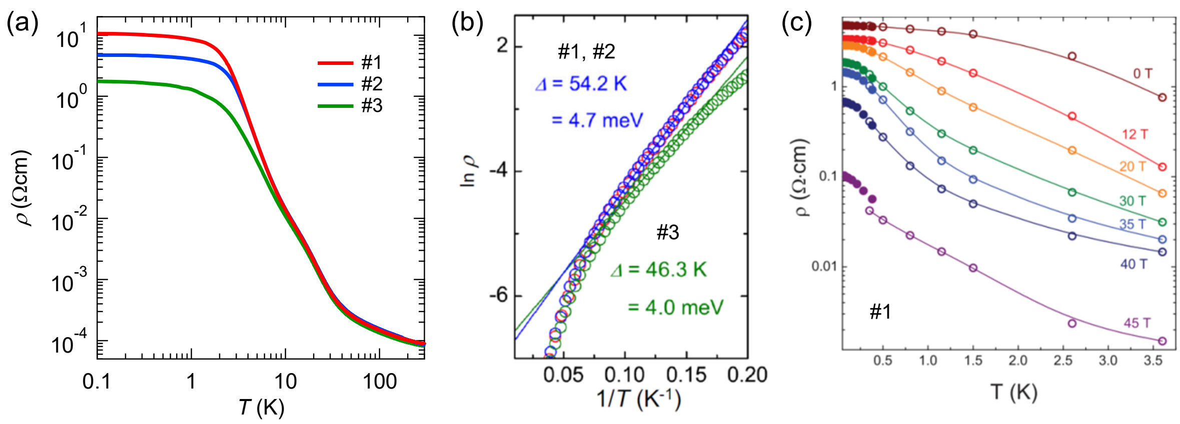


Figure 3.2: (a) Temperature dependence of resistivity in three samples. (b) Arrhenius plot above 5 K. The solid lines indicate the fitting results, and the activation energy $\Delta$ is extracted from their slopes. (c) Temperature dependence of resistivity in various fields taken using pulsed fields. The open and solid circles represent the data taken in a $^3$He cryostat at $\phi = 7.4°$ and in a dilution fridge at $\phi = 8.5°$, respectively. The solid lines are guides to the eye.

## 3.3 Results and discussion

### 3.3.1 QOs in the insulating phase of $YbB_{12}$

Fig. 3.3(a) shows the field dependence of the magnetic torque $\tau$ in #1 with different $\phi$ of up to 45 T. Here, $\phi$ denotes the angle of the magnetic-field direction from the [100] crystal axis. $\tau$ shows a step-like anomaly around 20 T, which is attributed to the meta-magnetic transition. More importantly, $\tau$ shows distinct oscillations around $\sim$ 38-45 T. It is remarkable that the dHvA effect occurs in the insulating phase of $YbB_{12}$, similar to $SmB_6$. The inset shows the FFT frequency of the dHvA oscillations in the field range of 38.5-45 T. The major peak of $F = 720$ T and its higher harmonics are clearly resolved by the calculation.

Next, high-field MR data in the three samples are given in Fig. 3.3(b). Remarkably, the samples show clear oscillations well below the critical field $H_{\text{I-M}}$, revealing that the SdH effect can be observed in the insulating phase of $YbB_{12}$, unlike $SmB_6$. The negative slope of the background MR, which is the hallmark of field-induced gap suppression, can be subtracted by polynomial fitting to produce the oscillatory component of the MR $\Delta\rho$, as shown in Fig. 3.3(c). Distinct oscillations were resolved especially in #1 and #2, but #3 does not show significant periodic modulations. The fact that #1 and #2 show peaks at the same intervals with respect to $1/H$ strongly indicates that the oscillation is indeed the SdH effect. Moreover, the SdH oscillations in #1 and #2 become visible under almost the same field, implying that the scattering rates in these two samples are almost identical. On the other hand, because #3 has a smaller $\Delta$ than #1 and #2, the scattering rate in #3 should be lower. The absence of the SdH effect in #3 is consistent with this view, but it also indicates that crystals with stronger insulating characters show more pronounced QOs, which is inconsistent with the conventional theory of QOs. The current observations imply that the QOs in the insulating phase are an inherent feature of $YbB_{12}$, as metallic impurities, if they existed, would have behaved in a manner opposite to the observations.

As discussed in section 2.4, it is important to check whether the quasiparticles forming

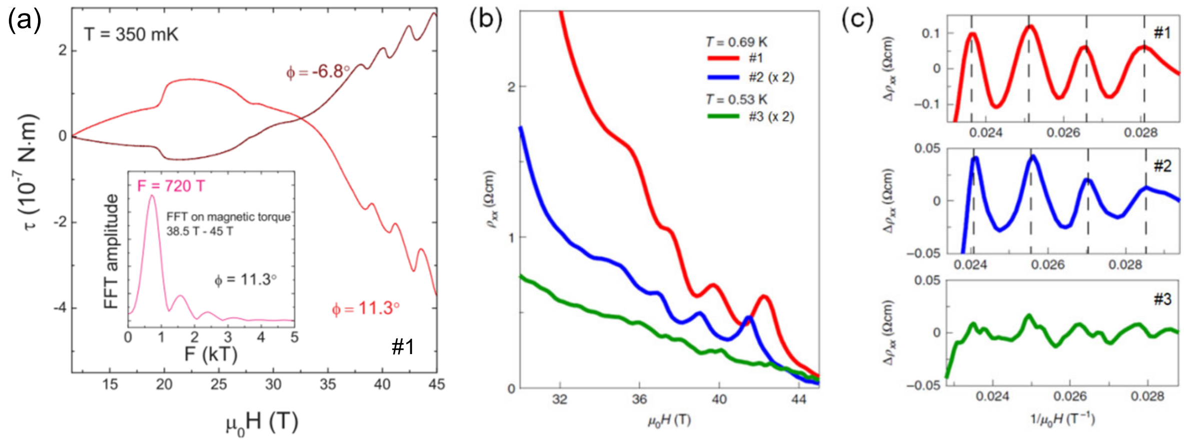


Figure 3.3: Quantum oscillations observed in the insulating phase of $YbB_{12}$. (a) dHvA effect proved by the magnetic torque. The inset shows the oscillation frequency calculated via FFT. (b) High-field magnetoresistance of three samples. #1 and #2 show distinct SdH oscillations around 36-44 T. (c) Oscillatory component of the magnetoresistance as plotted against $1/\mu_0 H$ for all samples, obtained from the data in (b).

the Fermi surface follow the Fermi-Dirac distribution law. The temperature dependence of the normalized oscillation amplitude for both the dHvA and SdH effects is displayed in Figs. 3.4(a)-(c). The solid curves are the fitting results obtained using the LK-formula (Eq. 2.13). We found excellent agreement with the LK curves for the data of both oscillations over the different ranges of fields and angles, implying that the quasiparticles are fermions. The fittings yield an effective mass ratio of $m^*/m_0 \sim 6.7$ from the dHvA effect and $\sim 15$ from the SdH effect. The different effective masses obtained from the dHvA and SdH effects may imply that they originate from different bands, although there remains the question why the band with the smaller mass detected from the dHvA effect does not contribute to the SdH signal. The observed effective mass is larger than that of a bare electron, which is contrary to the case of the small mass observed from the dHvA effect in $SmB_6$. This larger mass of the quasiparticles indicates that they result from the strong correlation in the Kondo lattice. The successful FFT calculation of the oscillations and the good agreement with the LK description confirm that the observed high-field features are QOs, rather than a series of field-induced Lifshitz transitions.

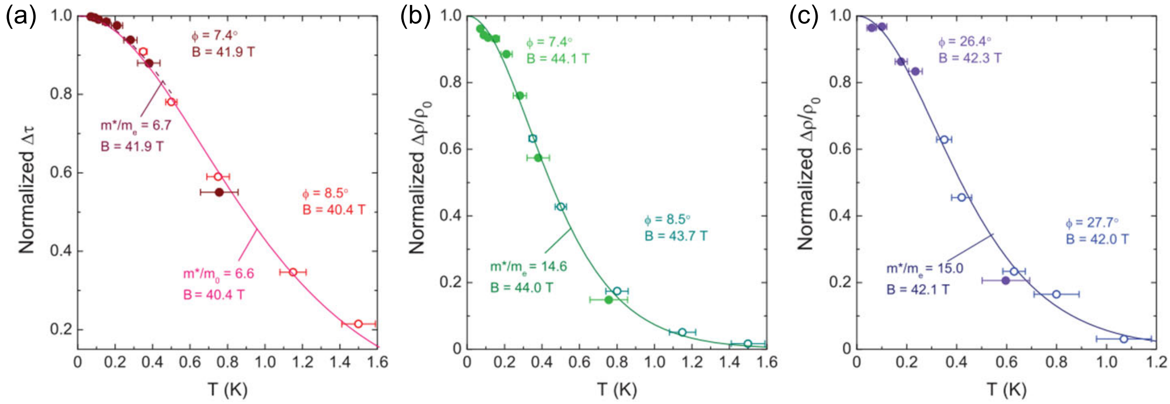


Figure 3.4: Temperature dependence of the normalized amplitude of (a) the dHvA effect and (b), (c) the SdH effect in the insulating phase of $YbB_{12}$. The solid curves in each panel and the dotted curve in (a) are LK fits. The corresponding effective mass is also given in each panel as a fitting parameter.

The angular dependence of $F$, which is calculated using FFT and Landau level fitting for each type of QOs, is displayed in Fig. 3.5(a). The open circles represent the data obtained from the dHvA effect, whereas the open triangles represent data extracted from the SdH oscillations. The angular dependences of $F$ obtained from the dHvA and SdH effects are quite different, indicating that they originate from different bands. The frequency of dHvA oscillations has a 2D-like nature: $F$ can be well fitted by the cylindrical Fermi surface model expressed as Eq. 2.16. However, the dHvA signal disappears when the field is applied at an angle above $\phi \sim 20°$. The relatively weak angle dependence within the small angle range of $|\phi| < 20°$ cannot rule out the possibility that the Fermi surface has a more prominent 3D nature. The frequency obtained using the SdH signal, on the other hand, shows a non-monotonic angle dependence. In the small angle range of $|\phi| < 20°$, the SdH frequency shows a stronger angle dependence than that expected from the 2D model. Furthermore, above $\sim 20°$, $F$ decreases with increasing $\phi$. The overall angular dependence can be explained by the 3D Fermi surface illustrated in Fig. 3.5(b) but not the 2D cylindrical model. The steep change in the small angle range can be traced by assuming a hyperboloid model, which is expressed as

$$F(\phi) \propto (\cos^2 \phi - r \sin^2 \phi)^{-1/2} \tag{3.1}$$

with the shape scaling parameter $r = a^2/c^2$ in the hyperboloid equation $(x^2+y^2)/a^2 - z^2/c^2 = 1$. The black dashed curve in Fig. 3.5(a) shows the fitting result with the parameter $r = 7.42$. This hyperbolic Fermi surface is typically found in the "neck" regime connecting large Fermi surfaces, as shown in Fig. 3.5(b). The frequency drop above $\phi \sim 20^\circ$ can also be explained within this model by assuming large oblate 3D spheroids. The magenta dash-dot curve in Fig. 3.5(a) is a rough description of the high-angle data with the aspect parameter $b/a = 0.101$. The corresponding minimum and maximum cross-section areas perpendicular to the [100] crystalline axis for the neck and oblate spheroid are $A = 7.62$ and $37.5\ \mathrm{nm}^{-2}$, respectively. These 3D features of the Fermi surface revealed by the SdH effect strongly suggest that the SdH signal arises from the insulating bulk, rather than the (topological) 2D surface state.

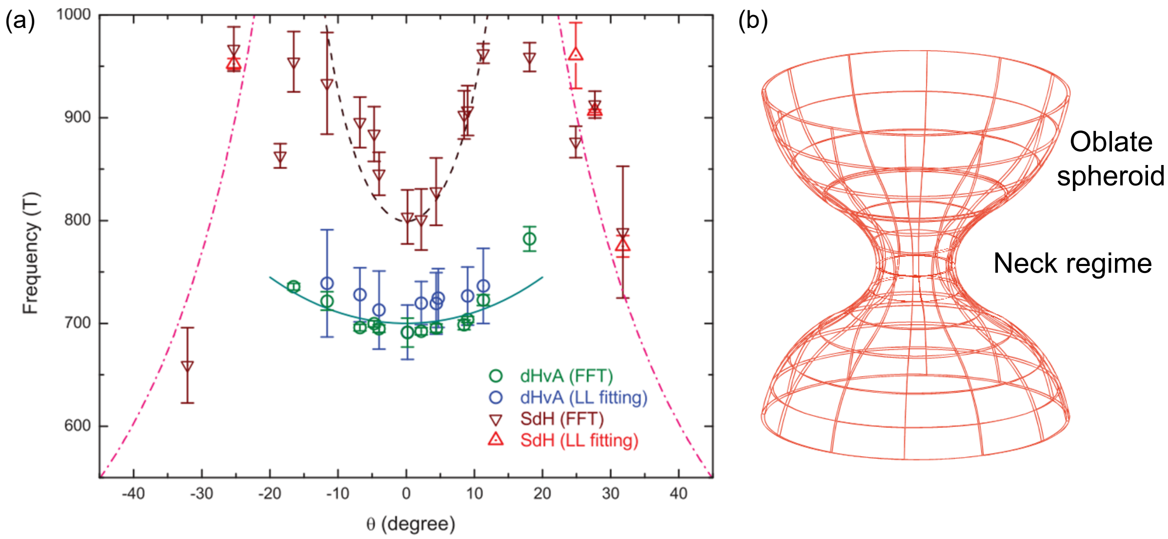


Figure 3.5: (a) Angular mapping of the QO frequency obtained from the dHvA effect (open circles) and SdH effect (open triangles). The points were obtained using either FFT or Landau level fitting. The green solid curve is a fit obtained using a 2D Fermi surface model (Eq. 2.16) with $F_0 = 700$ T. The black dashed curve represents the simulation of for the neck-shaped Fermi surface model, while the magenta dash-dot curve shows the calculation with the oblate spheroid model. (b) Schematic of the 3D Fermi surface, which is consistent with our observations.

### 3.3.2 High-field exotic metal of $YbB_{12}$

The observations of QOs in $YbB_{12}$ imply the existence of a Fermi surface with charge-neutral fermions. To understand the nature of the QOs, it is informative to study how the electronic structure evolves and enters the field-induced Kondo metal (KM) phase as the energy gap closes. Moreover, the electronic properties realized in the field-induced metallic state are not fully understood, because the experimental techniques we can utilize are limited owing to the large critical field. In this section, we present transport measurements by using the PDO technique in the KM phase to observe the SdH effect and discuss how the possible Fermi surface of the neutral fermions are affected by interactions with conventional charged fermions.

We employed the contactless proximity-detector-oscillator (PDO) technique, which allows one to measure the conductivity of a metallic sample through the skin depth in a pulsed magnetic field environment [89, 90]. The shift in the resonant frequency $f$ of the PDO circuit is given by

$$\Delta f = -a\Delta L - b\Delta R, \tag{3.2}$$

where $L$ and $R$ are the inductance and resistance of a sample coil and $a$ and $b$ are constants. The change in $L$ in the coil filled with the metallic sample is related to the change in the skin depth $\lambda$ by $\Delta L \propto (r - \lambda)\Delta\lambda$, where $r$ is the sample radius. The skin depth is also expressed by a combination of the resistivity $\rho$, angular frequency of the circuit $\omega$, and permeability of the sample $\mu$ as

$$\lambda = \sqrt{\frac{2\rho}{\omega\mu}}. \tag{3.3}$$

Therefore, the frequency shift $\Delta f$ is a measure of the MR of the sample. When the sample is insulating, the skin depth becomes as large as the sample radius, leading to the complete penetration of the field through the sample. In this case, the change in $\lambda$ in the sample cannot be detected through $\Delta f$. This implies that the PDO technique is applicable only to metallic samples. Therefore, in the KI state of $YbB_{12}$, $\Delta f$ is determined by the MR of the copper wire of the coil.

The field dependence of the PDO frequency $f$ is shown in Fig. 3.6(a) for various field directions $\theta$, which is the angle from [100] towards [110]. The I-M transition is manifested as the dip feature in $f$, as the sample skin depth shows a dramatic change across the critical field. On top of the positive MR on the KM phase, SdH oscillations are clearly detected, especially for small angles near $\theta \sim 0°$. Fig. 3.6(b) shows the oscillatory component of $f$, which was obtained by polynomial background subtraction, as a function of $1/H$. The steep change in the oscillation pattern above $\theta \sim 20°$ is reminiscent of the previous observations of a dramatic change in the QOs in the KI phase at this angle (the dHvA effect disappears, and the SdH frequency starts to show a negative angular dependence). This similarity across the I-M transition implies that the QOs in both the insulating and metallic phase are determined by the same band. We discuss this point in more detail later.

The frequency pattern observed in the KM phase shows unusual behavior. Fig. 3.6(c) shows the Landau level plots for the SdH oscillations in both the KM and KI states. The symbols in the KM phase are determined by the peaks and valleys, as labeled in Fig. 3.6(b). Here, the + and − signs represent the spin-split Landau sublevels. Thus, the average of these characteristic fields corresponds to the oscillations from the spin-degenerate Fermi surface. The Landau index $N$ in the KI phase shows the usual behavior of varying in proportion to $1/H$, and the slope corresponds to the field-independent quantum oscillatory frequency. On the other hand, it is remarkable that the Landau index in the KM phase does not show such behavior, implying that the SdH oscillations in KM are not periodic in $1/H$. This non-periodicity indeed leads to the failure of the FFT calculation for $\Delta f$: the summation of the calculated frequency components cannot reproduce the features in the raw data.

Nevertheless, despite the unusual periodicity, the temperature dependence of the SdH amplitude in the KM state can be well captured by the LK formulation (Eq. 2.13) as shown by the solid curves in Fig. 3.6(d). The inset shows the field dependence of the cyclotron energy $E_{\mathrm{c}} = eB/m^*$ obtained with each LK fit in the main panel. The $H$-dependence of $E_{\mathrm{c}}$ and the non-periodic SdH oscillations imply that the topology of the Fermi surface in the KM phase is $H$-dependent.

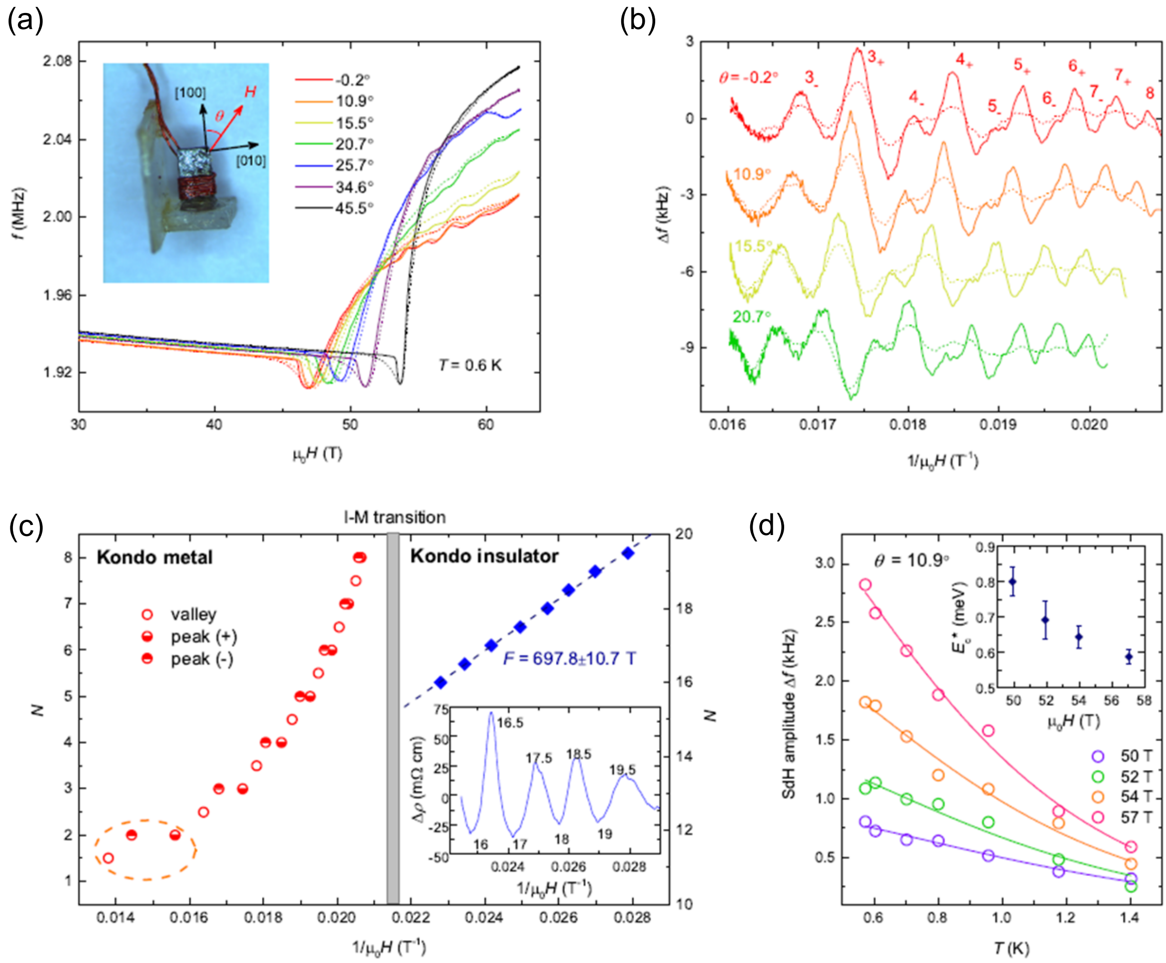


Figure 3.6: (a) PDO frequency as a function of the field with various field directions. The inset shows an image of a sample wrapped by a PDO coil and defines the configuration of the angle $\theta$. (b) Oscillatory component of the SdH signals in (a). The integers are the Landau indices. The solid and dashed curves in (a) and (b) represent the data acquired from upsweeps and downsweeps, respectively. (c) Landau level plots for the KM and KI phases. The inset displays the SdH effect in the KI state. The data marked by the dashed orange circle is obtained using a 75 T Duplex magnet. (d) Temperature dependence of the SdH amplitude for various fields. The inset shows the field dependence of the cyclotron energy determined from the fitting results in the main panel.

To analyze the non-periodic SdH oscillations in the KM state, we introduce an empirical relationship between the Landau index $N$ and the characteristic magnetic field $H_N$ at which the peaks or valleys are observed:

$$N + \lambda = \frac{F_0}{\mu_0(H_N - H^*)}, \tag{3.4}$$

where $\mu_0 H^*$ is an offset field and $\lambda$ is a phase factor. Setting $\mu_0 H^* = 41.6$ T, Eq. 3.4 successfully explains the relation between the characteristic $H_N$ and Landau index $N$ in the whole angle range below $\theta \sim 20°$, as shown in Fig. 3.7(a). Owing to the offset term, Eq. 3.4 implies that the QO frequency is field dependent. By setting $B \approx \mu_0 H$ and $B^* \approx \mu_0 H^*$, we introduce the $B$-dependent frequency as follows:

$$F_{\mathrm{KM}} = \frac{F_0}{B - B^*} B. \tag{3.5}$$

As discussed in subsection 2.2, Onsager's rule still holds even if the cross-section area of the Fermi surface is $B$-dependent, i. e., $F(B) = A(B)\hbar/(2\pi e)$. Therefore, one can interpret the $B$-dependent frequency as a cross-section area that progressively depopulates as $A(B) = A_0 B/(B - B^*)B$, where $A_0 = 2\pi e F_0/\hbar$.

From the above perspective, our results indicate that the Fermi pockets in the KI and KM states, which are attributed to the QOs in those states, are identical or at least closely related. The field dependence of the frequency $F_{\mathrm{KM}}$ in the KM state for $H \,||\, [100]$ is shown in Fig. 3.7(b). A cursory inspection reveals that $F_{\mathrm{KM}}$ is quite close to the $B$-independent frequency in the KI state when $F_{\mathrm{KM}}$ is extrapolated back to $H_{\text{I-M}}$. This coincidence of the frequency around the critical field $B = \mu_0 H_{\mathrm{KM}}(\theta)$ holds for all $\theta$ at which the SdH effect was observed. The magenta points in the inset of Fig. 3.7(b) shows the field dependence of the frequency, which is extrapolated from the KM state to the critical field. $F_{\mathrm{KM}}(\mu_0 H_{\text{ I-M}})$ closely traces that in the KI state, albeit with an offset of $\sim 100$ T. This offset might originate from the discontinuous jump of the cross-section area at the phase boundary or from the potential uncertainty of the critical field associated with a valence change [91]. Indeed, a slight offset to the critical field

$\mu_0 H_{\text{I-M}} - 0.8$ T is sufficient for the extrapolated frequency to trace well the angular dependence in the KI state (the red points in the inset of Fid.3.7(b)).

QOs also provide information on the cyclotron mass $m^*$ of the quasiparticles. The comparison of $m^*$ between the KI and KM states gives further supporting evidence that the Fermi surface attributed to the QOs are closely related in both phases. Fig. 3.7(c) shows the field dependence of the cyclotron mass ratio in both the KI and KM states. Around the critical field, the $m^*$ values for both phases coincide at $\sim 7$, which implies that the identical Fermi pocket is the source of the QOs in both states. As discussed previously, $m^*$ increases with increasing $H$ in the KM state. This mass enhancement is also captured by the spin-splitting parameter $S$ induced by the Zeeman splitting of the Fermi surface. According to [92], the split spin-down (-up) Landau level reaches the Fermi level under the following condition:

$$\frac{F}{B_N^{\pm}} = N + \lambda \pm \frac{1}{2}S. \tag{3.6}$$

Here, $S$ is determined from the $g$-factor and cyclotron mass as

$$S = \frac{1}{2}\frac{m^*}{m}g. \tag{3.7}$$

Thus, by tracing the additional phase factor in QOs owing to the Zeeman splitting, one can estimate $S$ from the nonlinear (Fig. 3.6(c)) and linear (Fig. 3.7(a)) Landau level plots as $S = F_m(1/B_N^+ - 1/B_N^-)$ and $S = F_0(1/(B_N^+ - B^*) - 1/(B_N^- - B^*))$, respectively. Fig. 3.7(d) depicts the field dependence of $S$ calculated using both the formulas. $S$ and $m^*$ are related to Eq. 3.7 and follow the same field dependence on substituting $g = 0.084$ (the red points in Fig. 3.7(d)). The coincidence of the field dependence not only validates the Zeeman splitting analysis, but also reveals the exotic property of the KM state, which hosts an unusually small $g$-factor compared to a non-interacting electron system ($g = 2$).

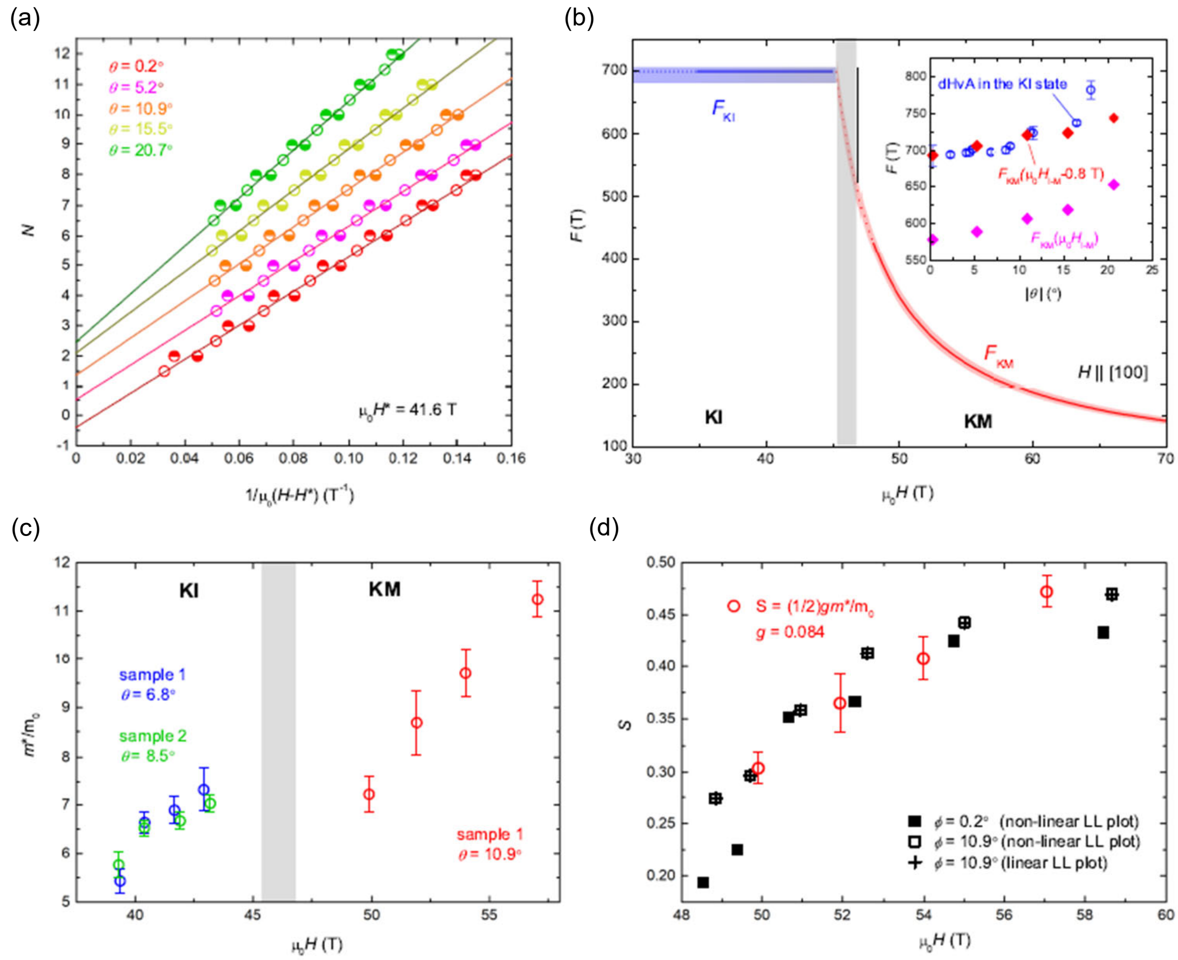


Figure 3.7: (a) Landau level plots as a function of $1/\mu_0(H - H^*)$. The offset field $\mu_0 H^* = 41.6$ T is determined so that the plot becomes linear. The slope for each line represents $F_0$ in Eq. 3.5. (b) Field dependence of the QO frequency $F$. $F$ is constant in the KI state but becomes $B$-dependent in the KM state, as described by Eq. 3.5. The solid and dashed lines represent the field range where the SdH oscillations are present and absent, respectively. The colored regime along each curve represents the width of the FFT peak. The black line around the phase boundary denotes the maximum allowed mismatch between $F_{\mathrm{KI}}$ and $F_{\mathrm{KM}}$ of $\sim 180$ T. The inset shows the field dependence of $F$. (c) Field dependence of the cyclotron mass ratio $m^*/m$. (d) Field dependence of the spin-splitting parameter $S$. The red points are estimated from the cyclotron mass in the KM state with $g = 0.084$.

The exotic properties of KM are also revealed by magnetotransport experiments. To measure the resistivity in the KM state reliably, the pulsed-current technique was employed. As the excitation current produces Joule heating in the KI state, in which the resistivity is relatively large, the current was applied only in the KM state. The time profiles of the current and magnetic fields are shown in the inset of Fig. 3.8(a). A current pulse was applied so that one can measure transport only when $H > H_{\mathrm{I-M}}$. Figs. 3.8(a)-(b) show the temperature dependence of the observed resistivity $\rho(T)$ at 55 T, which is obtained by performing the pulsed-current measurement at various temperatures. Although the hybridization gap is completely suppressed in the KM state, the $\rho(T)$ curve shows typical behavior for Kondo lattice systems: $\rho(T)$ shows a peak at a coherent temperature $T^* = 14$ K and decreases as $T$ decreases, reflecting the formation of coherent heavy quasiparticle band. A remarkable feature found in the KM state is that it shows a temperature-linear resistivity, i.e., $\rho \propto T$, below $T^*$, which is the hallmark of non-FL behavior [8]. This anomalous behavior, however, only holds within the temperature range of $T_{\mathrm{FL}} < T < 9$ K, where $T_{\mathrm{FL}} = 2.2$ K is the temperature below which FL behavior is observed ($\rho \propto T^2$). Fig. 3.8(b) shows the $T^2$ dependence of $\rho$ below $T^2 = 10$ K. We found good agreement between the data and Eq. 1.10, and $\rho_0$ = 0.34 m$\Omega$cm and $A_2 = 58$ $\mu\Omega$cm were obtained by fitting, as indicated by the dotted line in Fig. 3.8(b). As the residual resistivity $\rho_0$, in general, originates from impurity scattering, this relatively large $\rho_0$ indicates that the KM state may be classified as a "bad metal."

The Fermi surface attributed to the QOs does not contribute to the charge transport in KM for the following reason. Our observations of the $B$-dependent QO frequency and cyclotron mass imply that the geometry of the Fermi surface in the KM state significantly changes and most likely shrinks by $\simeq 45$ % from 50 T to 60 T, according to Eq. 3.5 and $B$-dependent Onsager's rule. Assuming a spherical Fermi surface, this shrinkage corresponds to a $\simeq 60$ % reduction in the quasiparticle density $n$, whereas the observed cyclotron mass increases by $\simeq 60$ %. Consequently, the Drude expression $\rho = m^*/ne\tau$ predicts that the resistivity would increase by a factor of 4 from 50 T to 60 T. In contrast, the observed MR in the KM state is negligibly small, indicating that the Fermi surface revealed by the SdH effect is charge-neutral even in the KM state. To account for the charge-transport properties in the KM state, one might have to assume another Fermi pocket with conventional charged fermions. This hidden Fermi pocket is also necessary to explain the large Sommerfeld coefficient observed in the pulsed-field specific heat measurement [62], which yields $\gamma \sim 63$ mJ/molK$^2$ on interpolating the value at 55 T. First, we estimate the contribution to $\gamma$ from the Fermi surface detected by the SdH effect in the KM state as follows. Assuming the simplest case of a single 3D band of the isotropic FL, the Sommerfeld coefficient is given by

$$\gamma = \frac{\pi^2 k_{\mathrm{B}}^2}{3} \frac{m^* k_{\mathrm{F}}}{\pi^2 \hbar^2}, \tag{3.8}$$

where $k_{\mathrm{F}}$ is the Fermi vector. Inserting $m^*$ and $k_{\mathrm{F}}$, which are estimated from the SdH analysis, we find that $\gamma$ from this Fermi pocket makes a contribution of only 4.4% of the measured $\gamma$. This rough estimation indicates that the $\gamma$ is determined not only by the Fermi pocket we resolved from the SdH effect, but also by the other Fermi surface of conventional charged fermions that we miss in the QOs.

The implication of the hidden Fermi surface in the KM state can be also captured by the unusually large Kadowaki-Woods (KW) ratio. By combining $\gamma \sim 63$ mJ/molK$^2$ from the pulsed-field specific heat measurement [62] and $A_2 = 58$ $\mu\Omega$cm from the previous linear fitting of $\rho(T)$ below $T_{\mathrm{FL}}$ (Fig. 3.8(b)), we estimate the KW ratio in the KM state of $\mathrm{YbB_{12}}$ at 55 T as $1.46\times10^{-2}\mu\Omega\mathrm{cm(Kmol/mJ)}^2$, which is 3-4 orders of magnitude larger than the universal value given in Eq. 1.11. In Fig. 3.8(c), we represent the relation between $A_2$ and $\gamma^2$ in the KM state of $\mathrm{YbB_{12}}$ along with those of other classes of materials including transition metals, Ce- and U-based heavy fermions, Yb-compounds, and $d$-electron oxides. This strong deviation in the KM state verifies the exotic properties of KM, and one can estimate information on the hidden Fermi surface ($k_{\mathrm{F}}$ and $m^*$) by combining the unusually large $A_2$ and $\gamma$. Employing the same calculations as in [93], $A_2$ can be written as

$$A_2 = \frac{81\pi^3 k_{\mathrm{B}}^2}{4e^2\hbar^3} \frac{m^{*2}}{k_{\mathrm{F}}^5}. \tag{3.9}$$

Combining Eqs. 3.8 and 3.9, one can estimate $k_{\mathrm{F}} = 2.15\ \mathrm{nm}^{-1}$ and $m^* = 90.0m_0$. Although such a large effective mass is unusual in Yb-based compounds, it can explain why the charged fermions cannot contribute to the QOs in the current environment of the pulsed-field measurements.

Our results imply the coexistence of two fluids in KM state: (i) charge-neutral fermions (CNFs) and (ii) the more conventional but still exotic charged fermions. The CNFs contribute to the QOs in both the KI and KM states, but are not responsible for charge transport. The existence of the CNFs even in the KM state is supported by the similarity of the Fermi surface at $H_{\text{I-M}}$ and little contribution to MR, although the geometry of the Fermi pocket shows significant shrinkage and mass enhancement with increasing field. The emergence of the charged fermions above $H_{\text{I-M}}$ is supported by the unusually large $\gamma$ observed in the specific heat measurement and the FL behavior with the large coefficient $A_2$, which strongly violates the KW ratio. Based on the two-fluid picture, the I-M transition produces a sudden increase of the density in (ii), which becomes a dense liquid of heavy fermions in the KM state from a thermally excited low-density gas in the KI state. On further increasing $B$ in the KM state, (i) becomes less energetically favorable, and the Fermi surface of CNFs shrinks, as described by Eq. 3.5. The hidden Fermi surface of (ii) acts as a "reservoir" into which CNFs can scatter or transfer. The analogous situation of the two-fluid picture has also been reported in other materials [94, 95].

The exotic metallic state found in the high-field regime involves the survival of the CNFs above the gap closure and their coexistence with the charged FL. This peculiar two-fluid picture may explain the observed non-FL behavior. In this situation, Luttinger's theorem may be violated, leading to possible continuous variation of FL properties [96]. In addition, the $T$-linear resistivity may be attributed to the interaction between CNFs and charged fermions [97]. The exotic properties of the KM state we found, therefore, are a prerequisite for future theoretical works.

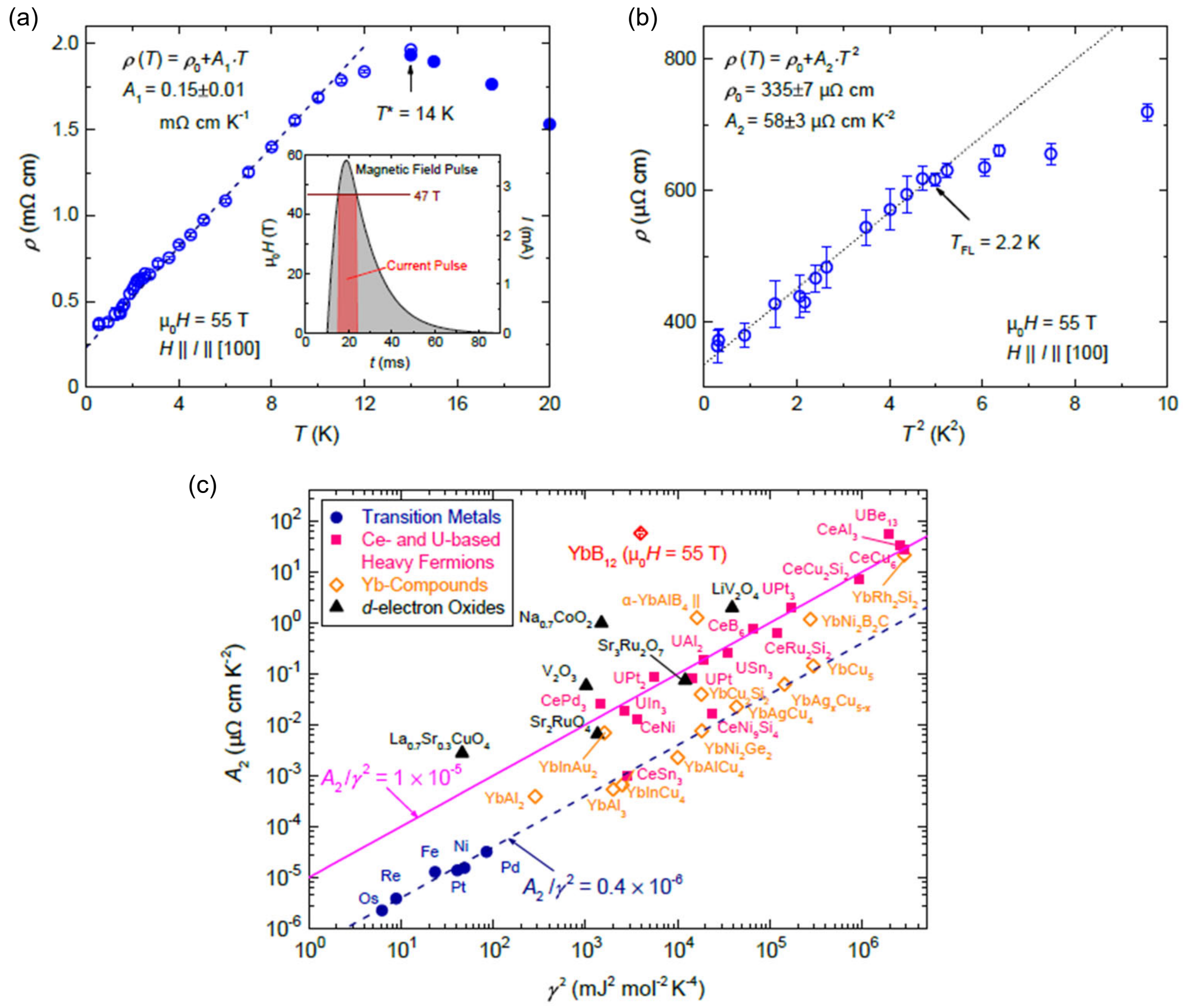


Figure 3.8: (a) Temperature dependence of resistivity of the KM state of $YbB_{12}$ at 55 T. The dashed line is the fitting for the $T$-linear resistivity regime. The inset shows the time profile of the pulsed magnetic field and current pulse. (b) Resistivity plotted against $T^2$. The dashed line is the fitting below $T_{\mathrm{FL}}$, and the parameters are also shown. (c) Kadowaki-Woods plot for a wide variety of materials, including transition metals (indigo circles), Ce- and U-based heavy fermions (magenta squares), Yb-based compounds (orange diamonds), and $d$-electron oxides (black triangles). The KM state of $YbB_{12}$ is plotted as a red diamond.

## 3.4 Conclusion

We investigated the high-field electronic properties of high-quality single crystals of the KI $YbB_{12}$ and successfully observed QOs both in the KI state and KM state. Remarkably, $YbB_{12}$ exhibits both the dHvA effect and SdH effect in the insulating phase well below the I-M transition field, suggesting that the QOs are an intrinsic property of the insulating ground state. Indeed, the amplitude of the SdH signals increases as the activation gap increases, ruling out the possibility that a metallic impurity phase contributes to the QOs. Furthermore, the temperature damping factor shows good agreement with the LK formula for a relatively large effective mass $m^* \sim$ 6-15$m_0$, demonstrating that the quasiparticles contributing to the QOs follow the Fermi-Dirac distribution law. The large observed $m^*$ also indicates that the electron correlation plays an important role in realizing the quasiparticles. Although the angular mapping of the frequency obtained from the dHvA effect cannot rule out the possibility of a 2D SS, the angle-resolved SdH signals strongly suggest that the Fermi surface has a 3D-like nature. Our observations provide intriguing evidence that the KI $YbB_{12}$ hosts a Fermi surface, which is a defining characteristic of metals. This apparent contradiction leads to the exotic Fermi surface of neutral fermions, which is also supported by the thermal transport experiment that we discuss in chapter 5. The observation of QOs in the insulating phase of $YbB_{12}$ makes a distant allusion to the fact that the QOs may be a common feature among KIs, but further investigations on $SmB_6$ and exploration on other types of KIs are required to confirm the universality.

We also resolved SdH signals above the critical field by employing the PDO technique and captured the exotic properties of the field-induced metallic state. Although the SdH effect in the KM state shows a non-linear Landau level plot, our analysis reveals a similarity between the Fermi surfaces in the KI state and KM state. We concluded that the Fermi pocket contributing to the QOs in the KM state is identical to that in the KI state. Our observation can be, therefore, interpreted in terms of a two-fluid picture: the coexistence of (i) CNFs, which contribute to the QOs in both the KI and KM states, and (ii) the more conventional but still exotic heavy FL. Although the CNFs are not strongly affected at the I-M transition, they become energetically unfavorable and convert into (ii) as the field increases. The field evolution of the Fermi surface of (i) is indeed captured by the unusual field suppression of $F_{\mathrm{KM}}$ and enhancement of $m^*$. Although the Fermi surface of (i) can be resolved by the current environment of pulsed-field measurements, it is not the case for (ii) owing to the surprisingly large $m^* \approx 90m_0$. Despite the absence of QOs from (ii), this hidden Fermi surface contributes to the large $\gamma$ and extremely massive $A_2$, which strongly violates the universal Kadowaki-Woods ratio. In addition, analysis on the spin-splitting QOs enabled us to evaluate the extremely small $g \sim 0.084$ of the neutral fermions. The coexistence of the two fluids and their interaction may explain the non-FL behavior found in the KM state. Our observations provide strong constraints for future theoretical investigations to explain the origin of CNFs and exotic metallic properties.

# 4 Purpose of this study

KIs have attracted renewed interest owing to the introduction of the concept of topology. Moreover, a series of recent detailed experiments have revealed another aspect of exotic properties in this strongly correlated insulator: unconventional QOs. The QOs observed in $SmB_6$ and $YbB_{12}$ sparked an intensive debate, but their origin remains unclear. If they host a Fermi surface with CNFs, as some theories proposed, their zero-energy excitations might contribute to the heat transport, resulting in a linear temperature dependence of the specific heat and thermal conductivity. Furthermore, if these neutral fermions are responsible for the QOs at higher fields, the possible Landau quantization of neutral fermions might contribute to the finite thermal Hall signal in analogy with conventional electrons. Motivated by these speculations, we studied the low-energy excitations in the KI $YbB_{12}$. In the next chapter, we will present the results of specific heat and thermal-transport measurements down to the dilution temperature at various fields to discover gapless fermionic excitations.

# 5 Charge-neutral fermions in $YbB_{12}$

## 5.1 Introduction

We have discussed the unconventional QOs in TKIs, the origin of which remains puzzling. As these observations generally indicate the presence of a Fermi surface, it is interesting to see if another experimental technique can resolve it. In FLs, the presence of a Fermi surface leads to gapless fermionic excitations, which are also manifested by the linear temperature dependence of the specific heat $C$ and thermal conductivity $\kappa_{xx}$. While the finite $\gamma = C/T(T \to 0)$ results from both localized and itinerant excitations, a finite residual thermal conductivity $\kappa_{xx}^0/T = \kappa_{xx}/T(T \to 0)$ is exclusively derived from itinerant excitations [98]. As thermal conductivity is free from local excitations such as the Schottky anomaly, it can provide the most direct and compelling evidence to determine whether the fermionic excitations have an itinerant character.

It has been reported that $SmB_6$ shows a finite $\gamma$ [71, 99–101]. Fig. 5.1(a) shows the temperature dependence of $C/T$ for a series of single crystals of $SmB_6$ [71]. $C/T$ shows a strong sample dependence, and the magnetic doping dramatically enhances the low-$T$ upturn. Although it was reported that the latest and cleanest sample grown using the floating-zone method shows a finite $\gamma \approx 4$ mJ/molK$^2$, there is ongoing debate on whether finite $\gamma$ is intrinsic to the insulating bulk, intrinsic to the in-gap state, or an extrinsic impurity contribution. The thermal conductivity of $SmB_6$ was also reported by several groups [101–103], and these results are shown in Figs. 5.1(b)-(d). Although $\kappa_{xx}^0/T$ was reported to be close to zero in these references, they show discrepancies in the $\kappa_{xx}$ in magnetic fields shows. While reference [102] reports a field-independent thermal conductivity, a significant magneto-thermal conductivity is reported in reference [103], which is interpreted in terms of conventional phonon scattering contributions. We also measured the low-temperature thermal conductivity of $SmB_6$ synthesized using the floating-zone method, as shown in Fig. 5.1(e). Our data at 0 T and 12 T do not show a significant field dependence, and in both sets of data, $\kappa_{xx}/T$ becomes vanishingly small on approaching zero temperature. These results indicate the absence of itinerant neutral fermionic excitations in $SmB_6$. Although inelastic neutron scattering experiments reveal distinct excitation modes within the hybridization gap [104], it is not evident whether the excitations are charge-neutral. Thus, the presence of intrinsic non-trivial itinerant quasiparticles within the gap in $SmB_6$ remains a controversial issue.

In the remainder of this chapter, we present measurements of the thermal transport properties of another candidate TKI, $YbB_{12}$, to investigate the low-energy excitations [105]. Although $SmB_6$ and $YbB_{12}$ show quite similar electronic properties, including the unconventional QOs, there seem to be several salient differences, such as in the presence of the SdH effect and the effective mass $m^*$ determined by the QOs. Therefore, systematic studies covering a wide range of materials may be key to understanding the nature of the exotic physics found in TKIs.

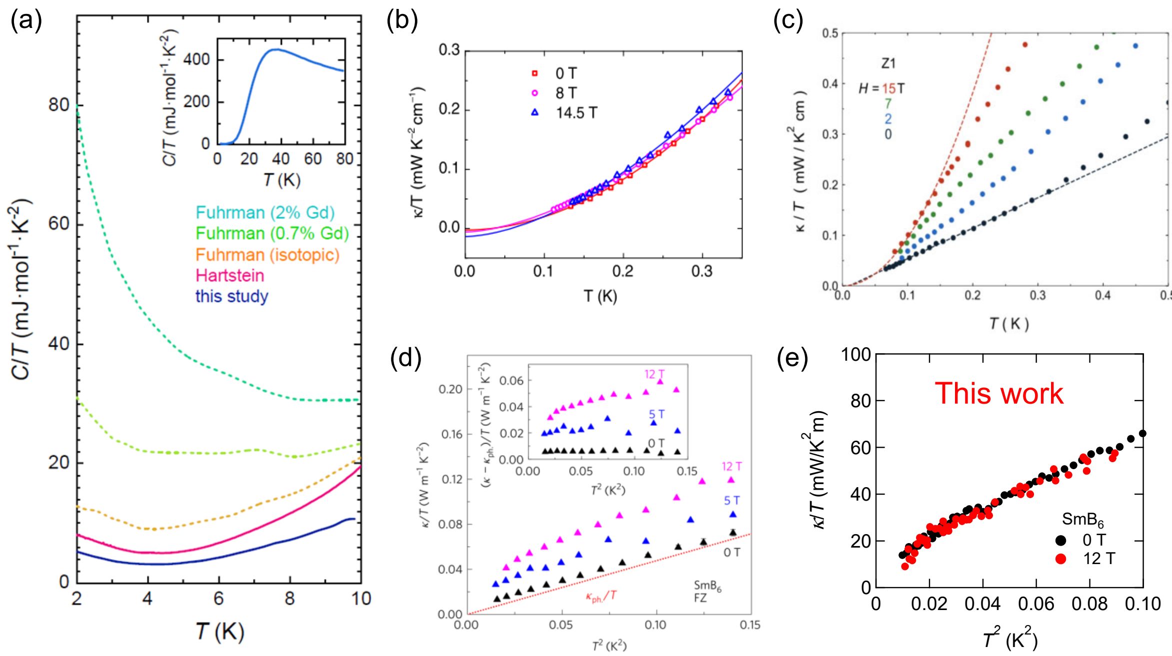


Figure 5.1: (a) Low-temperature specific heat in a series of single crystals of $SmB_6$ [71]. (b)-(d) Temperature dependence of thermal conductivity in $SmB_6$ with various fields. (b)-(d) are adopted from [102], [103], and [101], respectively. (d) Thermal conductivity of $SmB_6$ obtained in this work.

## 5.2 Experimental

### 5.2.1 Specific heat

Specific heat is one of the most fundamental physical properties of matter, as it is a bulk thermodynamic quantity related to the free energy of a given system. As the measurement of specific heat provides pivotal information on the electronic structure of a many-body system, it has been employed as a powerful tool for studying magnetism, superconductors, correlated insulators, and so on. The specific heat $C$ is defined as the ratio of the change in the heat absorbed by the system $\delta Q$ to the change in temperature $\delta T$

$$C = T\left(\frac{\partial S}{\partial T}\right)_p = \lim_{\delta T \to 0} \frac{\delta Q}{\delta T}. \tag{5.1}$$

A variety of experimental techniques have been developed to measure specific heat, such as adiabatic calorimetry, the continuous heating method, and AC calorimetry. In this study, we developed a setup based on the long-relaxation method, which has an overwhelming advantage in the measurement of tiny single crystals of mass is the order of a few micrograms [106, 107].

The principle of the long-relaxation method is as follows. A schematic of the measurement is shown in Fig. 5.2(a). The sample is mounted on a bare thermometer, which can also be used as a heater by applying excitation currents, producing Joule heat with power $P(T)$. The thermometer is weakly connected to a heat bath through a connection with a small thermal conductivity of $\kappa(T)$. In the long-relaxation method, a relatively large amount of heat is injected into the sample, and the time evolution of the sample temperature is recorded. Because of the large heat injection, the change in $C$ and $\kappa$ with respect to $T$ cannot be negligible. Taking the derivative of Eq. 5.1 with respect to time, we obtain

$$\frac{dQ}{dt} = C(T)\frac{dT}{dt}, \tag{5.2}$$

which can be expressed in the thermal equilibrium equation as

$$P(T) - \int_{T_0}^{T} \kappa(T')dT' = C(T)\frac{dT}{dt}. \tag{5.3}$$

In this method, we control $P(T)$ in the manner shown in Fig. 5.1(b): a higher power $P_{\mathrm{High}}(t)$ and a lower power $P_{\mathrm{Low}}(t)$ are fed into the sample within a constant time interval $\Delta t$. The temperature evolution with respect to time with the injection of a higher and lower power are then expressed as $T_{\mathrm{High}}(t)$ and $T_{\mathrm{Low}}(t)$, respectively. According to Eq. 5.3, these two relaxation processes can be written as

$$C(T)\frac{dT_{\mathrm{High}}}{dt} = P_{\mathrm{High}}(T) - \int_{T_0}^{T} \kappa(T')dT' \tag{5.4}$$

$$C(T)\frac{dT_{\mathrm{Low}}}{dt} = P_{\mathrm{Low}}(T) - \int_{T_0}^{T} \kappa(T')dT'. \tag{5.5}$$

This pair of equations can then be combined to obtain

$$C(T) = \frac{P_{\mathrm{High}}(T) - P_{\mathrm{Low}}(T)}{[dT_{\mathrm{High}}/dt - dT_{\mathrm{Low}}/dt]_T}. \tag{5.6}$$

Thus, by monitoring the time evolution of the relaxation curves with two different powers, the specific heat can be calculated using the above formula. The advantage of this technique is that we need not know $\kappa(T)$ accurately, because it will be canceled out as long as the base temperature $T_0$ is not influenced by the heat power. Another merit is that we can collect a set of data on $C(T)$ during just a pair of relaxation curves in a temperature range of $T_0 < T < T_{\mathrm{max}}$.

In DC measurements, the voltage induced by the thermoelectric effect cannot be negligible. This voltage can be canceled out by repeating the set of relaxations with positive and negative currents. One sequence for the measurement, therefore, consists of four sets of currents, $+I_{\mathrm{High}}$, $+I_{\mathrm{Low}}$, $-I_{\mathrm{High}}$, and $-I_{\mathrm{Low}}$, and the reading of the corresponding voltages, $V_{+\mathrm{High}}$, $V_{+\mathrm{Low}}$, $V_{-\mathrm{High}}$, and $V_{-\mathrm{Low}}$. The thermoelectric voltage can then be canceled as

$$V_{\mathrm{High}} = \frac{V_{+\mathrm{High}} + V_{-\mathrm{High}}}{2} \tag{5.7}$$

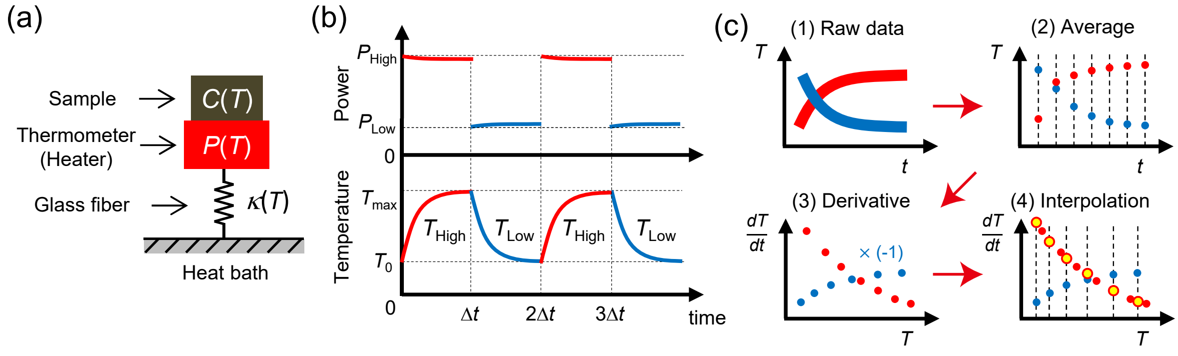


Figure 5.2: (a) Schematic of the setup for specific heat measurement using the long-relaxation method. (b) Time evolution of the temperature response to applied power. (c) Illustrations of the procedure of data analysis.

$$V_{\text{Low}} = \frac{V_{+\text{Low}} + V_{-\text{Low}}}{2}. \tag{5.8}$$

The corresponding resistances of the sample thermometer for both relaxation curves $R_{\text{High}}(t) = V_{\text{High}}/I_{\text{High}}$ and $R_{\text{Low}}(t) = V_{\text{Low}}/I_{\text{Low}}$ are converted to temperature using the calibration $T$-$R$ table, which is already determined. Fig. 5.2(c) schematically shows the procedure of data analysis. First, the relaxation curves are measured repeatedly (typically 5-100 times according to the signal-to-noise ratio (S/N) under the given conditions), following which they are averaged. Next, we take the derivative of $T$ with respect to $t$. While $T$ is recorded within the same time interval $\Delta t$, the resulting $dT/dt(T)$ is not obtained at regular intervals with respect to $T$. Therefore, one must perform linear interpolation to obtain a pair of $dT_{\text{High}}/dt$ and $dT_{\text{Low}}/dt$ at the same $T$. The temperature dependence of $P(T)$ is also taken into account because it changes according to $P(T) = I^2 \cdot R(T)$, where the resistance of the heater $R(T)$ is identical to that of the thermometer. Finally, we obtain a set of points $C(T)/T$ by using Eq. 5.6.

Figs. 5.3(a)-(c) show images and a schematic of the experimental setup. A Cernox 1030 BR chip was used as a thermometer, sample stage, and heater (all of these terms refer to the chip). In an actual measurements, the addenda contribution, which is the background specific heat observed even without the sample, should be minimized to achieve a good S/N. For this purpose, the bare thermometer chip was employed in the simplest possible form. A gold surface, which was coated on the Cernox chip, was removed by polishing with sandpaper, leading to decreased addenda and better thermal connection to samples. To suspend the thermometer in vacuum with a weak thermal connection to the heat bath, we used a pair of glass fibers of $\phi = 30$ $\mu$m, which were coated by gold to form electrical contacts. The resistance of the glass fiber was $\sim 80$ $\Omega$. The contact to the thermometer and heat bath was made by silver paint. Fig. 5.3(b) shows an image taken after mounting a sample. The sample was fixed on the stage by applying a tiny amount of high-vacuum grease. The copper base was thermally connected to the $^3$He pot of an Oxford Heliox. The circuit used in the long-relaxation method is illustrated in Fig. 5.3(c). The resistance of the sample thermometer was measured using the conventional 4-terminal configuration. The excitation was applied using a Keithley 6221 current source, producing simultaneous heat pulses to the sample. The voltage was then monitored using Keysight 3458A volt meter in the fast reading mode. Furthermore, resistors $R_I = 200$ k$\Omega$ and $R_V \sim$ 0-30 k$\Omega$ were used to remove the noise and optimize S/N according to each experimental condition. The filter boxes consist of low-pass filters with capacities of 22000 pF and 100 pF at room temperature and cryostat temperatures, respectively.

In Fig. 5.4(a), we show the temperature dependence of the specific heat of addenda $C_{\mathrm{Add}}$ and total specific heat $C_{\mathrm{Tot}}$ including that of the $\mathrm{YbB}_{12}$ sample, as shown by the red and black curves, respectively. For comparison, $C_{\mathrm{Add}}$ obtained using the quasi-adiabatic method, which has been employed as a conventional technique in the lab, is shown by the blue curve. $C_{\mathrm{Add}}$ measured using the quasi-adiabatic method is almost twice as large as $C_{\mathrm{Tot}}$. On the other hand, $C_{\mathrm{Add}}$ obtained using the newly developed long-relaxation method is much smaller, and it becomes $\sim 1/10$ times smaller near the lowest temperature of 0.5 K. It is also important to consider the field dependence of $C_{\mathrm{Add}}$ as it cannot be negligible when the sample signal is comparable to that of addenda. In fact, a significant field dependence is observed, as displayed in Fig. 5.4(b). Therefore, each time we changes the sample, $C_{\mathrm{Add}}$ was re-calibrated because even a minute amount of glue can significantly affect the results.

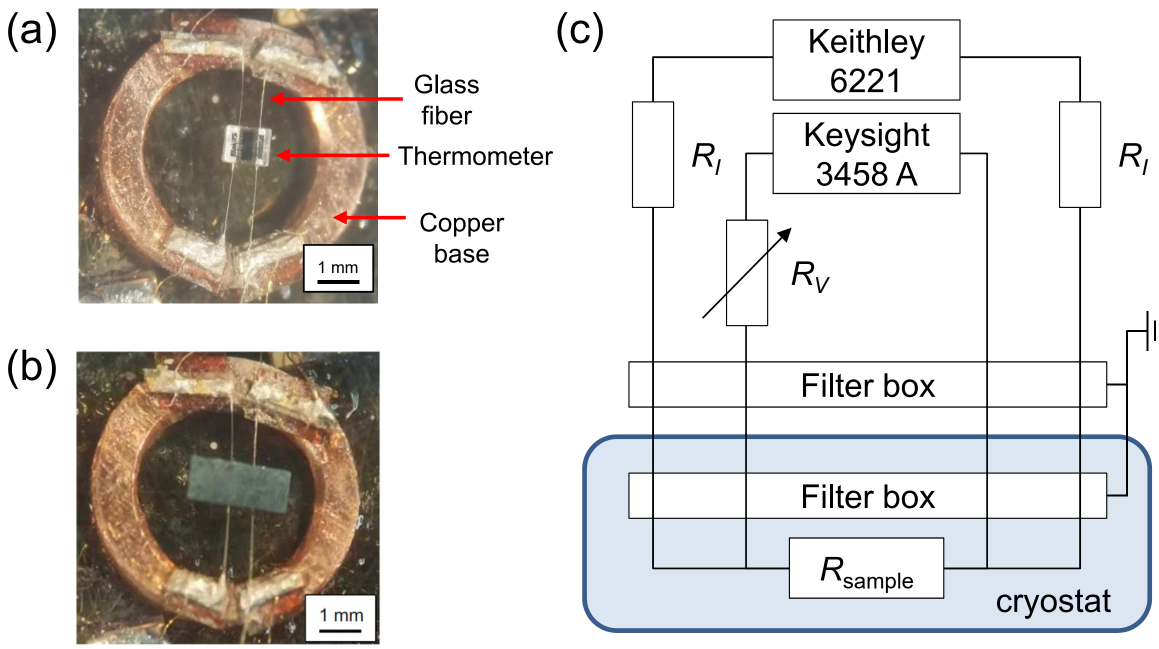


Figure 5.3: (a), (b) Images of the setup for the specific heat measurement. The thermometer is connected to a copper heat bath by glass fibers with $\phi = 30$ $\mu$m (a) without a sample and (b) with a $YbB_{12}$ sample. (c) Schematic of the circuit used in the measurements.

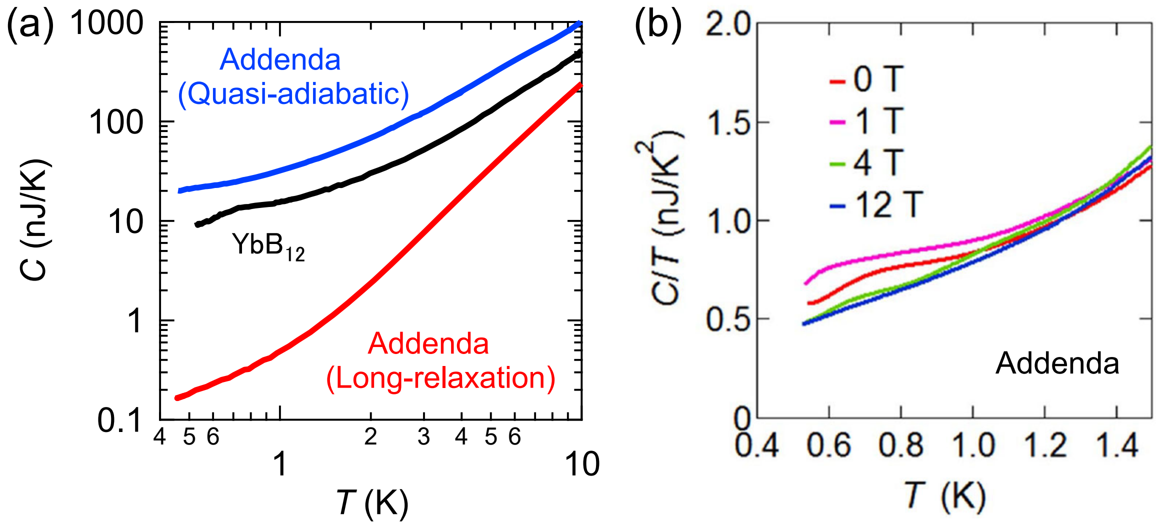


Figure 5.4: (a) Log-log plot of the measured total specific heat $C$ without (the red curve) and with a $YbB_{12}$ sample (the black curve) as a function of $T$. For comparison, the addenda data obtained using the quasi-adiabatic method (the blue curve) is also displayed. (b) Temperature dependence of the addenda contribution measured using the long-relaxation method with various fields.

### 5.2.2 Thermal transport

In addition to the electrical transport, thermal conductivity measurements provide pivotal information on both charged and neutral quasiparticle excitations of the underlying system. We will describe the principles and experimental details below. Passing a heat current through materials induces a thermal gradient. In the steady state, this response can be written as

$$q_i = -\kappa_{ij} \partial_j T, \tag{5.9}$$

where $q_i$ $(i = x, y, z)$ is the thermal current density along the $i$-direction, $\kappa_{ij}$ is the thermal conductivity tensor, and $\partial_j T$ is the thermal gradient along the $j$-direction. Assuming that the heat flows only in the $xy$-plane for simplicity, this relation can be expressed as

$$\begin{pmatrix} q_x \\ q_y \end{pmatrix} = \begin{pmatrix} \kappa_{xx} & \kappa_{xy} \\ -\kappa_{xy} & \kappa_{xx} \end{pmatrix} \begin{pmatrix} \partial_x T \\ \partial_y T \end{pmatrix}. \tag{5.10}$$

A plate-like sample is desirable to well define a uniform thermal current and thermal gradient. In a typical experimental setup, one side of the sample is attached to the heat bath, while the other side is connected to the heater, as shown in Fig. 5.5(a). In this setup, $q_x = Q/wt$, $q_y = 0$, $-\partial_x T = \Delta T_x/\ell$, and $-\partial_y T = \Delta T_y/w'$. Here, $Q$ is the power released from the heater, and $\Delta T_x$ and $\Delta T_y$ are the longitudinal and transverse thermal difference given by $\Delta T_x = T_{\mathrm{H}} - T_{\mathrm{L}}$ and $\Delta T_y = T_{\mathrm{L}} - T_{\mathrm{L}'}$, respectively. $\ell$, $t$, and $w$ are dimensional factors: length, thickness, and width, respectively. It is worth noting that there are two different definitions for width: $w$ is measured from one sample edge to the other, while $w'$ is defined as the distance between two thermal contacts from L to L'. Ignoring $O(\Delta T_y)^2$, each component of the thermal conductivity tensor is finally given by

$$\begin{aligned}\kappa_{xx} &= \frac{Q}{\Delta T_x}\frac{\ell}{wt}, \\ \kappa_{xy} &= \left(\frac{\Delta T_y}{Q}\right)\left(\frac{\Delta T_x}{Q}\right)^2 \frac{\ell^2}{ww't} \\ &= \left(\frac{\Delta T_y}{Q}\right)\frac{wt}{w'}\kappa_{xx}^2. \end{aligned} \tag{5.11}$$

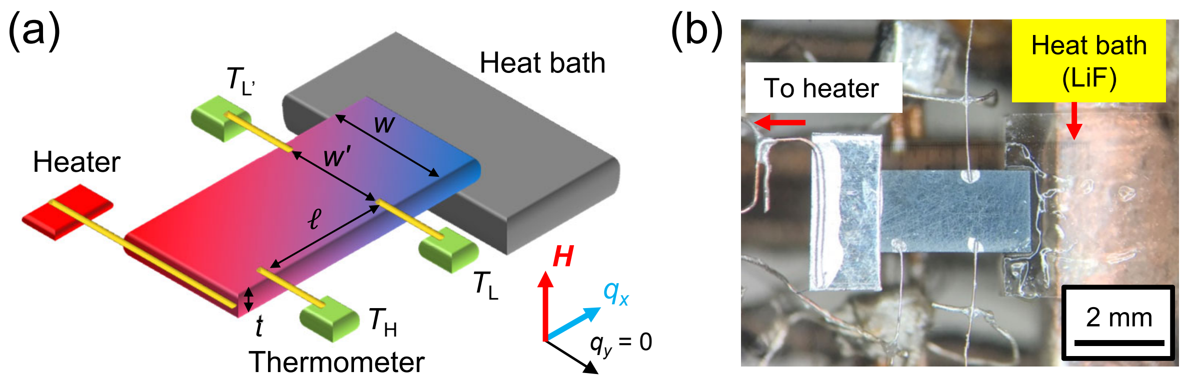


Figure 5.5: (a) Schematic of thermal conductivity measurement using the steady-state method. (b) Image of the actual setup. The $YbB_{12}$ sample (the black rectangle in the middle) is placed on the LiF heat bath (the transparent object). A heat current is passed through the silver plate (the silver rectangle on the left), which is connected to the heater.

In practice, the thermal contacts are inevitably misaligned. Therefore, the transverse response can be contaminated by the longitudinal signal, and vice versa. One can cancel this effect by inverting the sign of the field direction, as the longitudinal and transverse responses are symmetric and anti-symmetric, respectively, with respect to the external magnetic field:

$$\Delta T_x(H) = \Delta T_x(-H), \tag{5.12}$$

$$\Delta T_y(H) = -\Delta T_y(-H). \tag{5.13}$$

Therefore, the misalignment effect can be canceled out as

$$\Delta T_x(|H|) = \frac{\Delta T_x(H) + \Delta T_x(-H)}{2} \tag{5.14}$$

$$\Delta T_y(|H|) = \frac{\Delta T_y(H) - \Delta T_y(-H)}{2}. \tag{5.15}$$

Although this cancellation works in principle, it is still important to reduce the misalignment to improve S/N, especially when the $\kappa_{xy}$ of the sample is small. The misalignment angle can be estimated as $\Delta T_y(0)/\Delta T_x(0)$. In the following thermal Hall conductivity experiments on $YbB_{12}$, we achieved a misalignment of less than 1 %.

The sequence of the measurements is as follows. We stabilize the base temperature $T_\mathrm{B}$ and record the resistance of the thermometers $R_\mathrm{S}$ without applying power. These sets of data were used for the $T$-$R$ calibration table of each thermometer. We then applied a heat current to the sample and recorded the thermal gradient to calculate $\kappa_{ij}$ using Eq. 5.11. If we apply too much power to the sample, the linear response of the thermal gradient ($\Delta T \propto Q$) cannot be reliably evaluated. Therefore, we applied a moderate power so that $\Delta T_x/T_\mathrm{B} \sim$ 0.5-2 % and ensured that the thermal gradient response is always $Q$-linear.

Fig. 5.5(b) shows an image of the actual experimental setup. To apply a thermal current along the $x$-direction uniformly, we used a thin silver plate as a thermal contact to the heater. In addition, if the $\kappa_{xy}$ of the sample is too small, there may be a possible major contamination of $\Delta T_y$ induced by the $\kappa_{xy}$ of the copper heat bath. Thus, we utilize lithium fluoride (LiF) as an electrically insulating heat bath. In fact, LiF has a large activation gap $\sim$ of 15 eV [108] and exhibits a vanishingly small $\Delta T_y$, which can be negligibly small in the same setup [109]. The sample, LiF (the transparent material shown in Fig. 5.5(b)), and copper base were connected with high-vacuum grease, whereas the thermal contacts to the sample were made using silver paint.

We schematically show our sample cell in Fig. 5.6(a). To measure the sample temperature precisely, we employed a $RuO_2$ chip resistor as a sample thermometer. As one has to place the sample and thermometer in a practical vacuum environment, it is desirable to minimize possible thermal connections to the bath (i.e., thermal ground). For this purpose, less conductive wires of twisted manganin with $\phi = 30\,\mu$m and $R_{\rm mang} \sim 200\ \Omega$ were used to make electrical contacts to the thermometers, which are rolled into coils to increase the resistance in the limited space of our sample cell. The thermometers are placed on a piece of polyimide tubes (DuPont, kapton tubes), which are attached to a fiber-reinforced-plastics (FRP) frame. To arrange the three $RuO_2$ chips and one heater independently, the sample cell consists of four sets of the same structure, including a manganin coil, thermometer/heater, and prop kapton tube. For visibility, we only show one of the above structures clearly in Fig. 5.6(a); the others are transparent.

In an ideal setup, one can simply assume that the heat current released from the heater passes solely through the sample and heat ground. However, in practice, heat leakage is inevitable through the components of the sample cell, such as the manganin wires and frame. First, if the resistance of the heater is comparable to that of the manganin wire, the Joule heating in the wire cannot be negligible. To avoid this, we used $R_Q = 10$ k$\Omega$, which is more than 100 times larger than $R_{\rm mang}$. In addition, as shown in Fig. 5.6(b), there are several possible heat-leak paths through the thermal conductance $G_{\rm m}$. If this heat leak is comparable to that from the sample thermal conductance $G_{\rm s}$, one cannot evaluate the heat current $q_{\rm s}$ through the sample reliably. According to reference [110], the $\kappa_{xx}$ of manganin is approximately 0.05 and 1 mW/cmK at 0.1 K and 1 K, respectively. This leads to $G_{\rm m}(0.1\,{\rm K}) \sim 7 \times 10^{-11}$ W/K and $G_{\rm m}(1\,{\rm K}) \sim 1.4 \times 10^{-9}$ W/K for our coils. On the other hand, the $G_{\rm s}$ of a typical $YbB_{12}$ crystal we measured can be estimated as $G_{\rm s}(0.1\,{\rm K}) \sim 5 \times 10^{-8}$ W/K and $G_{\rm s}(1\,{\rm K}) \sim 1 \times 10^{-5}$ W/K. Here, we used a dimensional factor of $wt/\ell \sim 50\,\mu$m for the calculation ($wt/\ell \sim 37\mu$m and $\sim 63\,\mu$m in sample #1 and #3, respectively). The above estimations imply that $G_{\rm s}/G_{\rm m} > 10^3$ throughout our measurement temperature range, indicating that the heat leak through the sample thermometer and manganin is negligibly small. Therefore, even with an additional 1 % of Joule heating within the manganin wire of the heater, most ($\sim 99.9\,\%$) of the power would contribute to the net thermal current $q_{\rm net}$ towards the sample. Although an accurate estimation of the heat leak through other components such as the frame is difficult, we ensured that without the sample, none of the thermometers responded to the typical power we used for the measurements.

Fig. 5.7 schematically shows the circuit for the thermal transport measurements. To simultaneously monitor the temperature of three different points, High, Low, and Low', we prepared three sets of AVS 47-B resistance bridges. The measured resistance is converted through the DC output line to a Keithley 2000 multimeter. Regarding the magnitude of heat current, an excitation current of $I_Q$ was applied from the Keithley 2400 current source. As the $T$- and $H$-dependence of the resistance in the heater $R_Q$ must be considered, the voltage $V_Q$ was also recorded using another Keithley 2000 multimeter. The heat power is given from the observed $V_Q$ as $Q = I_Q \cdot V_Q$. Low-pass (LP) filter boxes were used to cut external noise as well as for the specific heat measurements. We also used a 12-14 T solenoidal superconducting magnet (Oxford Instruments) to apply magnetic fields and a gas handing system with a $^3$He-$^4$He dilution refrigerator (Cryoconcept, DR-JT-S-200-10), the lowest temperature of the mixing chamber of which is $\sim$ 40 mK.

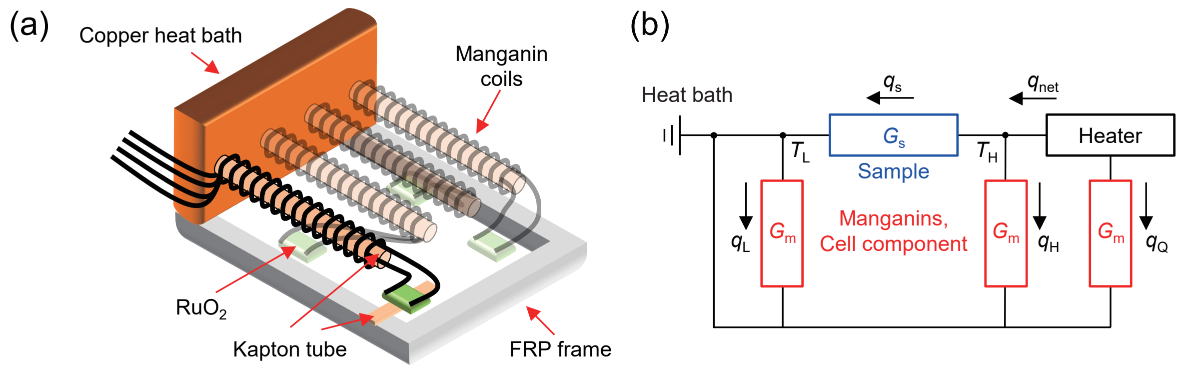


Figure 5.6: (a) Schematic of the sample cell for thermal conductivity measurement. The sample is attached to the bottom surface of the copper heat bath. A sample and the contacts between thermometers are excluded in the depiction for visibility. (b) Thermal circuit for our setup describing possible heat leaks through the manganin coils and cell components such as the FRP frame.

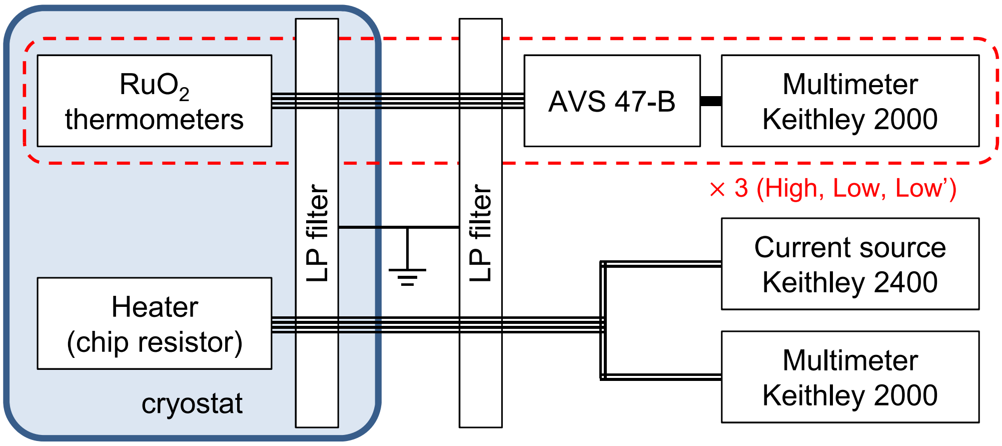


Figure 5.7: Schematic of the circuit used for the thermal conductivity measurement.

## 5.3 Results and discussion

### 5.3.1 Specific heat

Fig. 5.8(a) shows the temperature dependence of the specific heat divided by the temperature ($C/T$) of #2 and #3 (the same single crystals as in chapter 3) in zero field as blue filled and open circles, respectively. The overall temperature dependence has several characteristic structures: a slight upturn below $\sim$ 1 K, a broad hump-like anomaly around 6 K, and a steep growth above $\sim$ 10 K. It is notable that despite the upturn at low temperature, $C/T$ does not seem to approach zero as $T \to 0$: the extrapolation from above 1 K clearly has a finite intercept. This indicates that the specific heat of $YbB_{12}$ has a linear temperature dependence, which can be expressed as $C_{\mathrm{qp}} = \gamma T$, suggesting that the ground state has gapless fermionic excitations similar to those of ordinal metals. To quantitatively evaluate the $T$-linear term, we estimated other contributions as follows. First, the slight upturn below 1 K is attributed to a Schottky contribution, $C_{\mathrm{Sc}}/T$. The low-temperature enhancement of $C/T$ is well fitted by a three-level Schottky model, as shown by the green solid and dotted curves in Fig. 5.8(a). Second, the hump anomaly and steep growth above $\sim$ 10 K can be described by low-energy Einstein optical phonon modes. These anomalies have also been reported in the isostructual metallic compounds $LuB_{12}$ and $YB_{12}$ [111]. The $MB_{12}$ (M is a rare-earth element) structure can be regarded as free oscillators of rare-earth atoms in rigid cavities of $B_{24}$ cuboctahedrons, as shown in Fig. 5.9(a). Fig. 5.9(b) shows the specific heat of the isostructual $LuB_{12}$ and $YB_{12}$. Similar to our data for $YbB_{12}$, both compounds show a steep upturn in $C$ above $\sim$ 10 K. In addition, inelastic neutron scattering experiments of $YbB_{12}$ reveal 3D phonon dispersions [112]. Therefore, we attribute both the acoustic phonon ($\propto T^3$) and two optical phonon modes to $C_{\mathrm{ph}}$, which is described by the solid and dotted black lines in Fig. 5.8(a). Owing to the high Debye temperature, the acoustic phonon contribution to the total heat capacity is very small. On the other hand, the optical phonon contributions are slightly sample dependent, but the other components are almost the same in #2 and #3.

The low-temperature specific heat of $YbB_{12}$, therefore, can be written as a sum of the phonon, quasiparticle, and Schottky contributions as

$$C = C_{\rm qp} + C_{\rm ph} + C_{\rm Sc}, \tag{5.16}$$

where

$$C_{\rm qp} = \gamma T, \tag{5.17}$$

$$C_{\rm ph} = \beta T^3 + \frac{A}{T}\left(\frac{\Theta_{\rm E}}{T}\right)^2 \frac{\exp(\Theta_{\rm E}/T)}{[\exp(\Theta_{\rm E}/T)-1]^2}, \tag{5.18}$$

$$C_{\rm Sc} = \frac{B}{T^2}\left[\frac{\sum_{i=0}^{n-1}\epsilon_i^2\exp(-\epsilon_i/k_{\rm B}T)}{\sum_{i=0}^{n-1}\exp(-\epsilon_i/k_{\rm B}T)} - \left(\frac{\sum_{i=0}^{n-1}\epsilon_i\exp(-\epsilon_i/k_{\rm B}T)}{\sum_{i=0}^{n-1}\exp(-\epsilon_i/k_{\rm B}T)}\right)^2\right]. \tag{5.19}$$

Here, $\Theta_{\rm E}$ is the Einstein phonon temperature, and $\epsilon_i$ ($i$ = 1, 2, 3) is the energy levels yielding the Schottky contribution. As shown in Fig. 5.8(b), $C_{\rm qp}/T$ obtained by subtracting $C_{\rm ph}$ and $C_{\rm Sc}$ from the total $C$ is consistent between #2 and #3. The calculated $\gamma$ is $\approx$ 3.8 mJ/molK$^2$ in zero field, which is comparable to the values in isostructual metallic $LuB_{12}$ ($\gamma \approx$ 4.2 mJ/molK$^2$ [111]) and other conventional metals. We stress that the volume fraction of the impurity phases of our single crystals is estimated to be much less than 1% from high-resolution synchrotron X-ray diffraction measurements, as we discussed in subsection 3.2. Therefore, we can rule out the possibility that the finite $\gamma$ arises from impurity phases.

Next, we discuss the field dependence of the specific heat. Figs. 5.10(a)-(i) show the temperature dependence of $C/T$ below 5 K in various magnetic fields up to 12 T. The anomalies mentioned above, i.e., the low-temperature upturn and hump behavior, appear to be field dependent. At 4 T, for example, $C/T$ decreases as $T$ decreases with a downward curvature below 2 K. At 8 and 12 T, on the other hand, $C/T$ decreases almost linearly against $T$ with a steeper slope than that of the zero-field data. This low-temperature behavior may be attributed to the coupling between the magnetic field and the optical phonon modes. The field dependence of $C/T$ at the lowest temperature $T$ = 1 K is displayed in Fig. 5.11(a). The low-field anomaly around 2 T is mainly attributed to the significant change in the Schottky contribution. We also performed the

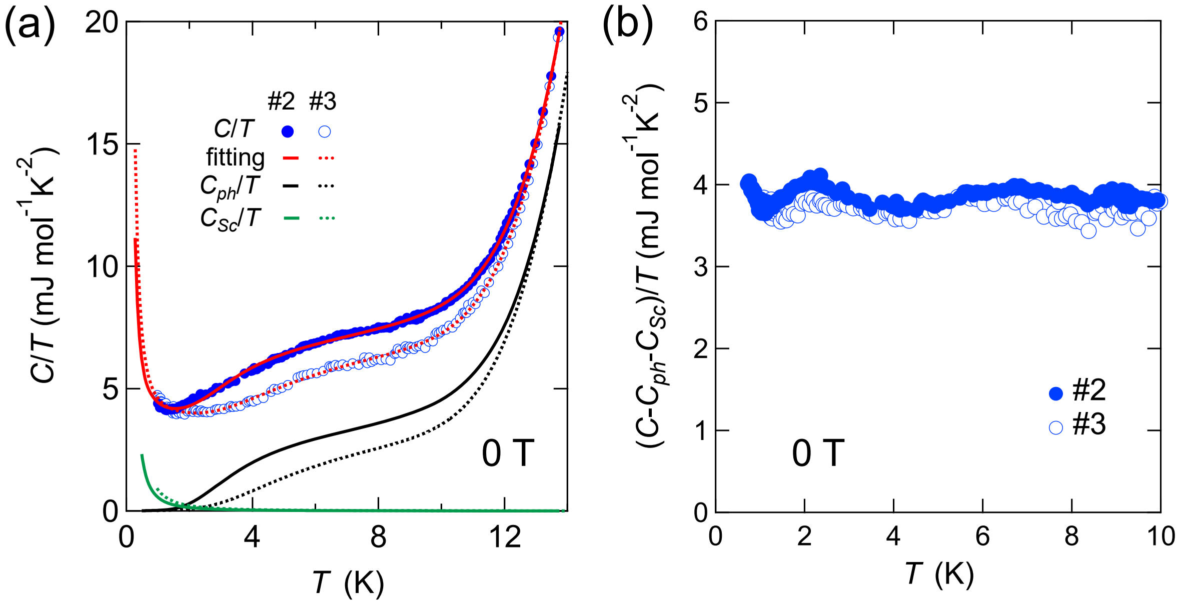


Figure 5.8: (a) Specific heat data at zero field in #2 and #3 (the blue filled and open circles, respectively). The red, black, and green curves represent the total fitting results, phonon contribution, and Schottky contribution, respectively. (b) Temperature dependence of $C/T$ subtracted by the phonon and Schottky contributions.

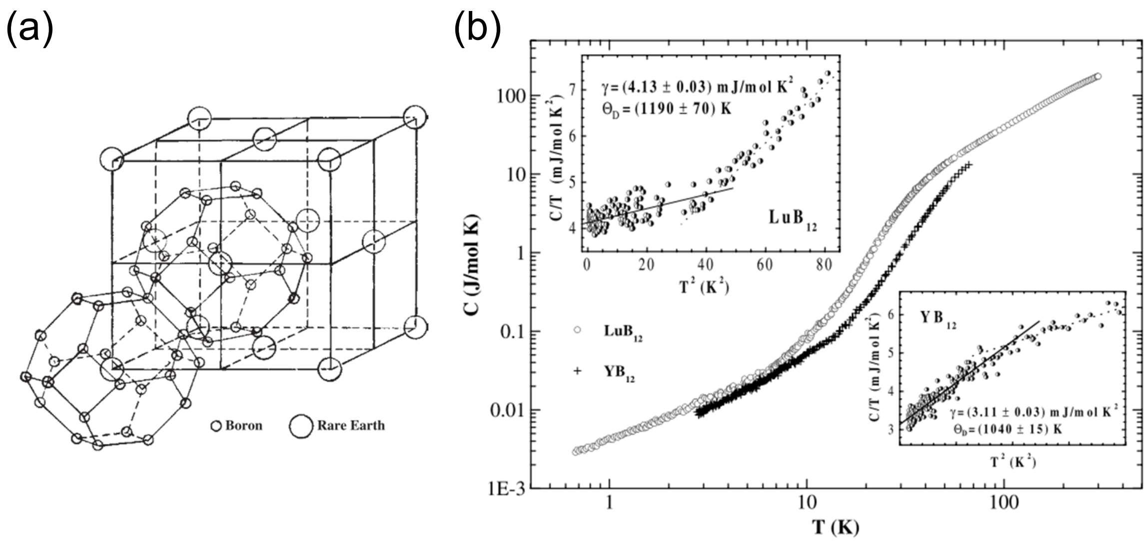


Figure 5.9: (a) Crystalline structure of $MB_{12}$ [111]. The cluster of boron forms Fedorov's cubooctahedra. (b) Specific heat of the isostructual compounds $LuB_{12}$ and $YB_{12}$ [111].

fitting of $C/T$ in fields by using the same model, Eq. 5.16, and the resulting parameters are displayed in Figs .5.11(b)-(d). Here, $\Delta_i$ is the energy splitting in the three-level model. As the field increases, $\gamma$ is slightly reduced, while the Schottky contributions are substantially affected. Although the exact estimation of $\gamma$ is difficult because of the underlying large Schottky and phonon contributions, the present results imply that the gapless fermionic excitations are affected by external fields.

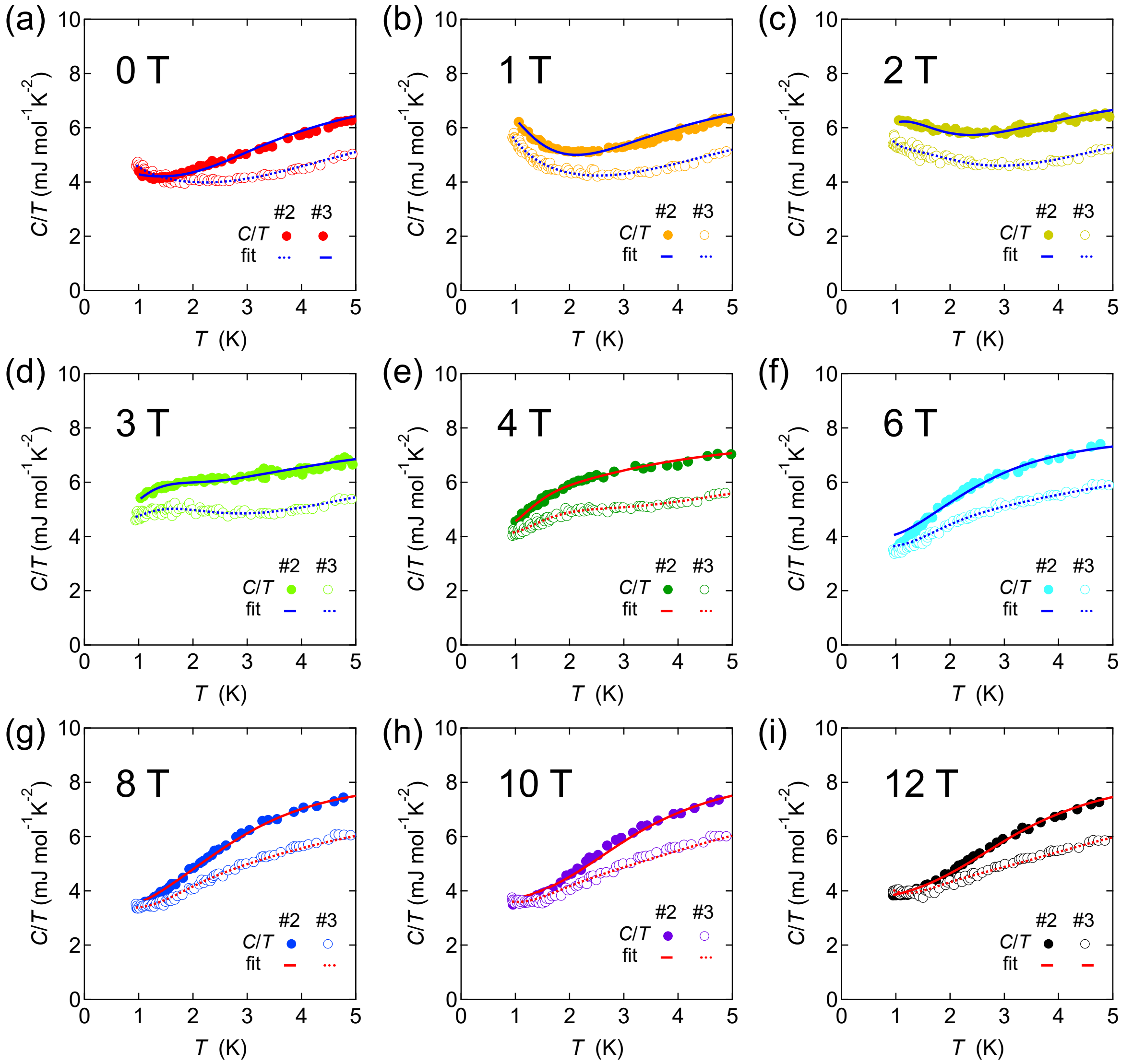


Figure 5.10: (a)-(i) Temperature dependence of $C/T$ in #2 and #3 in various fields up to 12 T.

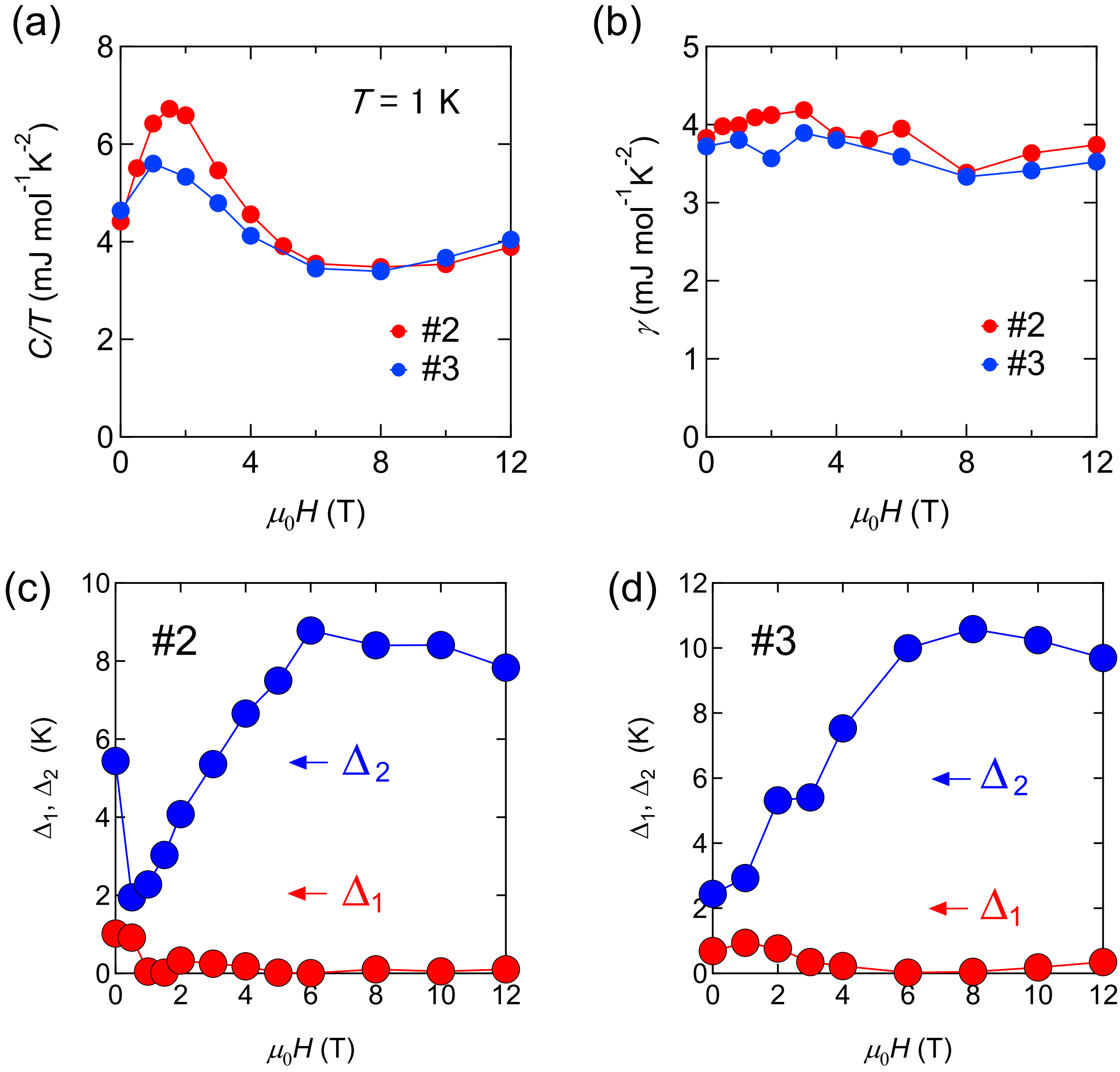


Figure 5.11: (a) Field dependence of $C/T$ in #2 and #3 at $T$ = 1 K. (b) Field dependence of the calculated $\gamma$. (c), (d) Energy splitting of the Schottky specific heat obtained in sample #2 and #3 at different fields.

### 5.3.2 Thermal conductivity

We now turn to the thermal conductivity, which shows the itinerant aspect of the neutral excitations. The red and blue circles in Fig. 5.12(a) represent the $T^2$ dependence of $\kappa_{xx}/T$ in zero field for #1 and #3, respectively. As the thermal conductivity does not contain the localized Schottky contribution, $\kappa_{xx}$ can be described as a sum of the itinerant quasiparticle and phonon contributions: $\kappa_{xx} = \kappa_{xx}^{\mathrm{qp}} + \kappa_{xx}^{\mathrm{ph}}$. To use $\kappa_{xx}$ as a probe of itinerant quasiparticles, $\kappa_{xx}^{\mathrm{ph}}$ must be extracted reliably. The solid lines in Fig. 5.12(a) are obtained by fitting low-temperature data as follows:

$$\kappa_{xx}/T = \kappa_{xx}^{0}/T + AT^2. \tag{5.20}$$

The $AT^2$ term here is attributable to phonons for the following reasons. The optical phonon modes are negligible at temperatures well below the Einstein temperature (which is 16–24 K in our samples) because of the small population of optical phonons and the low phonon group velocity. Consequently, acoustic phonons are the only carriers of heat at low temperature, and the phonon thermal conductivity is given by

$$\kappa_{xx}^{\mathrm{ph}} = \frac{1}{3}\beta T^3 v_{\mathrm{ph}} \ell_{\mathrm{ph}}, \tag{5.21}$$

where $v_{\mathrm{ph}}$ and $\ell_{\mathrm{ph}}$ are the sound velocity and mean free path of acoustic phonons, respectively. We compare $\ell_{\mathrm{ph}}$ and the effective diameter of the sample $d_{\mathrm{eff}} = 2\sqrt{wt/\pi}$ ($w$ and $t$ are the width and thickness of the crystal, respectively); $d_{\mathrm{eff}} = 0.58$ mm and 0.37 mm for #1 and #3, respectively. Using $\beta = 0.026$ and 0.017 mJ/molK$^4$ for #1 and #3, respectively, from the specific heat measurements shown in Fig. 5.8(a), as well as $v_{\mathrm{ph}}= 9.6 \times 10^3$ m/s for $LuB_{12}$ [113], we find that $\ell \approx d_{\mathrm{eff}}$ at $\sim 0.5$ K for #1 and $\sim 0.6$ K for #3. These are close to the temperatures below which $\kappa_{xx}/T$ shows $T^2$ dependence, as shown in Fig. 5.12(a), supporting the above estimation. These results suggest that at sufficiently low temperatures, $\ell_{\mathrm{ph}}$ is limited by the crystal size; that is, the samples are in the boundary scattering regime where $\kappa_{xx}^{\mathrm{ph}}/T \propto T^2$. The fact that the systems are in this regime is also supported by the $A$ values of #1 and #3. In the boundary scattering regime, $A$ is proportional to $\beta d_{\mathrm{eff}}$. The ratio of the $A$ values between #1 and #3, as determined from the $T$ dependence of $\kappa_{xx}/T$, is $\sim 2.6$. This value is close to the ratio ($\sim 2.5$) of $\beta d_{\mathrm{eff}}$ of the two crystals, indicating the proportionality of $A$ and $\beta d_{\mathrm{eff}}$.

Fig. 5.12(b) shows the low-temperature thermal conductivity data, where the phonons are in the boundary scattering regime. $\kappa_{xx}/T$ extrapolated to zero temperature yields definite non-zero intercepts in both crystals: $\kappa_{xx}^{0}/T \neq 0$. Thus, our results provide evidence of a finite residual linear term in $\kappa_{xx}^{\mathrm{qp}}$ (that is, the presence of itinerant gapless fermionic excitations). We stress that the finite $\kappa_{xx}^{0}/T$ is not caused by phonons as discussed above. It is known that localized vibrational modes, such as tunnelling states in amorphous solids, can contribute to a finite $\gamma$ [114]. However, such excitations are localized and do not carry heat, resulting in the absence of $\kappa_{xx}^{0}/T$. Moreover, these vibrational modes may act as scattering centers for phonons. This yields a $T^{-1}$ dependence of $\ell_{\mathrm{ph}}$, leading to $\kappa_{xx} \propto T^2$, in contrast to the observed non-zero $\kappa_{xx}^{0}/T$. It should also be stressed that the observed finite $\kappa_{xx}^{0}/T$ does not originate from charged quasiparticles, in contrast to the situation in conventional metals. Evidence for this is given by the spectacular violation of the Wiedemann–Franz (WF) law, which connects the electronic thermal conductivity to the electrical resistivity (see section 1.4.4 for details). In moderately pure metals at low temperatures, $L = \kappa_{xx}^{\mathrm{qp}}\rho_{xx}/T \leq L_0$ is generally satisfied, where $L_0 = \pi^2 k_{\mathrm{B}}^2/3e^2$ is the Lorenz number. The values of $\kappa_{xx}^{0}\rho_{xx}^{0}/T$ for #1 and #3 are found to be $\sim 6 \times 10^4 L_0$ and $\sim 5 \times 10^3 L_0$, respectively. It is highly unlikely that the surface metallic region significantly violates the WF law. In fact, it is well established that the WF law holds in 2D metals, even in the quantum Hall regime. The WF expectation of $\kappa_{xx}^{0}/T$ from the metallic surface is less than $10^{-4}$ W/K$^2$m, which is by far smaller than the experimental resolution. These results lead us to conclude that the neutral fermions in the insulating bulk of the samples are responsible for the finite $\kappa_{xx}^{0}/T$. In other words, as the bulk resistivity diverges as $T \to 0$, the Lorenz number for the heat-carrying quasiparticles also diverges. Thus, the thermal conductivity and specific heat data very strongly suggest the presence of highly mobile and gapless neutral fermionic excitations. The results for $YbB_{12}$ are in contrast to those for $SmB_6$, where a $T$-linear term is present in $C$ [71, 99–101] but absent in $\kappa_{xx}$ at zero field [101–103].

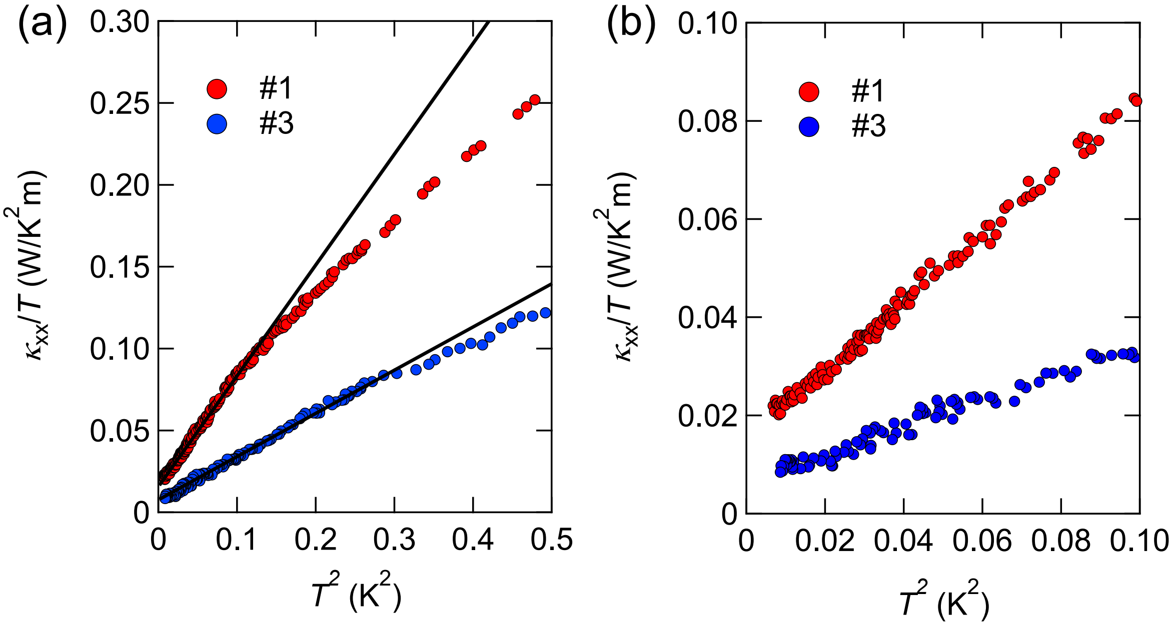


Figure 5.12: (a) Thermal conductivity in #1 and #3 divided by temperature as a function of $T^2$. The solid lines represent the linear fitting performed in the low-temperature regime. (b) Expanded view of (a) below $T^2 = 0.1$ K.

Now, we discuss the field dependence of thermal conductivity in $YbB_{12}$. Figs. 5.13(a)-(b) plot $\kappa_{xx}/T$ as a function of $T^2$ in various magnetic fields for #1 and #3. $\kappa_{xx}/T$ is slightly enhanced on applying a magnetic field. We fit the data using Eq. 5.21 to extract the phonon and quasiparticle contributions. The fact that all the data can be linearly fitted clearly indicates that the phonons remain in the boundary scattering regime even in the magnetic fields. The finite $\kappa^0_{xx}/T$ is resolved in the whole field range up to 12 T for both samples. We also plotted $\kappa_{xx}/T$ as a function of $T$ in Fig. 5.13(c). Although the extrapolation of $\kappa_{xx}/T$ to $T \to 0$ in this plot estimates the lower limit of $\kappa^0_{xx}/T$, finite intercepts are resolved in all the data, implying that the neutral fermions exist regardless of the $\alpha$ value (the exponent of the phonon power). Interestingly, $\kappa^0_{xx}/T$ estimated by the linear fitting shows non-monotonic growth on applying fields, as shown in Fig. 5.13(d). The present results imply that the neutral fermions couple to magnetic fields. Another prominent feature is that the $\kappa^0_{xx}/T$ of #1 is much more enhanced by the magnetic fields than that of #3: the $\kappa^0_{xx}/T$ of #1 shows a steep increase at low fields and becomes nearly twice that at 0 T, while the $\kappa^0_{xx}/T$ of #3 is only slightly enhanced. Given that #1 shows a larger activation energy than #3, this result indicates that higher-quality crystals with lower impurity scattering rates exhibit a larger magneto-thermal conductivity. As larger $\kappa^0_{xx}/T$ values arise from longer mean free paths, this result suggests (as might be expected) that the more mobile neutral fermions are more strongly influenced by a magnetic field.

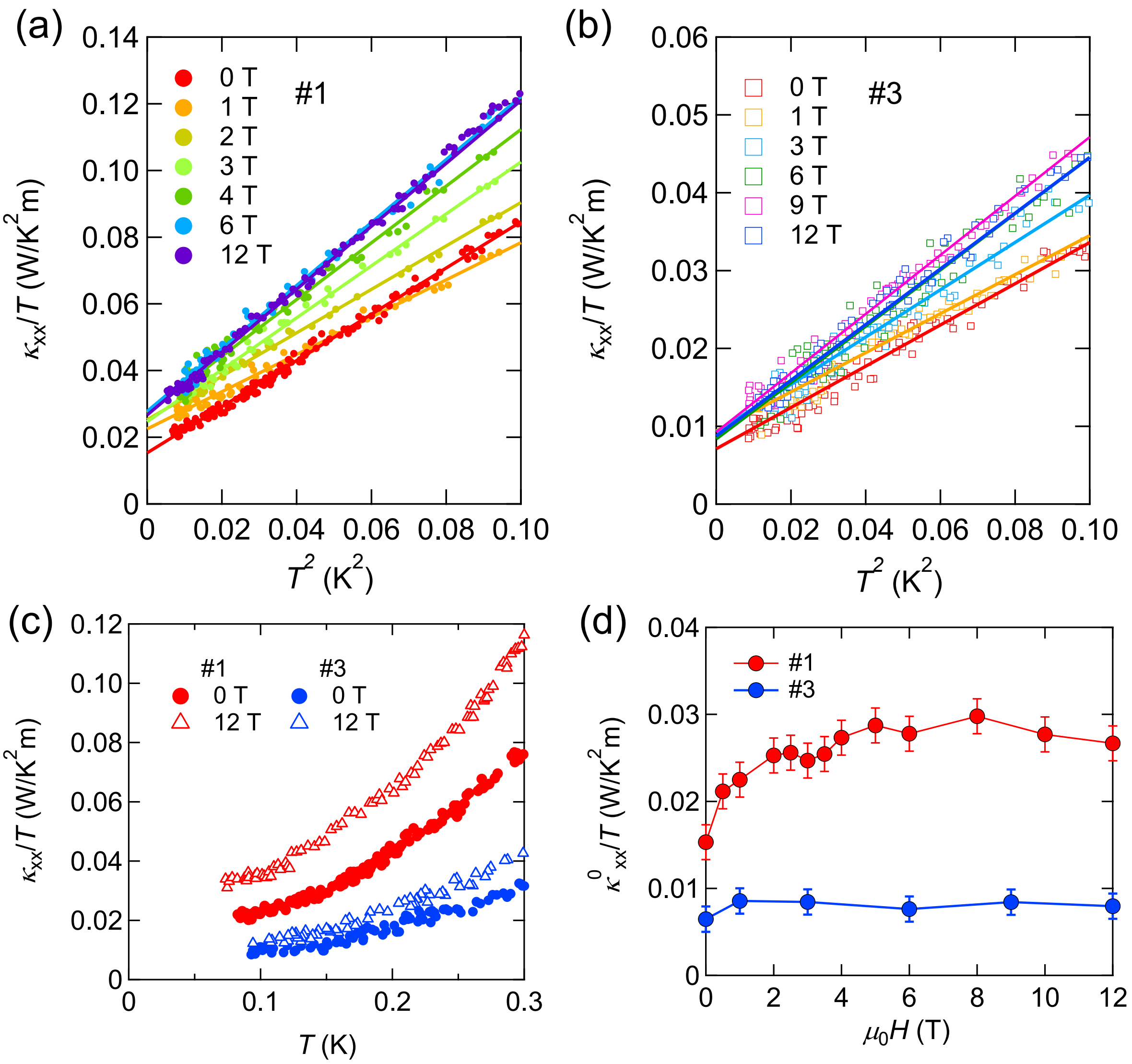


Figure 5.13: (a), (b) Thermal conductivity divided by temperature as a function of $T^2$ under magnetic fields for samples #1 and #3. The solid lines are the fitting results, showing a finite $\kappa^0_{xx}/T$ throughout the field range for both samples. (c) $\kappa_{xx}/T$ against $T$. (d) Field dependence of $\kappa^0_{xx}/T$ obtained by from linear fit shown in (a) and (b).

### 5.3.3 Mean free path of the neutral fermions

The observed $\kappa_{xx}^0/T$ for #1 is nearly twice that for #3, while $\gamma$ for #2, the quality of which is very close to that of #1, coincides with that for #3. This quantitative difference derives from the mean free path of neutral fermions in the two types of crystals. The quasiparticle thermal conductivity is related to the specific heat by

$$\frac{\kappa_{xx}^{\mathrm{qp}}}{T} = \frac{1}{3}\gamma v_F \ell_{\mathrm{qp}} \tag{5.22}$$

where $v_F$ is the Fermi velocity and $\ell_{\mathrm{qp}}$ is the mean free path of the neutral fermions. Therefore, the $\ell_{\mathrm{qp}}$ of #1 and #2 is twice that of #3. Interestingly, this indicates that more strongly insulating crystals with larger activation energies have higher-mobility neutral quasiparticles. A fascinating question is whether the CNFs are responsible for the QOs. To examine this, we estimate $\ell_{\mathrm{qp}}$ from Eq. 5.22 by assuming that $v_F$ is given by the Fermi velocity obtained from the SdH oscillations in the insulating state, which we discussed in section 3.3.1. By assuming a simple spherical Fermi surface, we obtain $v_F = \hbar k_F/m^* \approx 1.3 \times 10^4$ m/s from the SdH oscillations, where $k_F \approx 1.7$ nm$^{-1}$ is the Fermi wave number and $m^* \approx 15 m_e$ is the effective mass. We estimate $\ell_{\mathrm{qp}} \approx 54$ and 25 nm, which is nearly 70 and 30 times larger than the lattice constant $a \approx 5.28$, for #1 and #3, respectively. Although the mean free path is large, the heavy effective mass leads to rather small mobilities $\mu$:

$$\mu = \frac{e\ell_{\mathrm{qp}}}{m^* v_{\mathrm{F}}} \tag{5.23}$$

is approximately 480 cm$^2$/Vs (0.048 T$^{-1}$) for #1 and 230 cm$^2$/Vs (0.023 T$^{-1}$) for #3. According to Eq. 2.14, the reciprocal of the mobility corresponds to the characteristic magnetic fields $B_{\mathrm{c}}$, above which QOs begin to develop. The above estimation corresponds to $B_{\mathrm{c}} \sim 21$ T and 43 T for #1 and #3, respectively. This simplified model explains why magnetic fields of 30–40 T are needed to resolve the SdH oscillations in #1 and why the oscillatory amplitudes in #3 are much smaller than those in #1. Therefore, this rather crude estimation suggests that the enhanced thermal conductivity in zero field and the visible SdH effect at high fields in the sample with large $\ell_{\mathrm{qp}}$ are intimately connected. The present observations for several crystals are consistent with this scenario, where CNFs are responsible for the QOs.

Finite values of both $\gamma$ and $\kappa_{xx}^0/T$ in the insulating state have been reported in a quantum-spin-liquid candidate, the organic compound $\mathrm{EtMe_3Sb[Pd(dmit)_2]_2}$ (DMIT) having a 2D triangular lattice [14, 115]. In DMIT, finite $\gamma$ and $\kappa_{xx}^0/T$ have been discussed in terms of electrically neutral spinons forming the Fermi surface. In addition, in DMIT, a $T$-independent Pauli-paramagnetic-like magnetic susceptibility $\chi$ is observed, and the Wilson ratio $R_W$ is close to unity, which is a basic property of metals [116] (see subsection 1.4.3 for details). As shown in Fig. 3.1(c), a temperature-independent $\chi$ is also observed in $\mathrm{YbB_{12}}$, and it may be ascribed to the van Vleck contribution within the $J$ =7/2 multiplet, although this contribution has not been quantitatively estimated. An alternative explanation is that the neutral fermions give rise to a Pauli-paramagnetic-like $\chi$. A simple estimation of $R_{\mathrm{W}}$ using the measured $\chi \approx 3 \times 10^{-3}$ emu/mol and $\gamma \approx 4$ mJ/molK$^2$ yields $R_{\mathrm{W}} \approx 100$, which is comparable to that reported in some spin-liquid systems [79]. In DMIT, the quantum oscillations have not been observed up to 32 T, although its possible observation was suggested theoretically [117]. Thus, more experiments are needed for quantitative comparisons between these two extraordinary systems.

### 5.3.4 Thermal Hall angle

As discussed in section 2.4.2, an observable thermal Hall signal has been proposed within a theoretical framework, where neutral fermions are responsible for the QOs in KIs [78, 117]. The neutral fermions are expected to experience the Lorentz force as the conduction electrons in metals do, forming Landau quantization in a magnetic field and giving rise to the QOs. In an attempt to observe such an effect, we measured the thermal Hall conductivity $\kappa_{xy}$. The tangent of the thermal Hall angle

$$\tan\theta_{\mathrm{H}} = \frac{\kappa_{xy}}{\kappa_{xx}} = \omega_{\mathrm{c}}\tau \tag{5.24}$$

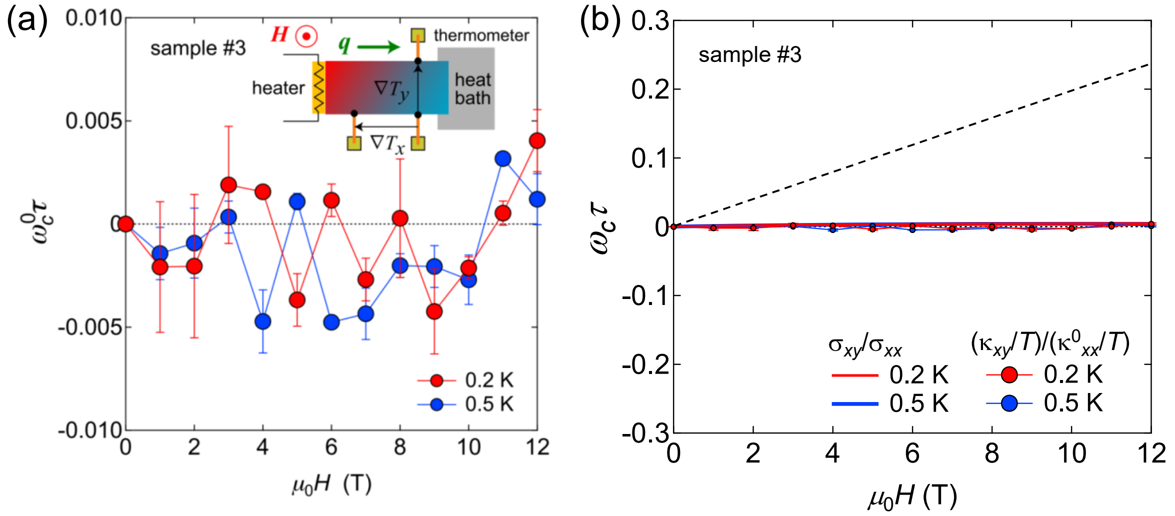


Figure 5.14: (a), (b) Thermal Hall angle at $T$ = 0.2 and 0.5 K with different scales. The inset of (a) shows the setup for the thermal Hall conductivity measurements. The dotted line in (b) shows the $B$-linear Hall response expected in a conventional metal, in which QOs appear at approximately 40 T.

provides similar information as the electrical Hall angle in conventional metals. Here, $\omega_c = (eb)_{\text{eff}}/m^*$ corresponds to the cyclotron frequency of the neutral fermion, where $b$ is the effective magnetic field experienced by neutral fermions, and $\tau$ is the scattering time. Fig. 5.14(a) shows the field dependence of $\omega_c^0\tau \equiv (\kappa_{xy}/T)/(\kappa^0_{xx}/T)$ at 0.2 and 0.5 K. As $\kappa_{xx} > \kappa^0_{xx}$, $\omega_c^0\tau$ yields the upper limit for $\omega_c\tau$. As can be observed in the data, no discernible thermal Hall effect is observed at both temperatures; $\omega_c^0\tau$, and hence, $\omega_c\tau$ are less than 0.005, which is less than our experimental resolution. In conventional metals with a single carrier type, $\omega_c\tau = eB\tau/m^*$ is of the order of unity at the magnetic field where the QOs appear. As the SdH oscillations are observed around 40 T, the thermal Hall angle at 10 T could be expected to be of the order of 0.2, which is much larger than the observed thermal Hall angle. This rough estimation is also shown by the dotted line in Fig. 5.14(b). As expected by the insulating behavior in resistivity, the electrical Hall angle is also vanishingly small compared to the above expectation (Fig. 5.14(b)), clearly implying that the conventional electrons cannot be the source of the QOs. These vanishingly small Hall angles may suggest that $(eb)_{\text{eff}}$ is significantly different from $eB$ [109, 118]. However, it is premature to conclude that the neutral fermions are not responsible for the SdH oscillations, because the small thermal Hall angle may be explained by a nonlinear $B$ dependence of $b$ or the presence of electron- and hole-like pockets of neutral fermions. In the latter scenario, compensation effects may reduce the thermal Hall signal considerably. The presence of a Fermi surface of neutral fermions and the coupling to an external magnetic field with a negligible thermal Hall angle call for further studies.

## 5.4 Conclusion

In this chapter, we presented the results of the specific heat and thermal conductivity measurements of $YbB_{12}$ single crystals, in which we found the QOs discussed in chapter 3, down to the dilution temperature with various magnetic fields of up to 12 T. Remarkably, terms with linear temperature dependence in both the specific heat and thermal conductivity, which are comparable to those in ordinal metals, were clearly resolved. Nevertheless, the resistivity shows clear activation-type behavior. Thus, the sizable fermionic contributions in thermal conductivity lead to the strong violation of the Wiedemann-Franz law, which reveals exotic bulk properties in $YbB_{12}$: it is electrically insulating but thermally metallic. Our observations, therefore, impose novel gapless excitations of CNFs. Furthermore, they are significantly affected by external fields. Although it is tempting to conclude that the observed neutral fermions are the source of the QOs at high fields, direct evidence was not provided by the thermal Hall angle measurements. Nevertheless, the scenario cannot be completely ruled out: the rough estimations of the mean free path and mobility of the neutral fermions as well as their sample dependence are consistent with an emergent Fermi surface of neutral fermions. Our findings therefore calls for further theoretical and experimental investigations on KIs to explain the origin of the CNFs in $YbB_{12}$ and their relation to the unconventional QOs observed in the insulating phase of KIs.

# 6 Conclusion

The textbook definition of metals is that they are materials which possessing a Fermi surface in momentum space. The presence of a Fermi surface is manifested by observations of QOs in magnetic fields and $T$-linear terms in specific heat and thermal conductivity. We have presented a series of experiments on the KI $YbB_{12}$ and found exotic electronic properties.

We found that $YbB_{12}$ shows QOs not only in magnetization, but also in resistivity (SdH effect), although it is electrically insulating. The SdH oscillations still occur above the insulator-metal transition critical field, and the oscillatory amplitude shows Lifshitz-Kosevich behavior in both states, indicating that fermions contribute to Landau quantization. Angle-resolved experiments captured the 3D geometry of the frequency, suggesting that the insulating bulk possesses an unconventional Fermi surface of CNFs. Interestingly, our results indicate that the Fermi surface of CNFs still contributes to the SdH effect, although it progressively depopulates with increasing field. CNFs also exhibit intriguing properties such as an extremely small $g$-factor and the field enhancement of the cyclotron mass $m^*$. Moreover, the large Sommerfeld coefficient $\gamma$ and FL transport coefficient $A_2$ in the field-induced metallic state show strong deviation from the universal Kadowaki-Woods ratio. The present results indicate the coexistence of two fluids in the metallic state, CNFs and the conventional charged heavy fermions. They strongly scatter each other and may give rise to the non-FL transport. Our pulsed-field experiments revealed highly exotic electronic properties of KIs.

We also conducted low-temperature specific heat and thermal conductivity measurements with various fields to study low-energy excitations in $YbB_{12}$. Surprisingly, we observed finite $T$-linear terms in both specific heat and thermal conductivity, which are comparable to those of ordinal metals. The sizable fermionic thermal conductivity leads to a remarkable violation of the WF law, indicating that $YbB_{12}$ is electrically insulating but thermally metallic. The present results suggest that charge-neutral gapless fermionic excitations occur in the ground state of $YbB_{12}$ and are highly mobile. Moreover, despite the charge neutrality, they are influenced by applied magnetic fields. Although it is tempting to link the observed fermionic thermal transport to the charge-neutral Fermi surface detected in the pulsed-field experiments, our thermal Hall conductivity measurements did not provide direct evidence to link these observations. Thus, we leave the problem of the relationship between the mobile neutral fermions and the QOs for future work.

Thus far, we have discussed a series of results providing evidence for “metallic” behaviors in the KI $YbB_{12}$, although it is a charge insulator. Our studies revealed exotic electronic properties and non-trivial emergent quasiparticles in this unconventional quantum state, which are expected to motivate further investigations in the future.

# References

[1] J. Kondo, Prog. Theor. Phys. **32**, 37 (1964).

[2] K. G. Wilson, Rev. Mod. Phys. 47, 773 (1975).

[3] N. Andrei, K. Furuya and J. H. Lowenstein, Rev. Mod. Phys. **55**, 331 (1983).

[4] F. D. M. Haldane, Phys. Rev. Lett. **40**, 416 (1978).

[5] P. Coleman, arXiv:1509.05769v1 (2015).

[6] S. Burdin, A. Georges, and D. R. Grempel, Phys. Rev. Lett. **85(5)**, 1048 (2000).

[7] S. Doniach, Physica B **91**, 231 (1977).

[8] C. M. Varma, Rev. Mod. Phys. **92**, 31001 (2019).

[9] N. Mott, Philos. Mag. **30:2**, 403 (1974).

[10] M. Dzero, J. Xia, V. Galitski, and P. Coleman, Annu. Rev. Condens. Matter Phys. **7**, 249 (2016).

[11] K. Kadowaki, and S.B. Woods, Solid State Commun. **58** 507 (1986).

[12] N. Tsujii, H. Kontani, and K. Yoshimura, Phys. Rev. Lett. **94**, 057201 (2005).

[13] R. Franz, and G. Wiedemann, Ann. Phys. **165**, 497 (1853).

[14] M. Yamashita, N. Nakata, Y. Senshu, M. Nagata, H. M. Yamamoto, R. Kato, T. Shibauchi, and Y. Matsuda, Science, **328**, 1246 (2010).

[15] H. Murayama, Y. Sato, X. Z. Xing, T. Taniguchi, S. Kasahara, Y. Kasahara, M. Yoshida, Y. Iwasa, and Y. Matsuda, Phys. Rev. Res. **2**, 013099 (2020).

[16] G. Grissonnanche, A. Legros, S. Badoux, E. Lefrançois, V. Zatko, M. Lizaire, F. Laliberté, A. Gourgout, J. S. Zhou, S. Pyon, T. Takayama, H. Takagi, S. Ono, N. Doiron-Leyraud, and L. Taillefer, Nature **571**, 376 (2019).

[17] H. Pfau, S. Hartmann, U. Stockert, P. Sun, S. Lausberg, M. Brando, S. Friedemann, C. Krellner, C. Geibel, S. Wirth, S. Kirchner, E. Abrahams, Q. Si, and F. Steglich, Nature. **484**, 493 (2012).

[18] Y. Machida, K. Tomokuni, K. Izawa, G. Lapertot, G. Knebel, J. P. Brison, and J. Flouquet, Phys. Rev. Lett. **110**, 236402 (2013).

[19] R. Mahajan, M. Barkeshli, and S. A. Hartnoll, Phys. Rev. B **88**, 125107 (2013).

[20] G. A. R. v. Dalum, A. K. Mitchell, and L. Fritz, Phys. Rev. B **102**, 041111(R) (2020).

[21] M. Z. Hasan, and C. L. Kane, Rev. Mod. Phys. **82**, 3045 (2010).

[22] J. E. Moore, Nature **464**, 194 (2010).

[23] L. Fu and C. L. Kane, Phys. Rev. B **76**, 45302 (2008).

[24] M. He, H. Sun, and Q.L. He, Frontiers of Physics **14**, 43401 (2019).

[25] M. Dzero, K. Sun, V. Galitski, and P. Coleman, Phys. Rev. Lett. **104**, 106408 (2010).

[26] A. Menth, E. Buehler, and T. H. Geballe, Phys. Rev. Lett. **22**, 295 (1969).

[27] T. Takimoto, J. Phys. Soc. Jpn. **80**, 123710 (2011).

[28] F. Lu, J. Zhao, H. Weng, Z. Fang, and X. Dai, Phys. Rev. Lett. **110**, 096401 (2013).

[29] V. Alexandrov, M. Dzero, and P. Coleman, Phys. Rev. Lett. **111**, 226403 (2013).

[30] F. Chen, C. Shang, Z. Jin, D. Zhao, Y. P. Wu, Z. J. Xiang, Z. C. Xia, A. F. Wang, X. G. Luo, T. Wu, and X. H. Chen, Phys. Rev. B **91**, 205133 (2015).

[31] Y. S. Eo, A. Rakoski, J. Lucien, D. Mihaliov, Ç. Kurdak, P. F. S. Rosa, and Z. Fisk, Proc. Natl. Acad. Sci. **116**, 12638 (2019).

[32] S. Rö*β*ler, T. H. Jang, D. J. Kim, L. H. Tjeng, Z. Fisk, F. Steglich, and S. Wirth, Proc. Natl. Acad. Sci. **111**, 4798 (2014).

[33] W. Ruan, C. Ye, M. Guo, F. Chen, X. Chen, G. M. Zhang, and Y. Wang, Phys. Rev. Lett. **112**, 136401 (2014).

[34] X. Zhang, N. P. Butch, P. Syers, S. Ziemak, R. L. Greene, and J. Paglione, Phys. Rev. X. **3**, 011011 (2013).

[35] M. Neupane, N. Alidoust, S. Y. Xu, T. Kondo, Y. Ishida, D. J. Kim, C. Liu, I. Belopolski, Y. J. Jo, T. R. Chang, H. T. Jeng, T. Durakiewicz, L. Balicas, H. Lin, A. Bansil, S. Shin, Z. Fisk, and M. Z. Hasan, Nat. Commun. **4**, 2991 (2013).

[36] N. Xu, X. Shi, P. K. Biswas, C. E. Matt, R. S. Dhaka, Y. Huang, N. C. Plumb, M. Radović, J. H. Dil, E. Pomjakushina, K. Conder, A. Amato, Z. Salman, D. M. K. Paul, J. Mesot, H. Ding, and M. Shi, Phys. Rev. B **88**, 121102 (2013).

[37] J. Jiang, S. Li, T. Zhang, Z. Sun, F. Chen, Z. R. Ye, M. Xu, Q. Q. Ge, S. Y. Tan, X. H. Niu, M. Xia, B. P. Xie, Y. F. Li, X. H. Chen, H. H. Wen, and D. L. Feng, Nat. Commun. **4**, 3010 (2013).

[38] P. Hlawenka, K. Siemensmeyer, E. Weschke, A. Varykhalov, J. Sánchez-Barriga, N. Y. Shitsevalova, A. V. Dukhnenko, V. B. Filipov, S. Gabáni, K. Flachbart, O. Rader, and E. D. L. Rienks, Nat. Commun. **9**, 517 (2018).

[39] T. Caldwell, A. P. Reyes, W. G. Moulton, P. L. Kuhns, M. J. R. Hoch, P. Schlottmann, and Z. Fisk, Phys. Rev. B **75**, 075106 (2007).

[40] W. T. Fuhrman, J. R. Chamorro, P. A. Alekseev, J. M. Mignot, T. Keller, J. A. Rodriguez-Rivera, Y. Qiu, P. Nikolić, T. M. McQueen, and C. L. Broholm, Nat. Commun. **9**, 1539 (2018).

[41] D. J. Kim, J. Xia, and Z. Fisk, Nat. Mater. **13**, 466 (2014).

[42] P. Syers, D. Kim, M.S. Fuhrer, and J. Paglione, Phys. Rev. Lett. **114**, 096601 (2015).

[43] S. Wolgast, Ç. Kurdak, K. Sun, J. W. Allen, D. J. Kim, and Z. Fisk, Phys. Rev. B **88**, 180405 (2013).

[44] S. Thomas, D.J. Kim, S.B. Chung, T. Grant, Z. Fisk, and J. Xia, Phys. Rev. B **94**, 205114 (2016).

[45] J. Kim, C. Jang, X. Wang, J. Paglione, S. Hong, J. Lee, H. Choi, and D. Kim, Phys. Rev. B **99**, 245148 (2019).

[46] Y. S. Eo, S. Wolgast, A. Rakoski, D. Mihaliov, B. Y. Kang, M. S. Song, B. K. Cho, M. C. Hatnean, G. Balakrishnan, Z. Fisk, S. R. Saha, X. Wang, J. Paglione, and C. Kurdak, Phys. Rev. B **101**, 155109 (2020).

[47] N. Xu, P. K. Biswas, J. H. Dil, R. S. Dhaka, G. Landolt, S. Muff, C. E. Matt, X. Shi, N. C. Plumb, M. Radović, E. Pomjakushina, K. Conder, A. Amato, S. V. Borisenko, R. Yu, H. M. Weng, Z. Fang, X. Dai, J. Mesot, H. Ding, and M. Shi, Nat. Commun. **5**, 4566 (2014).

[48] L. L. Moiseenko, and V. V. Odintsov, J. Less-Common Metals, **67** 237 (1979).

[49] M. Kasaya, F. Iga, K. Negishi, S. Nakai, and T. Kasuya, J. Magn. Magn. Mater. **31–34**, 437 (1983).

[50] F. Iga, N. Shimizu, and T. Takabatake, J. Magn. Magn. Mater. **177–181**, 337 (1998).

[51] H. Weng, J. Zhao, Z. Wang, Z. Fang, and X. Dai, Phys. Rev. Lett. **112**, 016403 (2014).

[52] J. C. Y. Teo, L. Fu, and C. L. Kane, Phys. Rev. B **78**, 045426 (2008).

[53] M. Legner, A. Rüegg, and M. Sigrist, Phys. Rev. Lett. **115**, 156405 (2015).

[54] F. Iga, S. Hiura, J. Klijn, N. Shimizu, T. Takabatake, M. Ito, Y. Matsumoto, F. Masaki, T. Suzuki, and T. Fujita, Physica B **259–261**, 312 (1999).

[55] M. Kasaya, F. Iga, M. Takigawa, and T. Kasuya, J. Magn. Magn. Mater. **47–48**, 429 (1985).

[56] K. Ikushima, Y. Kato, M. Takigawa, F. Iga, S. Hiura, and T. Takabatake, Physica B **281–282**, 274 (2000).

[57] H. Okamura, T. Michizawa, T. Nanba, S. I. Kimura, F. Iga, and T. Takabatake, J. Phys. Soc. Japan. **74**, 1954 (2005).

[58] T. Susaki, A. Sekiyama, K. Kobayashi, T. Mizokawa, A. Fujimori, M. Tsunekawa, T. Muro, T. Matsushita, S. Suga, H. Ishii, T. Hanyu, A. Kimura, H. Namatame, M. Taniguchi, T. Miyahara, F. Iga, M. Kasaya, and H. Harima, Phys. Rev. Lett. **77**, 4269 (1996).

[59] M. Okawa, Y. Ishida, M. Takahashi, T. Shimada, F. Iga, T. Takabatake, T. Saitoh, and S. Shin, Phys. Rev. B **92**, 161108(R) (2015).

[60] K. Sugiyama, F. Iga, M. Kasaya, T. Kasuya, and M. Date, J. Phys. Soc. Japan. **57**, 3946 (1988).

[61] F. Iga, K. Suga, K. Takeda, S. Michimura, K. Murakami, T. Takabatake, and K. Kindo, J. Phys. Conf. Ser. **200**, 012064 (2010).

[62] T. T. Terashima, Y. H. Matsuda, Y. Kohama, A. Ikeda, A. Kondo, K. Kindo, and F. Iga, Phys. Rev. Lett. **120**, 257206 (2018).

[63] T. T. Terashima, A. Ikeda, Y. H. Matsuda, A. Kondo, K. Kindo, and F. Iga, J. Phys. Soc. Japan. **86**, 054710 (2017).

[64] K. Hagiwara, Y. Ohtsubo, M. Matsunami, S. I. Ideta, K. Tanaka, H. Miyazaki, J. E. Rault, P. Le Fèvre, F. Bertran, A. Taleb-Ibrahimi, R. Yukawa, M. Kobayashi, K. Horiba, H. Kumigashira, K. Sumida, T. Okuda, F. Iga, and S. I. Kimura, Nat. Commun. **7**, 12690 (2016).

[65] L. Onsager, Philos. Mag. **43**, 1006 (1952).

[66] I. Lifshitz, and A. Kosevich, Sov. Phys. JETP **2**, 636 (1956).

[67] M. V. Kartsovnik, Chem. Rev. **104**, 5737 (2004).

[68] G. Li, Z. Xiang, F. Yu, T. Asaba, B. Lawson, P. Cai, C. Tinsman, A. Berkley, S. Wolgast, Y. S. Eo, D. J. Kim, C. Kurdak, J. W. Allen, K. Sun, X. H. Chen, Y. Y. Wang, Z. Fisk, and Lu Li, Science **346**, 1208 (2014).

[69] B. S. Tan, Y. T. Hsu, B. Zeng, M. Ciomaga Hatnean, N. Harrison, Z. Zhu, M. Hartstein, M. Kiourlappou, A. Srivastava, M. D. Johannes, T. P. Murphy, J. H. Park, L. Balicas, G. G. Lonzarich, G. Balakrishnan, and S. E. Sebastian, Science **349**, 287 (2015).

[70] S. M. Thomas, X. Ding, F. Ronning, V. Zapf, J. D. Thompson, Z. Fisk, J. Xia, P. F. S. Rosa, Phys. Rev. Lett. **122**, 166401 (2019).

[71] M. Hartstein, H. Liu, Y.-T. Hsu, B. S. Tan, M. C. Hatnean, G. Balakrishnan, and S. E. Sebastian, iScience **23**, 101632 (2020).

[72] L. Zhang, X. Y. Song, and F. Wang, Phys. Rev. Lett. **116**, 046404 (2016).

[73] O. Erten, P. Ghaemi, and P. Coleman, Phys. Rev. Lett. **116**, 046403 (2016).

[74] H. Shen and L. Fu, Phys. Rev. Lett. **121**, 026403 (2018).

[75] T. Yoshida, R. Peters, and N. Kawakami, Phys. Rev. B **98**, 035141 (2018).

[76] R. Peters, T. Yoshida, and N. Kawakami, Phys. Rev. B **100**, 085124 (2019).

[77] J. Knolle, and N. R. Cooper, Phys. Rev. Lett. **118**, 096604 (2017).

[78] D. Chowdhury, I. Sodemann, and T. Senthil, Nat. Commun. **9**, 1766 (2018).

[79] L. Balents, Nature **464**, 199 (2010).

[80] G. Baskaran, arXiv:1507.03477 (2015).

[81] O. Erten, P. Y. Chang, and P. Coleman, A. M. Tsvelik, Phys. Rev. Lett. **119**, 057603 (2017).

[82] C. M. Varma, Phys. Rev. B **102**, 155145 (2020).

[83] A. Kitaev, Ann. Phys. **321**, 2 (2006).

[84] Y. Kasahara, T. Ohnishi, Y. Mizukami, O. Tanaka, Sixiao Ma, K. Sugii, N. Kurita, H. Tanaka, J. Nasu, Y. Motome, T. Shibauchi, and Y. Matsuda, Nature **559**, 227 (2018).

[85] P. Coleman, E. Miranda, and A. Tsvelik, Physica B **186-188**, 362 (1993).

[86] Z. Xiang, Y. Kasahara, T. Asaba, B. Lawson, C. Tinsman, Lu Chen, K. Sugimoto, S. Kawaguchi, Y. Sato, G. Li, S. Yao, Y. L. Chen, F. Iga, J. Singleton, Y. Matsuda, and Lu Li, Science **69**, 65 (2018).

[87] Z. Xiang, Lu Chen, K.W. Chen, C. Tinsman, Y. Sato, T. Asaba, H. Lu, Y. Kasahara, M. Jaime, F. Balakirev, F. Iga, Y. Matsuda, J. Singleton, and Lu Li, (Under review at Nature Physics).

[88] H. Liu, M. Hartstein, G. J. Wallace, A. J. Davies, M. C. Hatnean, M. D. Johannes, N. Shitsevalova, G. Balakrishnan, and S. E. Sebastian, J. Phys. Condens. Matter **30**, 16LT01 (2018).

[89] M. M. Altarawneh, C. H. Mielke, and J. S. Brooks, Rev. Sci. Instrum. **80**, 066104 (2009).

[90] S. Ghannadzadeh, M. Coak, I. Franke, P. A. Goddard, J. Singleton, and J. L. Manson, Rev. Sci. Instrum. **82**, 113902 (2011).

[91] K. Götze, M. J. Pearce, P. A. Goddard, M. Jaime, M. B. Maple, K. Sasmal, T. Yanagisawa, A. McCollam, T. Khouri, P.-C. Ho, and J. Singleton, Phys. Rev. B **101**, 075102 (2020).

[92] D. Shoenberg, Cambridge University Press, Cambridge, England (1984).

[93] A. C. Jacko, J. O. Fjærestad, B. J. Powell, Nat. Phys. **5**, 422 (2009).

[94] Y. Matsumoto, K. Kuga, T. Tomita, Y. Karaki, and S. Nakatsuji, Phys. Rev. B **84**, 125126 (2011).

[95] N. Harrison, J. Singleton, A. Bangura, A. Ardavan, P. A. Goddard, R. D. McDonald, and L. K. Montgomery, Phys. Rev. B **69**, 165103 (2004).

[96] T. Senthil, M. Vojta, and S. Sachdev, Phys. Rev. B **69**, 035111 (2004).

[97] A. A. Patel, J. McGreevy, D. P. Arovas, and S. Sachdev, Phys. Rev. X **8**, 021049 (2018).

[98] Y. Matsuda, K. Izawa, and I. Vechter, J. Phys. Condens. Matter **18**, R705 (2006).

[99] W. A. Phelan, S. M. Koohpayeh, P. Cottingham, J. W. Freeland, J. C. Leiner, C. L. Broholm, and T. M. McQueen, Phys. Rev. X. **4**, 031012 (2014).

[100] M. Orendáč, S. Gabáni, G. Pristáš, E. GaŽo, P. Diko, P. Farkašovský, A. Levchenko, N. Shitsevalova, and K. Flachbart, **96**, 115101 (2017).

[101] M. Hartstein, W. H. Toews, Y. T. Hsu, B. Zeng, X. Chen, M. Ciomaga Hatnean, Q. R. Zhang, S. Nakamura, A. S. Padgett, G. Rodway-Gant, J. Berk, M. K. Kingston, G. H. Zhang, M. K. Chan, S. Yamashita, T. Sakakibara, Y. Takano, J. H. Park, L. Balicas, N. Harrison, N. Shitsevalova, G. Balakrishnan, G. G. Lonzarich, R. W. Hill, M. Sutherland, and S. E. Sebastian, Nat. Phys. **14**, 166 (2018).

[102] Y. Xu, S. Cui, J. K. Dong, D. Zhao, T. Wu, X. H. Chen, K. Sun, H. Yao, and S. Y. Li, Phys. Rev. Lett. **116**, 246403 (2016).

[103] M. E. Boulanger, F. Laliberté, M. Dion, S. Badoux, N. Doiron-Leyraud, W. A. Phelan, S. M. Koohpayeh, W. T. Fuhrman, J. R. Chamorro, T. M. McQueen, X. F. Wang, Y. Nakajima, T. Metz, J. Paglione, and L. Taillefer, Phys. Rev. B **97**, 245141 (2018).

[104] W. T. Fuhrman, J. Leiner, P. Nikolić, G. E. Granroth, M. B. Stone, M. D. Lumsden, L. DeBeer-Schmitt, P. A. Alekseev, J. M. Mignot, S. M. Koohpayeh, P. Cottingham, W. A. Phelan, L. Schoop, T. M. McQueen, and C. Broholm, Phys. Rev. Lett. **114**, 036401 (2015).

[105] Y. Sato, Z. Xiang, Y. Kasahara, T. Taniguchi, S. Kasahara, Lu Chen, T. Asaba, C. Tinsman, H. Murayama, O. Tanaka, Y. Mizukami, T. Shibauchi, F. Iga, J. Singleton, Lu Li, and Y. Matsuda, Nat. Phys. **15**, 954 (2019).

[106] Y. X. Wang, B. Revaz, A. Erb, and A. Junod, Phys. Rev. B **6309**, 094508 (2001).

[107] O. Taylor, PhD thesis, University of Bristol (2007).

[108] R. C. Chaney, E. E. Lafon, and C. C. Lin, Phys. Rev. B **4**, 2734 (1971).

[109] D. Watanabe, K. Sugii, M. Shimozawa, Y. Suzuki, T. Yajima, H. Ishikawa, Z. Hiroi, T. Shibauchi, Y. Matsuda, and M. Yamashita, Proc. Natl. Acad. Sci. USA **113**, 8653 (2016).

[110] I. Peroni, E. Gottardi, A. Peruzzi, G. Ponti, and G. Ventura, Nucl. Phys. B - Proc. Suppl. **78**, 573 (1999).

[111] A. Czopnik, N. Shitsevalova, V. Pluzhnikov, A. Krivchikov, Y. Paderno, and Y. Onuki, J. Phys. Condens. Matter. **17**, 5971 (2005).

[112] K. S. Nemkovski, P. A. Alekseev, J. M. Mignot, A. V. Rybina, F. Iga, T. Takabatake, N. Y. Shitsevalova, Y. B. Paderno, V. N. Lazukov, E. V. Nefeodova, N. N. Tiden, and I. P. Sadikov, J. Solid State Chem. **179**, 2895 (2006).

[113] G. E. Grechneva, A. E. Baranovskiy, V. D. Fil, T. V. Ignatova, I. G. Kolobov, and A. V. Logosha, Low Temp. Phys. **34**, 1167 (2008).

[114] P. W. Anderson, B. I. Halperin, and C. M. Varma, Philos. Mag. **25**, 1 (1972).

[115] S. Yamashita, T. Yamamoto, Y. Nakazawa, M. Tamura, and R. Kato, Nat. Commun. **2**, 275 (2011).

[116] D. Watanabe, M. Yamashita, S. Tonegawa, Y. Oshima, H. M. Yamamoto, R. Kato, I. Sheikin, K. Behnia, T. Terashima, S. Uji, T. Shibauchi, and Y. Matsuda, Nat. Commun. **3**, 1090 (2012).

[117] H. Katsura, N. Nagaosa, and P. A. Lee, Phys. Rev. Lett. **104**, 066403 (2010).

[118] O. I. Motrunich, Phys. Rev. B **73**, 155115 (2006).

# Published works

## Main work

**Y. Sato**, Z. Xiang, Y. Kasahara, T. Taniguchi, S. Kasahara, L. Chen, T. Asaba, C. Tinsman, H. Murayama, O. Tanaka, Y. Mizukami, T. Shibauchi, F. Iga, J. Singleton, L. Li, and Y. Matsuda,
"Unconventional thermal metallic state of charge-neutral fermions in an insulator",
Nature Physics **15**, 954–959 (2019).

## Journal articles (including the main work)

1. **Y. Sato**, S. Kasahara, H. Murayama, Y. Kasahara, E.-G. Moon, T. Nishizaki, T. Loew, J. Porras, B. Keimer, T. Shibauchi, and Y. Matsuda,
"Thermodynamic evidence for a nematic phase transition at the onset of the pseudogap in $YBa_2Cu_3O_y$",
Nature Physics **13**, 1074–1078 (2017).

2. **Y. Sato**, S. Kasahara, T. Taniguchi, X. Xing, Y. Kasahara, Y. Tokiwa, Y. Yamakawa, H. Kontani, T. Shibauchi, and Y. Matsuda,
"Abrupt change of the superconducting gap structure at the nematic critical point in $FeSe_{1-x}S_x$.",
Proceedings of the National Academy of Sciences **115**, 1227–1231 (2018).

3. Z. Xiang, Y. Kasahara, T. Asaba, B. Lawson, C. Tinsman, Lu Chen, K. Sugimoto, S. Kawaguchi, **Y. Sato**, G. Li, S. Yao, Y. L. Chen, F. Iga, J. Singleton, Y. Matsuda, and Lu Li,
"Quantum oscillations of electrical resistivity in an insulator",
Science **69**, 65–69 (2018).

4. H. Murayama, **Y. Sato**, R. Kurihara, S. Kasahara, Y. Mizukami, Y. Kasahara, H. Uchiyama, A. Yamamoto, E. G. Moon, J. Cai, J. Freyermuth, M. Greven, T. Shibauchi, and Y. Matsuda,
"Diagonal nematicity in the pseudogap phase of $HgBa_2CuO_{4+\delta}$",
Nature Communications **10**, 3282 (2019).

5. **Y. Sato**, Z. Xiang, Y. Kasahara, T. Taniguchi, S. Kasahara, Lu Chen, T. Asaba, C. Tinsman, H. Murayama, O. Tanaka, Y. Mizukami, T. Shibauchi, F. Iga, J. Singleton, Lu Li, and Y. Matsuda,
"Unconventional thermal metallic state of charge-neutral fermions in an insulator",
Nature Physics **15**, 954–959 (2019).

6. H. Murayama, **Y. Sato**, X. Z. Xing, T. Taniguchi, S. Kasahara, Y. Kasahara, M. Yoshida, Y. Iwasa, and Y. Matsuda,
"Effect of quenched disorder on the quantum spin liquid state of the triangular-lattice antiferromagnet 1T-$TaS_2$",
Physical Review Research **2**, 013099 (2020).

7. S. Kasahara, **Y. Sato**, S. Licciardello, M. Čulo, S. Arsenijević, T. Ottenbros, T. Tominaga, J. Böker, I. Eremin, T. Shibauchi, J. Wosnitza, N. E. Hussey, and Y. Matsuda,
"Evidence for an Fulde-Ferrell-Larkin-Ovchinnikov State with Segmented Vortices in the BCS-BEC-Crossover Superconductor FeSe",
Physical Review Letters **124**, 107001 (2020).

8. M. Yamashita, **Y. Sato**, T. Tominaga, Y. Kasahara, S. Kasahara, H. Cui, R. Kato, T. Shibauchi, and Y. Matsuda,
"Presence and absence of itinerant gapless excitations in the quantum spin liquid candidate $EtMe_3Sb[Pd(dmit)_2]_2$",

Physical Review B, **101**, 140407(R) (2020).

9. W. K. Huang, S. Hosoi, M. Čulo, S. Kasahara, **Y. Sato**, K. Matsuura, Y. Mizukami, M. Berben, N. E. Hussey, H. Kontani, T. Shibauchi, and Y. Matsuda,
"Non-Fermi liquid transport in the vicinity of the nematic quantum critical point of superconducting $FeSe_{1-x}S_x$",
Physical Review Research **2**, 033367 (2020).

10. H. Murayama, K. Ishida, R. Kurihara, T. Ono, **Y. Sato**, Y. Kasahara, H. Watanabe, Y. Yanase, G. Cao, Y. Mizukami, T. Shibauchi, Y. Matsuda, and S. Kasahara,
"Bond directional anapole order in a spin-orbit coupling Mott insulator $Sr_2(Ir_{1-x}Rh_x)O_4$",
In press at Physical Review X.

11. 佐藤雄貴, 笠原裕一, 伊賀文俊, 松田祐司
"近藤絶縁体の量子振動と中性フェルミオン励起"
日本物理学会誌に掲載予定

12. Z. Xiang, Lu Chen, K. W. Chen, C. Tinsman, **Y. Sato**, T. Asaba, H. Lu, Y. Kasahara, M. Jaime, F. Balakirev, F. Iga, Y. Matsuda, J. Singleton, and Lu Li,
"High field exotic metal in a Kondo insulator"
Under review at Nature Physics

# Acknowledgments

Firstly, I would like to express my greatest gratitude to my supervisor, Prof. Yuji Matsuda, for his continuous support throughout my doctoral course. Without his instructions and immense knowledge in physics, I certainly would not have been able to complete this research.

My sincere appreciation also goes to Prof. Takahito Terashima, Prof. Yuichi Kasahara, Prof. Shigeru Kasahara, Prof. Takasada Shibauchi, Prof. Yoshifumi Tokiwa, Prof. Lu Li, Prof. Eun-Gook Moon, Prof. Hiroshi Kontani, and Prof. Robert Peters for their experimental instructions and/or stimulating discussions related to my work. Further, I would like to appreciate Prof. John Singleton, Dr. Ziji Xiang, Dr. Lu Chen, Dr. Colin Tinsman, Dr. Ben Lawson, and Dr. Tomoya Asaba for discussions and their great efforts in the pulsed-field experiments at Los Alamos National Laboratory. Additionally, I would like to thank Prof. Fumitoshi Iga for providing extraordinarily clean single crystals of $YbB_{12}$ and $SmB_6$. I am deeply indebted to following fellows for discussions and helpful experimental support: Ms. Hinako Murayama, Dr. Xiangzhuo Xing, Mr. Tomoya Taniguchi, Mr. Ryo Kurihara, Mr. Takahiro Tominaga, Mr. Huang Wenkai, Dr. Yuta Mizukami, and Mr. Ohei Tanaka.

During my Ph.D. course, I was fortunate to have several chances to travel and conduct experiments abroad. I am deeply grateful to Prof. James Analytis for his kind support during my stay in Berkeley. I would also like to express my appreciation for Prof. Nigel Hussey and Dr. Matija Čulo for their kind support during intermittent experiments at High Field Magnet Laboratory in Nijimegen.

Many collaborators were involved in related unpublished work on another Kondo insulator, $YbIr_3Si_7$, which we have prepared but unfortunately could not be included in this thesis. I would like to thank Prof. Emilia Morosan and her workfellows in Rice University for providing us single crystals. I would also like to thank Prof. Andriy Nevidomskyy and Dr. Shota Suetsugu for fruitful discussions related to this work.

Moreover, I thank Prof. Kenji Ishida and Dr. Shunsaku Kitagawa for providing preliminary NMR results on $YbIr_3Si_7$.

I am grateful to the following labmates not only for their cooperation for my research but also for sharing a tough but fruitful time in Kyoto: Dr. Takuya Yamashita, Dr. Tatsuya Watashige, Mr. Yusuke Shimoyama, Dr. Masahiro Naritsuka, Mr. Daiki Terazawa, Mr. Tomohiro Ishii, Mr. Takafumi Onishi, Mr. Yohei Torii, Mr. Hironori Hashimoto, Mr. Sohei Miyake, Dr. Masahiro Haze, Ms. Tomoka Suematsu, Mr. Ma Sixiao, Mr. Daiki Sano, Mr. Satoshi Nakamura, Dr. Lang Peng, Mr. Takahito Ii, Mr. Hiroki Suzuki, Mr. Toshifumi Takahashi, Mr. Andre de Oliveira Silva, Mr. Yuzuki Ukai, Mr. Hiroaki Ominato, Mr. Takahiro Ono, and Mr. Taichi Yokoi. I would also like to thank lab secretary Ms. Ayumi Ishikawa for handling paperwork related to my research.

I wish to acknowledge financial support from the Research Fellowships of the Japan Society for the Promotion of Science for Young Scientists during my entire doctoral course.

Lastly, I must thank my family for their warm encouragement and support.